

INFORMATION TO USERS

The most advanced technology has been used to photograph and reproduce this manuscript from the microfilm master. UMI films the text directly from the original or copy submitted. Thus, some thesis and dissertation copies are in typewriter face, while others may be from any type of computer printer.

The quality of this reproduction is dependent upon the quality of the copy submitted. Broken or indistinct print, colored or poor quality illustrations and photographs, print bleedthrough, substandard margins, and improper alignment can adversely affect reproduction.

In the unlikely event that the author did not send UMI a complete manuscript and there are missing pages, these will be noted. Also, if unauthorized copyright material had to be removed, a note will indicate the deletion.

Oversize materials (e.g., maps, drawings, charts) are reproduced by sectioning the original, beginning at the upper left-hand corner and continuing from left to right in equal sections with small overlaps. Each original is also photographed in one exposure and is included in reduced form at the back of the book. These are also available as one exposure on a standard 35mm slide or as a 17" x 23" black and white photographic print for an additional charge.

Photographs included in the original manuscript have been reproduced xerographically in this copy. Higher quality 6" x 9" black and white photographic prints are available for any photographs or illustrations appearing in this copy for an additional charge. Contact UMI directly to order.



University Microfilms International
A Bell & Howell Information Company
300 North Zeeb Road, Ann Arbor, MI 48106-1346 USA
313/761-4700 800/521-0600

Order Number 1338523

**Scanning tunneling microscope characterization of nickel thin
film nucleation and growth**

Kelley, Murray, M.S.

The University of Arizona, 1989

U·M·I

**300 N. Zeeb Rd.
Ann Arbor, MI 48106**

**SCANNING TUNNELING MICROSCOPE CHARACTERIZATION
OF NICKEL THIN FILM NUCLEATION AND GROWTH**

by
Murray Kelley

A Thesis Submitted to the Faculty of the
COMMITTEE ON OPTICAL SCIENCES (GRADUATE)
In Partial Fulfillment of the Requirements
For the Degree of
MASTER OF SCIENCE
In the Graduate College
THE UNIVERSITY OF ARIZONA

1989

STATEMENT BY AUTHOR

This thesis has been submitted in partial fulfillment of requirements for an advanced degree at the University of Arizona and is deposited in the University Library to be made available to borrowers under rules of the Library.

Brief quotations from this thesis are allowable without special permission, provided that accurate acknowledgement of source is made. Requests for permission for extended quotation from or reproduction of this manuscript in whole or in part may be granted by the head of the major department or the Dean of the Graduate College when in his or her judgement the proposed use of the material is in the interests of scholarship. In all other instances, however, permission must be obtained from the author.

SIGNED: Murray Kelley

APPROVAL BY THESIS DIRECTOR

This thesis has been approved on the date shown below:

U. J. Gibson
U. J. Gibson
Professor of Optical Science

9/14/89
Date

ACKNOWLEDGEMENTS

I would like to take a moment to thank everyone who contributed to the creation of this thesis. Ursula Gibson was a most adept advisor, giving advice when asked, offering encouragement when needed, and applying pressure when necessary. Pat Kearney and Mike Burkland were very helpful, questioning that which I would have preferred simply to assume. Frank Suits was indispensable in explaining vacuum system idiosyncrasies. Ken Cornett helped in many ways, answering a slew of niggling questions, as did the rest of the OMG crew: Andy, Byron, Heidi, Joy, Marc, Tony, and Virginia.

On a much deeper level, I could not have accomplished any of this without the loving support of my wife Pam and daughter Brittany. They were there for me emotionally and spiritually through thick, thin and dark of sleepless night.

TABLE OF CONTENTS

	Page
LIST OF ILLUSTRATIONS	8
LIST OF TABLES	13
ABSTRACT	14
I. INTRODUCTION	15
Historical Perspective	16
Research Overview	18
II. SCANNING TUNNELING MICROSCOPE BACKGROUND	22
Quantum Mechanical Tunneling	22
Tunneling Microscopy	25
Vacuum Tunneling	25
Scanning Microscopy	26
Tunneling Spectroscopy	29
Resolution	31
Design Considerations	37
III. THIN FILM NUCLEATION AND GROWTH	42
Film Growth Theories	42
Microstructure Development	43
Structure Zone Models	48
Growth Mode Models	53
Nucleation	58
Film Stability	64

Table of Contents *continued*

	Page
IV. FABRICATION AND CHARACTERIZATION OF THIN NICKEL FILMS	65
Nickel Film Deposition	65
The Vacuum System	66
Materials and Preparation	69
Shadowing	72
Deposition Procedures	73
Film Handling	76
Scanning Tunneling Microscope Operation	76
The Nanoscope® II System	78
Calibration	84
Tips	85
Sample Requirements	86
Scanning Modes	89
Signal Processing	91
Conventional Film Characterization	93
Thickness and Roughness	94
Optical Photomicrography	95
Scanning Electron Microscopy	96
X-ray Diffraction	96
V. SCANNING TUNNELING MICROSCOPE RESULTS	97
Scanning Conditions	97
Conductivity, Noise and Feedback	97
Typical Signal Processing	99

Table of Contents *continued*

	Page
Initial Nucleation	99
Substrate Structure	100
Nucleation Sites	100
Critical Nuclei	109
Quantitative Nucleation Analysis	109
Nucleation and Condensation	111
Surface Activation Energies	112
Spatial Nucleation Variations	114
Coalescence Stage	115
Substrate Effects	115
Island Formation and Structure	119
Island Distribution	119
Continuous Films	123
Microstructure and Surface Roughness	123
Film Defects	141
Surface Spectroscopy	147
Discussion	147
VI. CONVENTIONAL FILM ANALYSIS	149
Thickness and Roughness	149
Film Growth and Microstructure	150
Optical Microscopy	151
Scanning Electron Microscopy	162
X-ray Diffraction	162

Table of Contents *continued*

	Page
Comparison With STM Results	164
Film Growth	164
Film Microstructure	167
VII. SUMMARY	168
REFERENCES	170

LIST OF ILLUSTRATIONS

Figure	Page
Figure 2.1 Graphical representation of scanning tunneling microscopy.	24
Figure 2.2 Various aspects of graphite including a) the SBZ collapsed to one state at \bar{P} (after Tersoff, 1986), ⁴⁴ b) the hexagonal monolayer structure, and c) a lineplot showing a typical STM scan of HOPG.	35
Figure 3.1 The tangent rule [$\tan \beta = 1/2(\tan \alpha)$] for oblique growth of Zone 1 grains.	51
Figure 4.1 The vacuum system used to deposit most of the nickel films used in this research (from F. Suits, 1988). ⁶⁷	67
Figure 4.2 Temperatures on the surface of a fused silica substrate and within the molybdenum heater block during e-gun depositions of Al_2O_3 at room temperature and 140°C (from F. Suits, 1988). ⁶⁷	74
Figure 4.3 RGA spectrum of background gas partial pressures in the vacuum system after pumping for three hours (from F. Suits, 1988). ⁶⁷	75
Figure 4.4 STM lineplot image of a region of nickel film showing a scratch caused by handling the film. Notice the pile of film material at the end of the scratch.	77
Figure 4.5 Block diagram of the layout of the Nanoscope II (from Digital Instruments, 1989). ⁴⁸	79
Figure 4.6 A photograph of the whole microscope unit including the large scan head.	81
Figure 4.7 SEM micrograph of a typical Pt0.8Ir0.2 tip in good condition taken at 200X.	87
Figure 4.8 High magnification SEM micrograph of the end of the tip shown in Figure (4.7).	88
Figure 4.9 Graphical representations of the data acquisition cycles for spectroscopic plot modes a) $I(V) _{s=C}$, b) $I(v) _{s=C}$, and c) $I(s) _{v=C}$ (adapted from Digital Instruments, 1989). ⁴⁸	90
Figure 5.1 Preferential nucleation and growth of nickel deposits along the upper side of ledges and canyons on HOPG.	101

List of Illustrations *continued*

Figure	Page
Figure 5.2 Nucleation of nickel islands on a slightly rippled section of HOPG.	102
Figure 5.3 A top-view of nickel nucleation islands, shown in purple, with indications of island bridging.	103
Figure 5.4 A three-dimensional view of the same nickel nucleation region shown in Figure (5.3) which reveals the occurrence of island bridging more clearly.	105
Figure 5.5 Single atom thick nucleation islands on HOPG partially covered by clusters of nickel, also only one atom thick, which form a partial second layer of atoms.	106
Figure 5.6 A three-dimensional view of the edge of a large island and adjacent field of small nucleation islands.	107
Figure 5.7 Three-dimensional view of a small nickel nucleation island showing barely resolved nickel atoms.	108
Figure 5.8 Reciprocal temperature dependence of the saturation nucleation density for nickel films on HOPG.	113
Figure 5.9 Spatial variation of the nucleation rate as a function of distance from the continuous film edge.	116
Figure 5.10 STM scan of the extreme edge of a continuous film growth.	117
Figure 5.11 Small STM scan one millimeter from the continuous film edge showing island growth only along a graphite defect.	118
Figure 5.12 Typical coalescence stage nickel island shown in 3-D relief.	120
Figure 5.13 False illumination top view of the nickel island shown in Figure (5.12).	121
Figure 5.14 Large STM scan showing island growth in clusters and along graphite features.	122

List of Illustrations *continued*

Figure	Page
Figure 5.15 Top view of nickel film grown on HOPG at room temperature and a 30° angle of incidence.	125
Figure 5.16 Three-dimensional view of a room temperature nickel film deposited at a 30° angle.	126
Figure 5.17 Top view of the surface of a nickel film deposited on HOPG at 300°C and an angle of 30°.	127
Figure 5.18 Three-dimensional view of a nickel film deposited on HOPG at 300°C and an angle of 30°.	128
Figure 5.19 Top view of a room temperature film on fused silica.	129
Figure 5.20 Three-dimensional view of the surface texture of a room temperature nickel film deposited on fused silica.	130
Figure 5.21 A top view of a sputtered nickel film deposited on silicon at just above room temperature.	131
Figure 5.22 A three-dimensional view of the surface of a sputtered nickel film deposited on silicon at just above room temperature.	132
Figure 5.23 The temperature dependence of surface roughness for several nickel film series.	134
Figure 5.24 Temperature dependence of the microRMS of nickel films on HOPG showing uncertainty.	135
Figure 5.25 Temperature dependence of the roughness of nickel films on fused silica as measured with the Wyko and the STM, showing uncertainty.	136
Figure 5.26 Observed angle of deposition dependence of surface roughness for nickel films deposited on HOPG.	137
Figure 5.27 Disturbance of normal film microstructure by deposition at high angles of incidence.	139
Figure 5.28 The increase in film grain size as a function of increasing temperature for several film families.	140

List of Illustrations *continued*

Figure	Page
Figure 5.29 Temperature dependence of grain size for nickel films on HOPG, showing uncertainty.	142
Figure 5.30 Temperature dependence of grain size for nickel films on fused silica, with uncertainty indicated and data from Fleet shown for comparison.	143
Figure 5.31 A large dislocation loop defect on an old nickel film.	144
Figure 5.32 A stress induced tear in a nickel film.	145
Figure 5.33 A large hole in a room temperature nickel film some 5 μm from the edge of the continuous film.	146
Figure 6.1 A typical surface region on HOPG photographed at 200X.	152
Figure 6.2 A 500X photo of a relatively high quality area of HOPG marred by numerous small grooves and a few larger defects.	153
Figure 6.3 A 200X micrograph of a large canyon on HOPG in a nickel film region. Note the preferential film growth around the canyon edges.	154
Figure 6.4 A 500X view of nickel island growth on graphite at 300°C.	155
Figure 6.5 A 500X view of nickel island growth on a heavily faulted region of HOPG. This sample was deposited at 205°C.	156
Figure 6.6 Nickel film deposited on fused silica at 500°C shown at 500X. Note the scratches, the substrate defects at the lower left, and the texture of the film which is just visible.	158
Figure 6.7 A 500X view of a nickel film deposited on fused silica at 100°C. Note the large hole revealing bare substrate and the polishing grooves visible on the film surface which can also be seen on the substrate in the hole.	159
Figure 6.8 A 200X optical micrograph of the edge of a sputtered nickel film on silicon. The film region is the lighter area on the left.	160

List of Illustrations *continued*

Figure	Page
Figure 6.9 A 200X optical micrograph of the edge of a sputtered nickel film on float glass.	161
Figure 6.10 A 10,000X SEM image of a nickel film on HOPG which just reveals some of the ledge features characteristic of the graphite.	163
Figure 6.11 X-ray data showing the (111) peak from a nickel film deposited on HOPG at room temperature.	165
Figure 6.12 A section of an X-ray scan of a nickel film deposited on HOPG at 300°C showing the sharp (111) peak.	166

LIST OF TABLES

Table	Page
Table 3-1 Nucleation rate equation variable parameters for various condensation regimes.	59

ABSTRACT

A study of the nucleation, growth and final microstructure of vacuum deposited nickel films has been performed using scanning tunneling microscopy (STM) as the primary research instrument. Typical nucleation conditions are reported for nickel films grown on partially shadowed highly-oriented pyrolytic graphite (HOPG), and techniques are developed for using the STM to catalog film islands instead of more conventional electron microscopes. Values for the activation energy of surface diffusion, critical nucleus size, changes in the saturation nucleation density with temperature, and spatial variations in the nucleation rate are included.

Roughening and microstructure changes observed with STM are reported as functions of substrate temperature and deposition angle for nickel films grown on highly-oriented pyrolytic graphite and fused silica. Conventional film RMS roughness values are compared to microRMS values derived from STM data and STM images of film microstructure are compared with SEM and optical microscope photographs.

CHAPTER I

INTRODUCTION

In less than a decade the scanning tunneling microscope (STM)^{*} has progressed from a crude and delicate instrument to a robust tool for surface study which has immeasurably advanced our understanding of the microscopic world around us. Perhaps not since the invention of the laser has such an important tool for scientific analysis been developed. Indeed, the ability of the STM to image atomic surfaces with beautiful clarity never fails to fascinate its operators. In the beginning it was the prospect of atomic imaging that spurred this research, but later it became apparent that STM could be used alongside various other surface analysis techniques to augment a detailed study of the properties of thin films. Comparing STM images with results from several other thin film analysis techniques is an important undercurrent in this research, but STM data on the formation of nickel thin films forms the basis of this thesis. Since it is very important that this data be accepted without the reservations sometimes held about new research techniques, it will be helpful to briefly review the history of the STM.

^{*} From this point on the acronym STM will be used interchangeably to mean scanning tunneling microscope and scanning tunneling microscopy.

Historical Perspective

The scanning tunneling microscope was invented in late 1981 by a team of researchers at IBM's Zürich laboratory lead by G. Binnig and H. Rohrer.^{1,2} It had taken years of dedicated research by this team and many others to reach the point where the tunneling gap from probe tip to sample could be isolated from its environment and stabilized to the degree necessary to maintain the constant tunneling current needed for imaging.^{3,4} Since that time however, rapid progress has been made in STM design and use. STM research has been especially prolific in the field of solid state physics where the ability of the STM to image surfaces with atomic resolution has allowed the study of surface reconstructions and subtle surface structure variations by direct observation.⁵ In fact, so important were the discoveries made by researchers using the STM that Binnig and Rohrer were awarded the 1986 Nobel Prize in Physics for its invention, a mere five years after the first STM images were made.

In the three years since then STM use has continued to spread to other disciplines, especially in the biological sciences where near-atomic imaging of biological materials offers fascinating possibilities for advancing our understanding of the processes of life.^{6,7} Instrument designs have rapidly become smaller, tougher and more versatile.⁴ As a result, STM can now be performed in vacuum, at atmospheric pressure or even under liquids, at temperatures ranging from somewhat above room temperature down to that of liquid helium. In fact, with a little ingenuity, it is now possible to image almost anything that is just slightly conductive.⁵ Even dielectrics can be imaged if the tunneling is energetic enough to thermalize electrons in the sample.⁸

In the future STM use is likely to continue its spread. It will soon become a standard tool for surface analysis alongside electron microscopy, AES, LEED, UPS, XPS, TPD, and others.^{9,10} A variety of commercial instruments are now available, each tailored to specific research needs.⁵ In biological circles, the STM is thought likely to greatly accelerate progress on the Human Genome Project. Further into the future, the ability of the STM to manipulate atoms and molecules could result in a revolution in nanochemistry and nanomanufacturing. Crude molecular lithography is possible even

now.^{11,12} As Paul Hansma puts it, a STM tip "...can be thought of as a miniature robot arm -- but one that currently lacks a hand."⁵

Before any of this occurs though, the STM may be replaced by a closely related instrument developed by Binnig¹³, the atomic force microscope or AFM. The AFM is one of a slew of microscope concepts based on using localized phenomenon other than tunneling to probe samples. It features a tip mounted on a cantilever beam placed within Ångstroms of a surface to detect the minute interatomic forces between the tip and the surface. As the cantilever beam is scanned over the surface it deflects in reaction to its interatomic attraction to the surface, indicating the positions of atoms on the surface. In a Rube Goldberg arrangement, a laser or STM is then used to track the motion of the cantilever beam and trace out an image of the surface. Thus AFM has two advantages over STM, it can scan any material conducting or not, and since it does not rely on the electrical properties of the sample, it is immune to the surface-tip interactions that sometimes plague STM scans.¹⁴ To date however AFM's remain fragile and their resolution is seldom better than 10 Ångstroms.¹⁵ Thus they are not yet competitive in the lab environment except for scanning dielectric materials.⁴

The more distant history of the STM is fascinating as well, with researchers coming within a hair's breadth of realizing the concept of an STM only to be discouraged by technical problems.⁴ The idea of tunneling through a vacuum barrier is not new, having first appeared in solid state physics research just before 1930. However it was not until the late 1950's that well developed theories arose to explain tunneling.³ The impetus at the time was the development of solid tunneling junctions used to study superconductivity on a local scale.¹⁶ Because of the relatively large size of the tunneling region however, the resolution of these devices was quite limited. Experimentation continued because of the interesting possibilities for tunneling microscopy in surface science, but successes were limited by technical difficulties.¹⁷ Russell Young broke the stalemate in 1971 with his "topographiner" which scanned surfaces with field emission electrons providing a lateral resolution of about 4000 Ångstroms. Progress was made with other instruments in the 1970's, including Clayton Teague's "stylus profilometer" which used a scanning method to drag a needle over a surface, obtaining three-dimensional images with 1000 Ångstrom lateral resolution. Both Young and Teague discussed vacuum tunneling to some degree, but neither pursued the issue.⁴ It was Binnig and Rohrer, beginning in 1978,

who picked up the pieces. They knew from field ion microscopy that it was possible to image atoms, but progress was stalled by the problem of producing tips sharp enough to do so.⁴ As it turned out this was incredibly easy, simply grinding a tungsten wire at an angle produced sufficiently sharp tips.^{2,8} This possibility had been hinted at before by field ion microscopists who noted that emissions came only from the extreme ends of their sharpened samples, indicating that the samples were a good deal sharper than was previously thought, but no one realized the ramifications.⁴ Once sharp tips were available, the only hurdle remaining in STM design was the purely mechanical need to design a rigid device isolated from vibrations which Binnig and Rohrer accomplished in 1981.¹

Research Overview

After it was decided to study a thin film system using a combination of STM and more conventional methods, considerable effort went into selecting a candidate. Early on the II-VI semiconductors ZnS and CdS were considered because considerable effort had been put into these systems by fellow researchers, but they proved too difficult to scan reliably in air. Scanning cadmium sulfide was further complicated by its multitude of surface states which added a great deal of chemical structure to normal STM scans. Aluminum films were also considered but their tendency to oxidize in air was too great to overcome. Films grown on silicon appeared promising as well because it was possible to passivate silicon in air by covering it with oil, but they too were discarded.

It was the possibility of actually studying film growth from nucleation to continuous deposit by using graphite as a substrate that finally suggested using nickel for the films because it was easy to deposit via e-gun and it did not oxidize in air.¹⁸ Graphite was selected as the primary substrate because it is very easy to scan with STM and has been extensively studied.^{5,19,20,21,22} Nickel islands on HOPG could be scanned with STM and easily separated from the surrounding graphite substrate material, allowing film growth to be quantified with ease since individual islands and small clusters could be counted and measured directly from the digitized scans.

Since nickel had also just been selected by a fellow researcher for a study of columnar microstructure formation and surface diffusion, a broad study of nickel film nucleation and growth was expected to be of assistance. On a broader scale, nickel films had not been previously researched with STM in sufficient detail and no direct nucleation studies had been done.^{23,24,25} Earlier conventional studies of other metal films were available for comparison, but the use of HOPG substrates broke new ground. Previous work relied almost exclusively on metal, glass or cleaved salt crystal substrates.^{26,27} As a result some films were deposited on fused silica so the resulting film microstructures could be directly compared to other studies. Unfortunately growth studies were not possible on fused silica because it cannot be scanned by STM.

Having decided to study nickel films on HOPG and fused silica, a research plan was outlined which stressed the use of STM wherever possible. Conventional film analysis techniques such as electron microscopy were to be used only in a supporting role to check the results obtained by STM. Since temperature was expected to have the greatest effect on final film microstructure, it was explored in considerable detail using the structure zone model of Movchan and Demchishin as a guide.²⁸ Angle of deposition effects were also studied, but not with the same emphasis. In order to produce a variety of film growth regions on a single substrate, it was decided to shadow the films. This produced a film thickness gradient over a portion of the substrate as the continuous film gradually thinned and then broke up into an island structure.

Initially it was hoped that the formation of a complete film deposit could be followed as it coalesced from small clusters into large islands separated by channels which then filled to form a continuous film. However nickel was observed to form a continuous film very rapidly after island coverage became significant. Large continuous film regions often formed after only 35 Å of film material had been deposited. Following island growth was thus impractical, but this mode of growth did mean that island distributions were largely unchanged by coalescence until just before the film became continuous. As a result, the initial nucleation islands of nickel often remained intact until a very mature island stage and could be counted long after nucleation ceased. This fortunate occurrence allowed nickel film nucleation to be quantified by simply gathering demographic information about the size and number of nickel islands in the film growth regions. To accomplish this, island population

counts were performed at various distances from the edge of continuous film growth on several of the nickel films grown on HOPG. Several thousand islands were counted, enough to insure that the island population distributions were accurately sampled.

The structure of continuous nickel films was studied for several families of films. First, nickel was grown on HOPG at a 10° angle of incidence and substrate temperatures of 25, 70, 100, 200, and 300°C , covering Zone 1 growth and crossing into Zone 2 at the highest temperature. Equivalent films were also deposited on HOPG at a 30° angle of incidence to explore the effect of a higher angle of deposition. A family of nickel films was also deposited on fused silica at 30° and temperatures of 25, 100, 200, 300, 400, and 500°C , for comparison with the 30° films on HOPG. The highest temperature film of this family crossed into the Zone 3 growth region. Finally a family of films was deposited at room temperature on HOPG at 20° , 40° , 60° , and 80° angles of deposition to explore the effect of large angles of deposition on film microstructure.

All of these films were scanned with the STM multiple times to get an accurate picture of their structure. Once that had been determined, a series of at least four large scans was made and RMS roughness calculations made. Small scans were also taken to provide high resolution images of individual film grains. If any particularly interesting features were observed in the course of these scans they were recorded as well.

Optical and stylus profilometry were applied to the films on fused silica to provide conventional film thickness and RMS roughness information. The HOPG films could not be studied by either of these methods. All of the films were studied under a Nomarski-capable optical microscope and an attempt was made to apply SEM to the films as well. Unfortunately, nickel proved to be a most unsatisfactory SEM specimen and no useful results were obtained. A few of the films were also X-rayed to insure that the nickel films were indeed in the expected FCC (111) orientation.

The results of these conventional film analysis techniques are discussed in Chapter 6. The much larger amount of STM data is presented in Chapter 5 and a brief comparison of the two is appended to Chapter 6. For the reader unfamiliar with STM design, operation and capabilities, a review is presented in Chapter 2. Chapter 3 covers the film nucleation and growth theory relevant to the work done in this thesis. Sections on structure zone models and the qualitative effects of various

experimental factors on film microstructure are included. The equipment used to deposit all the nickel films is discussed in Chapter 4 along with sections on the conventional equipment used and the operation of the Nanoscope® II STM used for the great bulk of the STM research reported. Finally, a summary of the results and their significance is presented in Chapter 7.

CHAPTER II

SCANNING TUNNELING MICROSCOPY BACKGROUND

Because it is a relatively recent technology, the scanning tunneling microscope has not yet become standard research equipment. This is especially true of its use as a tool for surface analysis including nucleation and growth studies such as those that form the basis of this research.⁵ As a result, a brief overview of quantum mechanical tunneling and the theoretical basis for scanning microscopy based on it is presented here. In addition, the various physical and design factors that limit scanning tunneling microscopy are discussed.

Quantum Mechanical Tunneling

Quantum mechanical tunneling through an energy barrier is the very essence of scanning tunneling microscopy. The same agent is responsible for many other natural phenomenon including alpha particle emission from heavy atomic nuclei and frustrated total internal reflection of photons at the boundary between two optical materials separated by a very thin layer of less optically dense material. In the case of STM the tunneling is usually the transfer of a constant current of electrons between a sharp metallic tip and a conductive sample separated by a few Ångströms of gas, liquid, vacuum, or even non-conductive solid.⁵ This is shown schematically in Figure (2.1). Because the tip is unusually only a few Ångströms from the surface being scanned the effective current densities can get quite high, but even so tunneling can be shown to occur one electron at a time. In addition, even at relatively low applied voltages such as the 10 mV typically used to scan clean metallic surfaces, dramatic local electric

field strengths are produced. However, because electrons are tunneling one at a time, space charging and sample heating are not a problem.²⁹

In less advanced studies quantum tunneling is usually modeled as a one-dimensional problem in order to keep calculations tractable.⁵ Using this simple approach, the tunneling current in a scanning tunneling microscope can be expressed, for well behaved low voltage and low temperature cases, as

$$I \propto e^{-2\kappa s}, \quad (2-1)$$

where I is the tunneling current, κ is the decay constant for the electron wave functions in the tunneling barrier, and s is the distance from tip to sample. If the tunneling barrier is vacuum, the decay constant κ is closely related to the effective local work function ϕ by

$$\kappa = (2m\phi)^{1/2} / \hbar, \quad (2-2)$$

where m is the free electron mass here because the barrier is vacuum. In this case κ represents the minimum inverse decay length for the wave function in vacuum.²⁹ The effective local work function ϕ is more difficult to quantify as it depends on detailed tunneling parameters. If the tip were at infinity, ϕ would simply be the average of the work functions of the tip and the sample, but at normal tunneling distances a complex interaction known as the image potential may reduce ϕ significantly.³

Although tunneling is actually a three-dimensional phenomenon, this simple approach proves to be quite powerful. In cases where atomic scale surface detail is not being imaged, the exponential nature of these equations allows fairly accurate prediction of tunneling behavior. For example, choosing values typical of a metallic sample, $1/\kappa < 1 \text{ \AA}$ and $\phi \approx 4 \text{ eV}$, reveals that the tunneling current decreases by an order of magnitude for every angstrom that the tunneling gap s is increased.^{3,5,29} As a result, if the tunneling current is stable to within only 20%, the tunneling gap will vary by a mere 0.1 angstrom. This is startling resolution and forms the basis for interpreting STM images as surface topographs. Unfortunately, as STM imaging is pushed down into the interesting realm of atomic scale surface corrugations, this simple picture breaks down rapidly. On such a minute scale, attention must be paid to electronic interactions between the tip and the sample as well as to the exact meaning of terms such as the tunneling gap.⁵

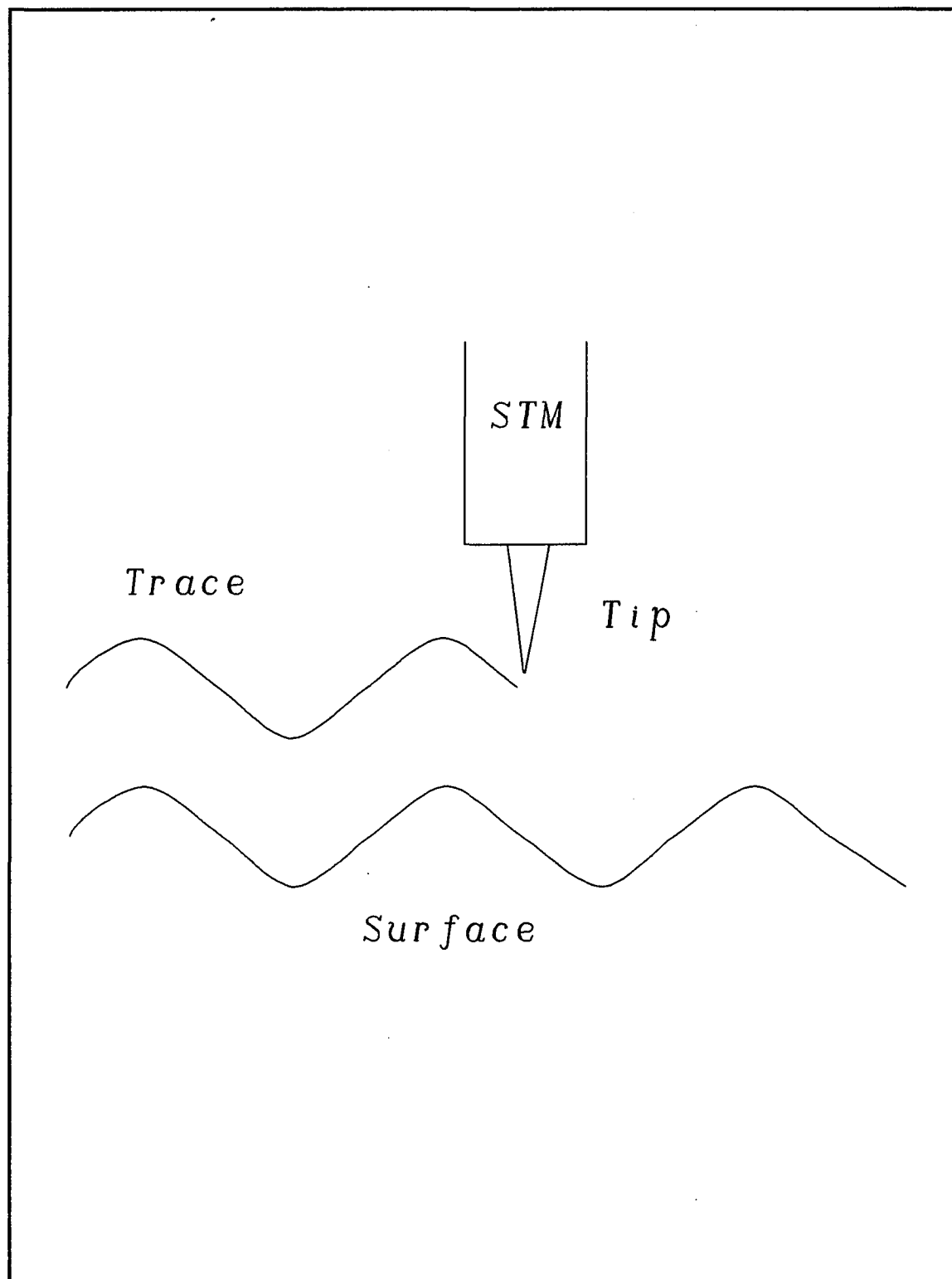


Figure 2.1 Graphical representation of scanning tunneling microscopy.

Tunneling Microscopy

In order to come to an understanding of the finer points of STM operation and image interpretation, it is first necessary to develop a detailed theory of vacuum tunneling. This is accomplished below by utilizing models initially developed to analyze quantum tunneling across superconducting metal-oxide-metal junctions thirty years ago.¹⁶ These models are easily adapted for STM analysis and the resulting equations can be generalized to apply to the great majority of STM applications. The equations themselves are powerful enough to predict actual tunneling parameters and instrument resolution, test new applications for STM, and analyze or simulate STM images.²⁹

Vacuum Tunneling

The greatest difficulty encountered in modeling vacuum tunneling is that while it may be possible to write out a formal expression for tunneling current in realistic situations, it is quite often impossible to use these equations. The computations are simply too intractable or require an overly exacting knowledge of tunneling conditions. Practically, rather severe approximations are required before any useful calculations can be performed.²⁹ Fortunately, the exponential nature of tunneling barriers tends to muffle approximation errors to the extent that even quite crude calculations yield surprisingly accurate results.⁵

One promising approach advanced by Tersoff and Hamann²⁹ is to apply relatively simple first-order perturbation theory to vacuum tunneling to yield a tunneling current given by

$$I = (2\pi e/\hbar) \sum_{\mu, \nu} f(E_{\mu}) [1 - f(E_{\nu} + eV)] |M_{\mu\nu}|^2 \delta(E_{\mu} - E_{\nu}), \quad (2-3)$$

where $f(E)$ is the Fermi function, V is the applied voltage, $M_{\mu\nu}$ is the tunneling matrix element between states ψ_{μ} of the tip and ψ_{ν} of the sample, and E_{μ} is the energy of the state ψ_{μ} in the absence of tunneling.²⁹ The descriptors μ and ν range over all the states of the tip and the sample respectively.⁵

It should be noted that equation (2-3) is quite similar to standard first-order perturbation theory except that in this case ψ_μ and ψ_ν are non-orthogonal eigenstates of different Hamiltonians.²⁹ At elevated temperatures an additional reverse tunneling term must be added.²⁹ Under the more typical conditions of low applied voltage and room temperature operation, equation (2-3) can be simplified to²⁹

$$I = (2\pi e^2 V / \hbar) \sum_{\mu, \nu} |M_{\mu\nu}|^2 \delta(E_\nu - E_f) \delta(E_\mu - E_f). \quad (2-4)$$

In either case the tunneling matrix element, $M_{\mu\nu}$, can be given in the elegant Bardeen tunneling-Hamiltonian formalism

$$M_{\mu\nu} = (\hbar^2 / 2m) \oint dS \cdot (\Psi_\mu^* \nabla \Psi_\nu - \Psi_\nu \nabla \Psi_\mu^*), \quad (2-5)$$

taking the integral over any plane in the tunneling barrier.³⁰

Other methods of addressing vacuum tunneling have been suggested, but most suffer from major drawbacks.^{29,31,32} The most promising alternative, proposed by Feuchtwang *et al.*³³, represents the tunneling current as a convolution of spectral functions of the tip and surface instead of proposing specific forms for the tip wave functions. These spectral functions are not known well so severe approximations are still required. Furthermore it is very difficult to apply this method to constant-current tunneling, the usual mode of STM operation. However, such an approach can be beneficial when considering constant-height tunneling, which is often approximated during STM spectroscopic operation.

In principle, equations (2-3) through (2-5) are sufficient to determine the tunneling current and in turn the STM image. This basic tunneling theory makes no distinction between tip and sample as they were interchangeable in the case of the superconducting tunneling junctions used in early vacuum tunneling experiments. In the case of a STM however this distinction can be critical because exact current analysis involves a complex convolution of the electronic states of the tip and the surface.^{29,34}

Scanning Microscopy

Extending the equations given above to a realistic treatment of scanning tunneling microscopy is a difficult task. A reasonable first step is to analyze an ideal case where the tip is treated as a localized

point. This has the effect of removing tip properties from the equations and greatly simplifying the analysis.⁵ In the case of low applied voltage, the tunneling current is simply

$$I \propto \rho(\mathbf{r}_t, E_f), \quad (2-6)$$

where \mathbf{r}_t is the tip position, E_f is the familiar Fermi energy and

$$\rho(\mathbf{r}, E) \equiv \sum_{\nu} |\Psi_{\nu}(\mathbf{r})|^2 \delta(E_{\nu} - E), \quad (2-7)$$

which is simply the local density of states (LDOS) at point \mathbf{r} and energy E , or the charge density due to states at E .⁵ This energy is generally the Fermi energy because the surface states typically involved in tunneling at low voltages lie very close to E_f .²⁹ The tunneling current is thus proportional to the LDOS at the position of the point tip, so the microscope image is merely a contour map of constant LDOS for the bare sample surface.²⁹ In this case it is actually more accurate to couch the equations in terms of conductance instead of current because conductance is independent of voltage in the low voltage limit, but this complicates matters later on.⁵

As simple as this result is, it is basically correct and explains the major image features revealed by more complex STM theories. Indeed Tersoff and Hamann have shown that tips of arbitrary size can be accommodated by this approach as long as the tip wavefunctions at E_f were reasonably approximated by s-wave functions and \mathbf{r}_t was taken to represent the center of curvature of the tip wave functions. In fact even small ℓ -wave components in the tip wave functions cause only minor discrepancies in the results.^{35,36} It is thus quite safe to assume that (2-6) is accurate as long as the tip is tunneling through a single atom or a small cluster of atoms, as is quite often the case.⁵

It is not possible to push this line of reasoning any further without detailed knowledge of the structure of the microscope tip itself. As this is not reasonable, the usual approach is to assume a locally spherical tip of radius of curvature R_c which has a number of arbitrarily sharp minitips at its very extremity.²⁹ Tunneling occurs between the sample and whichever minitip is closest to it. The lateral extent of the tunneling region is very limited, often less than three atomic spacings^{34,37}, and the current density drops off exponentially away from the center of the region.⁵ Studies have also shown that the shape and extent of the tunneling region depends on the exact geometries of the tip and surface as well as on the type of atoms involved in the tunneling.^{34,37} The details of such an analysis are too

complex to delve into here but are well documented elsewhere.²⁹ Generally such calculations predict minitip curvatures of 10 Å or less and tunneling gaps of 3 to 6 Å for normal STM operation.³⁵

Any of the theoretical discussions above can be adapted to use outside of vacuum by simply adjusting the appropriate constants including the effective work function ϕ , wave function decay constants κ , effective electron mass m , and so forth to match the physical properties of the barrier medium be it air, water, oil, or whatever. Unfortunately the major side effect of such conversions is that most of the neat solutions and slick approximations given above get messy. However, as has been emphasized before, the inherently exponential nature of tunneling barriers heavily buffers most tunneling calculations including the critical LDOS and tunneling current calculations. In fact even an error as gross as a factor of e^2 in the coefficients of equations (2-6) and (2-7) above would only result in a 10% error in the calculation.²⁹

Finally, the equations derived above can be applied to real tunneling situations in order to simulate what the STM image should look like. This is often necessary to check the validity of STM scans, but progress is slow and limited to simple or experimentally important systems by the sheer number and complexity of the calculations required. However in cases that have been modeled, the results have been in striking agreement with quality STM images, even when severe approximations were used.²⁹ In some more exotic cases, including those involving chemically heterogeneous surfaces, simplistic approaches often fail badly.⁵ A case of importance here is that of incomplete film growth on a substrate. Such a surface contains a great number of boundaries between the two chemically different materials where a less than full blown tunneling model can be expected to fail, at least in its prediction of fine surface detail. Fortunately, much of the STM work done for this thesis does not utilize atomic scale images, so this problem should not be a major concern.

Tunneling Spectroscopy

It is possible to probe the chemical and electronic nature of surfaces by employing a STM as a scanning tunneling spectroscopy (STS)** to study the local I-V, V-s, and I-s characteristics of the surface. This is generally done by imaging dI/dV or dI/ds while scanning and maintaining a constant average tunneling current.⁵ This is possible because STM actually images surfaces in five dimensions, three for space (x,y,z) plus tunneling current I and tunneling voltage V. Here s is the size of the tunneling gap. Various imaging modes are accessed simply by recording data for the dimensions of interest.³ The I-V properties of the surface, measured as $(dI/dV)(x,y)$, record the variations in the LDOS while the I-s properties, measured as $(dI/ds)(x,y)$ or $(ds/dV)(x,y)$, map the work function variations across the surface. As a result, dI/dV scans are referred to as STS images and dI/ds scans as work function profiles, just as images of $z(x,y)$ at constant current are called surface topographs or STM images.³

Just as is done in conventional tunneling spectroscopy, scanning tunneling spectra are taken by superimposing a small, rapid oscillation on the tunneling voltage while scanning over the surface in the usual fashion.³ The oscillation must be faster than the response time of the feedback circuit of the STM otherwise it would simply be countered by normal feedback response. Because these oscillations are so much faster than the feedback response, the tip effectively does not react in the z-direction while spectra are being taken. Thus this mode of operation approximates what is known as "constant height" STM operation.⁵ Note that STS and work profile images can also be produced by subtracting two STM images taken at different voltages or at different currents respectively.³ It is also advantageous to scan the surface rapidly to minimize tunneling gap distortions and yield cleaner images. However, scanning speed is limited because of the large electric fields produced on the sample surface by high speed scans. These fields tend to increase the tunneling gap and hence degrade resolution. They might also harm loosely bound surface adsorbate layers or delicate biological molecules.³ Current STM designs are

** From this point on the acronym STS will be used interchangeably to mean scanning tunneling spectroscopy and scanning tunneling spectroscopy.

capable of gap stabilities approaching 0.1 Ångstroms, stable enough for a large class of spectroscopic studies to be performed at the low scan rates currently feasible. Another order of magnitude in gap stability is required before routine study of atomic vibrational spectra is possible however.³

As is the case with STM images, it is often necessary to take STS and work function profile images with a grain of salt as anomalous features can appear in the images. Just as electronic and chemical interactions appear as unwanted spectroscopic information in topographic STM scans, residual surface topography can appear in STS images. Following Binnig and Rohrer³, and taking tunneling current to be of the general form

$$I = P(V)f(V,s), \quad (2-8)$$

a $\partial I/\partial V$ modulation signal would take the form^{***}

$$\partial[\ln(I)]/\partial V = \partial[\ln(P)]/\partial V + \partial[\ln(f)]/\partial V. \quad (2-9)$$

For voltages well below the effective tunneling barrier ϕ , f is independent of V and thus $\partial I/\partial V$ is independent of (x,y) along an equicurrent line even if the surface is electrically inhomogeneous.^{3,5} At moderate tunneling voltages where $V = \phi$, f becomes dependent on topography and thus indirectly so does $\partial I/\partial V$. In STS images taken at moderate voltages this residual structure appears in the form of inverted topography. At voltages well above ϕ , this anomalous structure dependence becomes negligible again.³

Work profile images are also subject to a certain amount of anomalous topographic degradation. Continuing with Binnig and Rohrer³, the $\partial I/\partial s$ modulation signal is, neglecting logarithmic terms in s ,

$$-\partial[\ln(I)]/\partial s = \sqrt{\phi} + (\sqrt{\phi}/2)\partial\phi/\partial s. \quad (2-10)$$

As discussed earlier ϕ is the effective work function which may differ significantly from the normal work function for the surface. Because ϕ is a local value it can reflect variations in local electronic charge concentration, increasing in the presence of excess charge and waning in areas where charge is absent. Local charge variations also cause variations in the tunneling gap s . Thus when ϕ is dependent on s ,

^{***} In the theoretical discussion which follows, partial derivatives (∂) are used where appropriate. For readability however, the full derivative (d) is used throughout the bulk of the text when spectroscopic modes are discussed.

residual topographic structure may be introduced into the work profile image. Otherwise $\partial I/\partial s$ is a direct measure of the local value of ϕ . The image potential created by the act of tunneling can also modify ϕ , but its influence on $\partial I/\partial s$ is minor and can be neglected. Even if ϕ is uniform, some structural information can get into work function profile images via local surface gradient variations. The tunneling gap is controlled in the z direction, perpendicular to the average sample surface, while the actual tunneling gap s is dependent on the direction of the tunneling cone between the tip and the surface. This cone is roughly perpendicular to the gradient of the local surface element and not the average surface so $\partial I/\partial s$ is influenced by local surface variations as

$$\partial I/\partial s = (\partial I/\partial z)/\sin\theta, \quad (2-11)$$

where θ is the angle between the z direction and the gradient of the local surface element. Thus the measured value of $\partial I/\partial s$ underestimates ϕ by a factor of $1/\sin\theta$. Determination of actual values of ϕ is further complicated by other factors that remained unexplained. Experimental observations often yield values of only tenths of eV, far below the standard values of several eV and much too low to be explained by image potentials and anomalous topographic effects.^{3,38}

It is also possible to measure $\partial s/\partial V$ when gathering I - s spectra, but measuring $\partial I/\partial s$ directly is usually easier. However, in the case of true constant current tunneling the special relationship

$$\partial I/\partial V + (\partial I/\partial s)(\partial s/\partial V) = 0 \quad (2-12)$$

holds. Since $\partial I/\partial s$ is typically featureless in this mode, it is possible to determine $\partial I/\partial V$ by measuring $\partial s/\partial V$.³⁹

Resolution

Vacuum tunneling equations (2-6) and (2-7) above can be used to derive some basic physical limitations on the resolution obtainable with scanning tunneling microscopy by examining the LDOS function ρ . As was discussed previously, the vertical resolution of a STM is in the sub-angstrom regime by virtue of the strong exponential dependence of tunneling current on the tunneling gap.⁵ However,

the lateral resolution of a STM is more difficult to determine.²⁹ First, it is necessary to carefully consider what is meant by resolution in this case. On one hand a nominal resolution can be defined by noting that as either the tunneling gap or the tip size is increased, the image corrugation decreases exponentially. Using detailed tunneling equations and employing reasonable assumptions about the decay of the image corrugation with increasing tunneling gap, it is possible to define the averaging performed by the tip while scanning a surface as a Gaussian resolution function of rms width

$$W \simeq \sqrt{z/2\kappa}, \quad (2-13)$$

where z is the sum of tip radius and the tunneling gap $r + d$, and κ is the decay constant for wavefunctions in the tunneling barrier. Thus for a single atom tip where z might be as small as 5 Å, this means, given $1/\kappa \approx 1$ Å for metal samples, the nominal resolution of a STM could reach $W = 1.6$ Å.^{5,29,36}

More often though it is the ability of an instrument to separate two peaks that defines its effective resolution. In the case of a STM, this relates to the ability of the instrument to detect atomic corrugations. This may be easily approximated by assuming a minimum signal to noise ratio of 1:1.⁵ If a surface with lattice constant a and corresponding Fourier component $G = 2\pi/a$ has a noise amplitude n_c , then the corrugation of the LDOS, ρ , must have at least an equal amplitude to be detected. Assuming small corrugations scanned far from the surface, perhaps a half dozen Ångstroms away, the observed corrugation is roughly

$$\Delta = (2/\kappa)e^{-zG^2/4\kappa} \simeq (2/\kappa)e^{-G^2W^2/2}. \quad (2-14)$$

Then for $\Delta \geq n_c$, the resolution criterion is given by

$$a \geq [2\pi^2 / \ln(2/\kappa n_c)]^{1/2} \cdot W, \quad (2-15a)$$

or for values typical of tunneling on metals

$$a \simeq 4[\ln(2 \text{ Å}/n_c)]^{1/2} \cdot W, \quad (2-15b)$$

where a is the closest that neighboring atoms may be and still meet the signal to noise restriction. For a well controlled noise level of 0.1 Å, the effective resolution is about 4 Å -- consistent with resolution observed on metallic samples where electron sharing between atoms usually inhibits the imaging of individual atoms.⁵

It is possible to achieve somewhat better resolution than this if a single, localized orbital is used for imaging. Such an orbital can be provided by an adsorbate atom^{3,37} or a monatomic tip with an elongated and dangling orbital.⁸ In the adsorbate atom case a relatively loosely bonded atom attaches to the end of the tip, providing an isolated source of tunneling current which reduces the effective tip size and improves resolution. This also applies to many semiconductor samples because the individual sample atoms are somewhat isolated from each other electrically, tending to localize tunneling current and improve resolution.^{40,41} Improved resolution can also be seen in scans of metal surfaces where monatomic steps are resolved because the atom at the edge of the step is somewhat isolated from its surroundings.⁴² A tip with a dangling orbital, typically a d-orbital pointed downward from the very end of the tip, also yields a very narrow tunneling cone and occasionally resolution good enough to image atoms on metal surfaces.^{8,24,38} Producing a tip with a dangling orbital is basically a matter of luck, but by testing they can be selected from batches of normal tips.

Unfortunately, anomalous effects in topographic STM scans sometimes cause this relatively general picture to break down. There are various causes for these effects, but the problem is usually related to electrical or chemical interactions between the tip and the sample.⁵ Generally these interactions act like an extra source of noise and tend to decrease resolution, however in some cases unique interactions actually lead to significant increases in the apparent resolution of the STM.⁴³ One particularly illustrative example of this latter phenomenon happens to involve graphite.⁴⁴ In light of the resolution limits discussed above, the 2.46 Å periodicity of the unit cells of graphite should be just beyond the resolution of STM, and any marginal resolution should yield small surface corrugations no more than 0.25 Å high. In reality though, any decent STM can easily resolve the unit cell spacings on a clean graphite surface with corrugations ranging from 1-7 Ångstroms.⁴⁵ Such large corrugations cannot result from imaging actual atomic structure, so some anomalous effect must be influencing the tunneling process on graphite.

One possibility put forward by Tersoff *et al.*⁴⁴ postulates that such corrugations could result if the Fermi surface of the sample was collapsed to a point at one corner of the surface Brillouin zone (SBZ). In the usual case where the STM is operated in constant current mode, it images contours of constant LDOS such that the image closely resembles the total charge density distribution across the sample

because the Fermi surface is extended and tunneling occurs simultaneously into a large number of surface states. However if the Fermi surface is collapsed, only one surface state, or perhaps a symmetry related set of surface states, is imaged. Thus the STM is no longer imaging surface structure, but rather the spatial variation of one surface state, which is actually spectroscopic information normally gathered during dI/dV spectroscopy. If the imaged state lies on a SBZ edge, as is often the case with semiconductors, it will generally have nodes which produce large anomalous corrugations in the STM image due the imaging of charge density waves (CDW's) instead of atoms. These SBZ-edge CDW corrugations replicate the periodicity of the sample unit cell, but they are usually independent of the actual atomic positions within the unit cell. Typically the CDW corrugations are several times larger than those possible for actual atomic corrugations and this allows the apparent imaging of features normally too small to resolve with STM. Two-dimensional semiconductors such as 1T-TaS₂^{43,46} and graphite generally have appropriately collapsed Fermi surfaces, but the size of the resulting corrugation enhancement in graphite images is still disputed.^{44,45}

Imaging individual surface states with STM was first noted when phase changes were observed in features on Si(111)(2x1) surfaces scanned at voltages corresponding to valence-band and conduction-band states at the SBZ edge.^{4,29,44} Shortly afterward, the appearance of anomalous corrugations in the much simpler graphite system lead to the proposal of CDW imaging as the source of a whole class of similar observations.⁴⁴ Following the analysis by Tersoff,⁴⁴ it can be shown that the loosely bonded monolayers of graphite act like a zero-gap two-dimensional semiconductor with a single state at \bar{F} of the SBZ determining E_F , as shown in Figure (2.2a). Further calculations show that idealized 2-D graphite monolayers have a hexagonal CDW consisting of three CDW's at 120° angles which can be expanded in terms of six plane waves and represented in the dimensionless form

$$\zeta = \ln \left\{ \sum_{n=1}^3 \sin^2(\omega_n \cdot \eta) \right\} + \zeta_0, \quad (2-16)$$

where the CDW directions ω_n are (0,1), $(\sqrt{3}/2, 1/2)$, and $(-\sqrt{3}/2, -1/2)$. This system consists of a hexagonal array of singular nodes as well as a six-fold node in the center of the hexagon. In reality graphite has weak interlayer bonding which lifts the central node and breaks the six-fold symmetry. This produces two types of sites in the hexagonal structure, those over atoms in the layer below (A sites) and those over gaps in the layer below (B sites), as shown in Figure (2.2b). These sites are

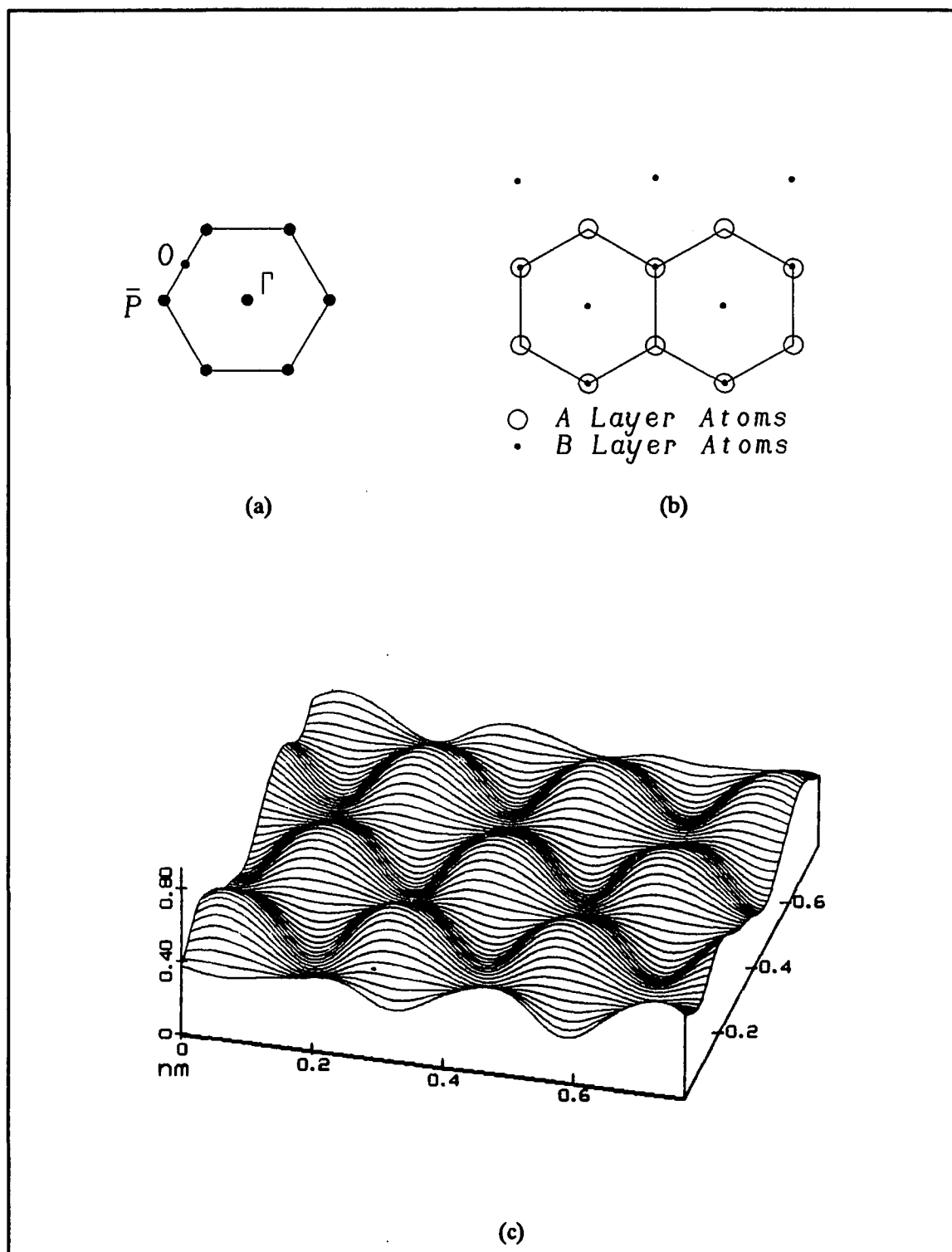


Figure 2.2 Various aspects of graphite including a) the SBZ collapsed to one state at \bar{P} (after Tersoff, 1986),⁴⁴ b) the hexagonal monolayer structure, and c) a lineplot showing a typical STM scan of HOPG.

energetically inequivalent and result in the type of graphite structure routinely imaged with STM. A representative lineplot is shown in Figure (2.2c). Note however that because of the inequivalency of sites A and B, STM images of the atomic structure of graphite are more difficult to visualize than one might expect. It is helpful to visualize the graphite as a diamond structure instead of hexagonal. Each peak in Figure (2.2c) corresponds to two atoms, not one. The peaks are shared by one B-site atom and one A-site atom smeared together by the STM. The distance from peak to peak then represents the unit cell spacing, 2.46 Å, instead of the atomic spacing, 1.42 Ångstroms.⁴⁵

Because the structure of graphite is quite simple, the CDW image is not too complicated. It replicates not only its unit cell periodicity but, fortuitously, some of the atomic structure as well. The 1.42 Å nearest-neighbor spacing is not fully resolved so A and B sites become smeared together giving the graphite more of a trigonal (or diamond-shaped) symmetry rather than the expected hexagonal appearance. In more complex materials, such as silicon in the (7x7) reconstruction, the CDW image may not appear at all like the atomic structure of the material, but the relationship between the CDW and atomic images is still quite significant. Studies on other materials have shown that regions which yield poor CDW images also yield poor atomic images, indicating a close correlation between the two.⁴³

Despite the strong theoretical basis for explaining anomalous resolution on graphite in terms of CDW imaging, several prominent researchers hold that other physical effects are at work.⁴⁵ Central to their reasoning is the observation that graphite images do not behave like scans of 1T-TaS₂, which are known to reflect CDW imaging.^{43,46} First, quality graphite images have corrugations much larger than those typical of other 2-D semiconductors, and second, corrugations larger than 2 Å cannot be explained by CDW imaging.⁴⁵ In addition, scans of other 2-D semiconductors like 1T-TaS₂ often contain regions where the CDW structure is mixed with areas of smaller corrugations where the actual atomic structure is resolved.⁴³ These and other discrepancies lead to the postulation of another source for the graphite corrugations analogous to that initially proposed by Soler *et. al.* (according to Batra *et. al.*)⁴⁵ to explain similar effects seen with AFM. It seems that on some materials, graphite included, the equilibrium tip ride height is extremely low. This proximity increases the electric field in the vicinity of the sample to such an extent that the integrity of the material is difficult to maintain. Elastic deformation of the surface layer occurs, yielding unusually high resolution as the tip "pushes" down into

holes in the sample surface. Other possibilities such as slippage of graphite layers and enhanced tunneling through tip or surface contamination layers may also increase observed corrugation heights somewhat. Current thinking is that some combination of effects including elastic deformation, CDW imaging and some plane slippage, usually account for the extremely large corrugations observed on graphite.⁴⁵

In the end then extreme care must be taken when quoting resolution figures for STM images. Equations (2-15) are fine when pure atomic structure is being imaged, but small anomalies in the chemical or electrical behavior of the sample or tip can lead to drastic variations in observed resolution. Thus it is best to check any analysis of STM images against data gathered from other sources.

Design Considerations

The long delay between the development of a workable theory of vacuum tunneling in the late 1950's and the invention of a working STM in 1981 was principally due to the daunting design problems presented by scanning tunneling microscopy.⁴ The most restrictive design criterion turned out to be mechanical rigidity, followed by vibration isolation.¹ In addition, problems involving materials for use in the scanning heads and tips had to be resolved.⁴⁷ In fact the only part of STM design that was initially well appreciated was the design of electronics for instrument control and data acquisition. These difficulties were magnified further by the fact that all early STM research had to be done in vacuum in order to insure that surface images were stable enough to scan.² In deference to these difficulties, a brief review of STM design criteria is given below. Several excellent detailed studies exist⁴⁷, but it should be noted that STM design is advancing rapidly so recent sources are preferable.

First consider the mechanical design of a STM. It usually consists of a large number of separate components including electronics modules, vibration isolation platforms, sample holders, scanning heads, and manual controls. The design of most of these components is fairly unconstrained, but it is essential that the mechanism keeping the scanning head and tip in tunneling contact with the sample be

extremely rigid. Typically this involves only the sample holder and the scanning head plus a couple of controls for manually engaging the tip. If this structure is very rigid, little or no mechanical distortion of the tunneling gap will occur during scanning and the STM images will be superior. The usual measure of this rigidity is resonant frequency.⁴⁷ Current non-UHV designs can have resonances of 40 to 60 kHz⁴⁸ while UHV designs can reach 100 kHz, a vast improvement over the 1 kHz resonance of the early Binnig and Rohrer instruments. Unfortunately, a high resonant frequency translates into poor vibration isolation, pointing out the need for effective vibration isolation systems on which to mount STM heads.⁵ Design rigidity depends on the structure being small, homogeneous, resistant to thermal expansion, and having the fewest possible number of parts. It is equally important that the critical head components be mechanically decoupled from other parts of the STM to prevent vibrations from creeping in.¹ One drawback of a small and rigid design is that it limits convenient rough sample positioning over a useful range of several millimeters or more. A compromise between rigidity and convenience must be made and the preferred balance depends on the application envisioned.³

As indicated above, successful vibration isolation is critical for the operation of a STM. However, it is been shown that several simple schemes can be used effectively if they are tailored to the specific needs of individual instruments.⁵ Taken in general, all vibration isolation systems consist of some sort of elastic material supporting a mass M , and are characterized by their first resonant frequency f_r . For such a system there are three frequency ranges of importance: frequencies well below resonance where vibration isolation fails and vibrations are transmitted with a slight amplification, frequencies near resonance where vibrations are greatly amplified, and frequencies above resonance where vibrations are attenuated. The degree of amplification or attenuation present at a given frequency is determined by the amount of damping present in the system. Damping is usually expressed relative to critical damping, which is simply the damping level which produces the smallest amplification at resonance. Massive underdamping is preferred because it results in large attenuations above resonance. Unfortunately, the trade off is a large amplification at resonance. The solution is to select a reasonable degree of underdamping, often in the range 0.2 to 0.02 of critical, to balance the two effects. However, the lower the resonant frequency of the system with respect to the problem vibrations, the less damping

necessary. All other things being equal then, a vibration isolation system should have the lowest possible resonant frequency.

One simple but effective method of vibration isolation is to mount the STM on a cement block hung from elastic supports.⁵ For such a simple spring and mass system, the resonant frequency as a function of static deflection, Δ , is given by

$$f_r = (1/2\pi)(g/\Delta)^{1/2} = (0.5 \text{ Hz})(1/\Delta \text{ meters})^{1/2}. \quad (2-17)$$

It is relatively easy to devise a system with supports that stretch sufficiently when loaded to yield a resonant frequency of approximately 1 Hz. Such a system is capable of attenuating typical 20 Hz building vibrations by two orders of magnitude.^{5,47} Other viable alternatives include air tables and stacks of alternating metal and elastic spacers, a system often used on vacuum compatible STM designs.⁴ In addition, for operation in air it is usually necessary to enclose the STM head to shield it from acoustic vibrations which strike the STM directly.⁴⁸

The materials chosen for a STM design are also a major concern for reasons of mechanical and thermal rigidity as well as for accurate control of tunneling parameters. For mechanical rigidity, prime choices include hard metals and ceramics. Various stainless steel alloys are popular, especially in vacuum applications where UHV compatibility is critical. When thermal rigidity is considered however, the obvious choice becomes Invar, a nickel steel renowned for its low thermal expansion, because it nearly matches the thermal expansion of the piezoelectric ceramics typically used to control tip motion during tunneling.¹⁸ Failure to closely match thermal expansion coefficients can result in thermal distortion of the tunneling gap during STM operation, possibly resulting in a tip crash.⁴⁸

The properties of the piezoelectric crystals used for tip control must also be considered. All piezoelectrics respond to an applied electric field by stretching or contracting in a rapid, linear motion. This motion is then followed by a much slower, very non-linear, relaxation effect. As a result, all piezoelectric actuators suffer from some degree of hysteresis during use causing distortions in the tunneling gap which can degrade images.⁴⁹ This is most apparent when scanning atomic cliffs.⁵⁰ Scans towards the cliff face have sharp vertical features at the cliff site, as expected. However, scans coming from the upper side of the cliff have more gentle slopes at the cliff site due to overshoot of the piezos when confronted with the sudden drop in topography. Further complications result because the non-

linear behavior can result from a variety of changes in external parameters including electric and magnetic fields, mechanical stress, and changes in temperature. If these changes are severe enough, the behavior of the material may be permanently altered. Fortunately, in normal STM use at low voltage and room temperature, the non-linearity is usually within the uncertainty in the scanned image. However, care must be taken when heating piezos during vacuum bakeout or soldering operations.⁴⁹ Piezo crystals also tend to lose sensitivity to applied voltage after prolonged use and should be recalibrated periodically.⁴⁸

In the early days of STM development a lot of concern was lavished on tip properties because it was feared that lack of tip sharpness was at fault in many failed experiments.⁴ However, it has turned out that a variety of materials and preparation techniques can be used to make tips. The most common materials are tungsten^{2,3,5} and Pt_{0.8}Ir_{0.2}^{11,46} alloy prepared by cutting, grinding, electrochemical etching or ion milling.⁴⁸ These processes have different success rates and produce distinct tip geometries suited for different applications. In general, contamination free tips such as platinum-iridium are preferred for atomic work while symmetric tips such as etched tungsten are preferred for large scans where tip cleanliness is less important.⁴⁸ Regardless of origin not all tips work properly, so it is necessary to assess quality somehow. Presently the only way to precisely determine the atomic structure of a tip is by field ion microscopy.^{51,52} Since this is usually not possible, simpler methods have been devised. One method is to simply examine the tips under an optical microscope at about 200 power. Tips that look sharp at this magnification are usually capable of atomic resolution. A somewhat more sophisticated technique is to employ a SEM and image the very end of the tip. If the radius of curvature is less than one micron, the tip is almost certainly capable of atomic resolution.^{9,53,54}

Finally, the STM electronics should be considered. All that is required is a source of X and Y raster voltages to regulate scanning, high voltage amplifiers to drive the piezo crystals, a voltage source and current sensing amplifier to establish tunneling current, an error amplifier to provide feedback on tunneling current changes, and a display device.⁵ Computers are typically used for both display purposes and generation of raster voltages.^{55,56} Other standard laboratory equipment can perform the remaining functions, except for feedback control which requires some uncommon electronics.⁵

However, nothing particularly complex is required unless amenities such as digital signal processing and image processing are desired.⁵⁷

CHAPTER III

THIN FILM NUCLEATION AND GROWTH

A vast amount of literature is available on the theoretical and experimental aspects of thin film formation. Much of it is highly detailed, with the subject often being approached in a manner intended to shed light on only one specific field of research. Thus the theoretical background on nucleation and growth is fractured into regimes of interest. For the purposes of this thesis however it was necessary to cross these boundaries and appeal to various treatments of nucleation and growth of thin films in order to properly encompass the powerful new insights into this microscopic world provided by STM.

Film Growth Theories

Taking a general view, there are two ways to approach the classification of film growth. One may choose a macroscopic viewpoint point and divide films by the type of structure they exhibit after growth^{28,58,59}, or one may instead choose to apply an extremely microscopic view and follow the actual evolution of the film on an atomic scale.^{26,27} Both approaches have wide application and in this research they were used in concert. By relying on film microstructure, the macroscopic method allows films to be easily categorized into broad regimes for study and comparison without requiring any knowledge of how the film arrived at its final form. On the other hand, microscopic studies allow the physics of film growth to be studied in detail, but they often fail to yield a clear view of the bulk characteristics of the film.

Microstructure Development

Before proceeding, it is important to review the various factors that can affect the growth and final properties of thin films. Naturally there are a myriad of possibilities, but, following Neugebauer²⁷ and Venables²⁸, a few items can be identified which merit special consideration. Obviously, the physical properties of the film and substrate materials as well as the conditions under which the film was deposited are critical, but surface diffusion, interactions between materials, binding energies, and even environmental factors can also play a role in modifying the microstructure of a thin film.²⁷ All of these concerns are interrelated and most center around the initial nucleation of the thin film in question.

The basic tenet of all growth theories is that there is a barrier to the formation of a permanent film deposit known as the nucleation barrier.²⁷ That is to say, every evaporant atom reaching a surface does not stick immediately and begin to form a film. Rather, a number of still relatively mobile evaporant atoms, or adatoms, must first collect in one place and form a stable (or critical) nucleus for other evaporant atoms to adhere to before film growth can begin in earnest. This barrier to nucleation can sometimes be mitigated, but generally it leads to the formation of film islands in the early stages of film growth. These islands grow independently until they meet and coalesce into the final continuous film. If the nucleation barrier is high, the film will initially consist of only large islands because of the increased size of the critical nucleus in such conditions. Because the chances of forming large nuclei are small, the number of such islands will be quite low. On the other hand, a low nucleation barrier leads to the formation of large numbers of small islands because of the relative ease of assembling the requisite small nuclei. As might well be expected, low nucleation barrier films become continuous relatively quickly because of the dense packing of the small islands. The large islands of high nucleation barrier films take longer to coalesce because they are both farther apart. Extending this reasoning, low nucleation barrier films are expected to be quite fine grained while high nucleation barrier films are usually more coarse. Note however, that in either case an individual film grain could well be formed from a number of nuclei. In addition, grain size does not determine film roughness by itself. Certainly grain boundaries are a major contributor to film roughness, especially on a microscopic scale, but other factors such as grain three-dimensionality and intra-grain roughness can also contribute. So while a fine

grained film has a large number of roughness causing grain boundaries, a large grained film might also be rough if the grains are individually rough. Finally, other factors, not related to the initial nucleation of the film, can also influence microstructure development. The most important of these is final film thickness and, to some extent, the rate of deposition. Thus the final form of a film depends on a large number of variables and is particularly sensitive to the conditions that prevail during nucleation. To begin, consider how each of the factors listed above individually affects thin film nucleation.

Several of the physical properties of the film material enter into nucleation directly, especially in the case of metallic films such as nickel.²⁷ In fact, the Gibbs free energy of the metal, ΔG_v , is often the dominant factor in determining i^* , the critical nucleus size.⁶⁰ Applying the Gibbs-Helmholtz equation, Trouton's rule and the Clausius-Clapeyron equation, it is possible to show the direct relation between the Gibbs free energy, the heat of vaporization of the metal, ΔH_{vap} , and the supersaturation of the deposition material over the substrate.²⁷ So any material with a high heat of vaporization should also have a high ΔG_v . As a result, even the smallest nuclei of metals with a high heat of vaporization, such as nickel, tend to be stable once deposited because considerable energy is required to re-evaporate them. Moreover, as clusters grow this stability increases dramatically so that high boiling point metals have low inherent nucleation barriers. Consequently, high boiling point films tend to have fine grained microstructures.

Substrate structure can have an equally powerful contribution to nucleation both as an inhibitor and as an instigator. Near-perfect substrate structure serves to hinder nucleation in most cases because it is difficult for deposited atoms to find a strong binding site on the substrate.²⁶ It is even more difficult for large clusters to form under these conditions, so perfect substrate planes tend to be thinly populated with small islands during the early stages of film growth. However, several factors including localized dangling bonds and matching film and substrate lattice constants and crystal structures can reduce this nucleation inhibition. Substrate features such as ridges, furrows, and steps often have the opposite effect and act as strong sources of preferential nucleation. Enhanced nucleation may occur along ridges, in furrows and either above, below, or along steps.^{26,61} Early nucleation speeds film growth in these regions and often results in the growth of large, rough islands in the vicinity of defects because of the strong film-substrate interaction. Flat substrate areas resist film growth and yield a finer-

grained final film.²⁶ HOPG substrates have vast numbers of defect sites surrounding areas of perfect graphite structure, making for a unique combination of properties in one substrate. The effect of this dual substrate nature will be seen clearly in the STM results discussed in Chapter 5.

A variety of deposition parameters including the deposition rate, substrate temperature and angle of deposition can affect the formation of film structures.²⁷ The type of evaporation source used can also cause visible differences in film microstructure. In more extreme cases vacuum system background pressure and contamination can have effects too, but these will not be dealt with here.

The angle of deposition has a more or less independent effect on microstructure, the higher the angle of deposition, the rougher the film.²⁷ This roughening is due to localized shadowing effects which start at the earliest stages of nucleation. Because the evaporant is impinging on the substrate at an angle, film islands that form early in the nucleation phase tend to cast shadows on the substrate behind them, resulting in reduced deposition rates in the shadowed areas. This process continues throughout the deposition and results in a film with more hills and valleys than a comparable film deposited at normal incidence. Thus films deposited at significant angles are notably rougher. Naturally, this purely classical argument is not exactly correct because, as mentioned above, evaporant atoms are usually mobile to some extent. Surface diffusion of adatoms tends to counteract classical shadowing by moving atoms from high spots down into low spots on the growing film. Films made under conditions of high adatom mobility will show less roughening due to shadowing than films where evaporant atoms have a high sticking coefficient and do not move around much after striking the substrate. Another effect of depositing films at non-zero angles of incidence is orientation of the film features. Hills on the film will tend to grow into the oncoming flux of evaporant atoms, much like rime ice growing into the wind. However, the classical view is again modified by surface diffusion such that instead of growing at the angle of deposition, the hills grow at smaller angles.

The influence of substrate temperature on microstructure is very intuitive, atoms impinging on a hot surface will retain energy longer and will thus tend to be more mobile. This increases the nucleation barrier since it is more difficult to assemble the adatoms necessary to form a stable cluster when the adatoms are highly mobile.²⁷ The result is high temperature films tend to form from large islands and have large grain structures as a result. High surface mobility also allows the growing film

to decrease its total energy by leveling hills, filling valleys, and removing grain boundaries to form a large grained film. At some temperature though grain growth and surface mobility reach limits and the temperature dependence of film microstructure saturates.²⁷

The rate of deposition is generally not very influential in determining film microstructure.²⁷ In well-behaved systems, it is often necessary to change the rate of deposition by an order of magnitude before any significant change in film microstructure is observed. However, if increasing the deposition rate changes other factors, such as increasing film stress, a much smaller change in the rate of deposition could have tragic consequences for film structure and stability. In fact, tensile stress failure was observed by a fellow researcher when nickel films were deposited on HOPG at 5 Å/s using resistive heating.⁶²

While most of the films used in this research were deposited with an e-gun source, a few auxiliary films were deposited by resistance evaporation and dc-magnetron sputtering. These methods differ from e-gun deposition, and resulted in some variations in film microstructure for otherwise comparable films. Because the resistance evaporation source used was manually controlled, its deposition rate varied considerably. This was observed to increase the tensile stress of nickel films on HOPG, leading to structural failure unless rates of deposition below 5 Å/s were used. Sputtering on the other hand is more stable than any e-gun deposition. Full computer control and the lack of a rapidly changing liquid melt to contend with resulted in nearly flawless films with smooth grains and few islands atop the base film growth. Films deposited by either e-gun or resistive sources commonly had a number of hilly growths on the base film.

Interactions between the film and substrate can also play a vital role in determining nucleation and growth behavior. Chemical reactions can, of course, completely change the growth patterns of the film, but the effects of surface energy and bond strength are also important.^{26,27,63} If the surface energy of the film material is high, or if the substrate surface energy is low, the nucleation barrier will be high. Only large clusters will be stable in the former case because of the large amount of binding energy needed to overcome the surface energy and keep the cluster from re-evaporating. Likewise, low substrate surface energies must be supplemented by binding energy from film clusters or the film atoms will simply re-evaporate. The binding energy of the film material is also important independent of

surface energy considerations. Tight bonding film materials will nucleate more easily because smaller clusters will be resistant to re-evaporation. Loosely bound condensate clusters will fall apart much more easily. Binding of the film-substrate system is also important because a tight binding film material might still not stick to even a substrate with a high surface energy if the film atoms cannot somehow bind to the substrate. Unfortunately, information on HOPG is limited since historically it has not been important as a substrate material, but its layered structure indicates a low surface energy. By itself nickel is expected to have a high surface energy. Fused silica is a well studied substrate and is known to have a low surface energy, so one would expect a high nucleation barrier for nickel films on SiO_2 unless other factors act to ease nucleation.

All of these effects begin with nucleation and continue throughout the growth of the film. However, film microstructure can also be affected by the final thickness of the film, regardless of the nucleation conditions.²⁷ During growth, individual film grains tend to maintain their continuity. Thus thicker films have generally larger grains and a more uniform microstructure than thin films. At some point growth of individual grains is disrupted and secondary nucleation occurs, producing new grains. Thus grain growth with increasing film thickness is limited and saturates at some point.

There is also a competing phenomenon caused by fluctuations in the deposition process which tends to roughen films as they grow thicker.²⁷ Random variations in the arrival of evaporant atoms on the film surface lead to random height variations across the surface of the film which grow throughout the deposition process. If surface mobility is reduced to zero, these height variations, Δd , fit a Poisson distribution which reduces to

$$\Delta d = \sqrt{d}, \quad (3-1)$$

so that the film roughens as a function of the square root of its thickness. Non-negligible surface mobilities can reduce this effect but not entirely eradicate it. It is also possible for surface diffusion to enhance growth on the fastest growing crystal planes of the film, leaving behind the slower growing, denser, low index crystal planes.^{26,58} This tends to cause facets on the film surface, making it rougher again instead of smoother. To avoid problems relating to changing film thickness, all of the e-gun deposited films used in this research were made 500 Å thick.

Complications to this collection of individual effects arise because some or all of them are present simultaneously and in differing amounts in real film-substrate systems. It is important then to review what can be expected for the two systems investigated here, nickel on HOPG and nickel on SiO_2 , and compare that to what is actually observed. Nickel itself has conflicting properties. Its high melting point eases nucleation, but its high surface energy resists cluster formation. In reality though nickel is observed to nucleate with extreme ease, the critical nucleus size often being a single atom. The mixed structure of HOPG substrates will cause nucleation conditions and film microstructure to vary from region to region over the substrate. Smooth regions will resist nucleation and yield a smooth but fine grained microstructure while badly faulted regions will enhance nucleation and result in a lumpy film. STM observations confirm these expectations, with nickel films on HOPG having a fairly smooth background structure disturbed by numbers of large hills and even ridges propagated through the film from the substrate. Fused silica on the other hand is quite smooth and uniform. This should increase the size of the barrier to nickel nucleation and yield very smooth films with larger grains. Deposition parameters were varied for each film system as part of the research effort, so a discussion of the results will be deferred until Chapter 5. However, in all cases the rate of deposition was kept at a low 2 Å/s to insure that the film did not become stressed.

Structure Zone Models

With this picture of the generalities behind the formation of film microstructure in mind, it is possible to move on to a study of characterizing films by their microstructure. This type of structural categorization is known as structure zone modeling and was first developed by Movchan and Demchishin in their landmark 1969 paper.²⁸ In its original form it applied to a variety of thick films made by e-gun evaporation. Since that time other others have expanded on it to encompass sputtering and have extended the number of zone divisions recognized.⁵⁸ The initial work in the Soviet Union revealed the presence of three basic type of film microstructure referred to as Zones 1 through 3 which were functions of the melting temperature of the film material.²⁸ Zone 1 extended from zero Kelvin up to approximately 30% of the melting point of the film material, and was characterized by a grainy

film microstructure consisting of large numbers of individual tapered crystals with domed tops, large number of dislocations and a poorly defined internal structure. For nickel, with a melting point of 1726° K , this temperature, known as T_1 , is $543 \pm 10^\circ \text{ K}$. The second zone was more variable, but typically lasted up to about one-half the melting point of the film material. This is the well researched columnar growth region where grains often extend all the way through the film as thin columns with a well defined grain structure and dense intercrystalline boundaries giving the film surface a mat appearance. The cutoff temperature for Zone 2 growth is known as T_2 and for nickel it is $725^\circ \pm 10 \text{ K}$. Zone 3 was then defined as extending above this temperature and consisting of large, flat, polyhedral grains similar to those observed in recrystallized or annealed bulk metal. Metal films with this structure are quite smooth and reflective.

The mechanical properties of these three zones are also markedly different.³⁷ Zone 1 material has poor lateral strength and a high dislocation density, but the individual grains are extremely hard, possessing microhardness values several times those of the bulk annealed material. However this hardness decreases rapidly with temperature as the Zone 2 boundary is approached. This decrease in hardness continues, albeit more slowly, across Zone 2 where the columnar grains give the film more continuity but less hardness. Individual Zone 2 grains have a microhardness similar to bulk cast materials, with hardness decreasing across the temperature range of the zone in accordance with the Hall-Petch relationship. These films are still quite strong but they have little ductility. In Zone 3 the film hardness drops to the level of the recrystallized bulk material that it resembles.

Film roughness is also affected by structure zones. Instead of varying with temperature in a uniform manner as indicated in the previous section, film roughness has a consistent temperature dependence only across individual zones.²⁸ Large roughness variations are observed at the zone boundaries. In the case of Zones 1 and 2, the film begins finely-grained and quite rough. As temperature is increased within each zone, the grains, be they tapered crystals or columnar structures, grow in size so that the film usually becomes smoother. However the sudden change from large tapered crystals to small columns at the first zone boundary temperature of T_1 produces a dramatic increase in film roughness to accompany the change in structure. A similar roughness discontinuity is observed when entering Zone 3 because grain size increases dramatically. Despite the decrease in the

number of grain boundaries, roughness jumps abruptly at the boundary for nickel films because the formation of equiaxed Zone 3 grains disturbs the surface of the film as reconstruction takes place gradually. While grain size does not increase much more across Zone 3, additional temperature increases should smooth out the film surface and reduce roughness.

Movchan and Demchishin developed this zone system after analyzing an amazing amount of data, but most of it was from industrial strength experiments where tremendously thick films were deposited at incredible rates in huge e-gun evaporators.²⁸ For example some films were up to 2 mm thick deposited at $0.25 \mu\text{m/s}$ by 150 kW evaporators. As a result, the applicability of the results to the usual research grade film 500 Å thick deposited at 2.0 Å/s by a 3 kW e-gun is open to some question. And, in fact, later studies have lead to some modifications to the model.⁵⁸ The number of zones now recognized has increased to four or even five, and the range of the zones has changed. In addition zones are now delineated not so much by structure as by the dominant physical processes operating. It is profitable then to review the original Movchan and Demchishin zone model in this light.⁵⁸

In Zone 1 the crystal diameters increase with temperature, indicating that the activation energy of the film material is low and there is little in the way of surface diffusion. Thus, shadowing of surface regions beginning during nucleation becomes the dominant force in determining the film microstructure. As a secondary result of such shadowing, the tapered grains of this zone tend to grow in the direction of the deposition flux in accordance with the tangent rule

$$\tan \beta = 1/2(\tan \alpha), \quad (3-2)$$

which is shown in Figure (3.1). As with any added structure, tilted grains add to the roughness of the film.²⁷

In Zone 2 the more rapid increase in column width with temperature indicates that the film activation energy was high enough to activate surface diffusion as the dominant physical process and mitigate roughening due to shadowing.²⁶ However, the uniform columnar microstructure of this zone produces a strong tendency for the grains to grow into the oncoming deposition flux. Careful modeling of this effect has shown that it is much more complex than the tangent rule behavior of the Zone 1 grains. For a given incident flux angle, the columns can grow at a variety of angles defined by a one-parameter family of surface profiles. Typically the tilting is smaller than that predicted by the tangent

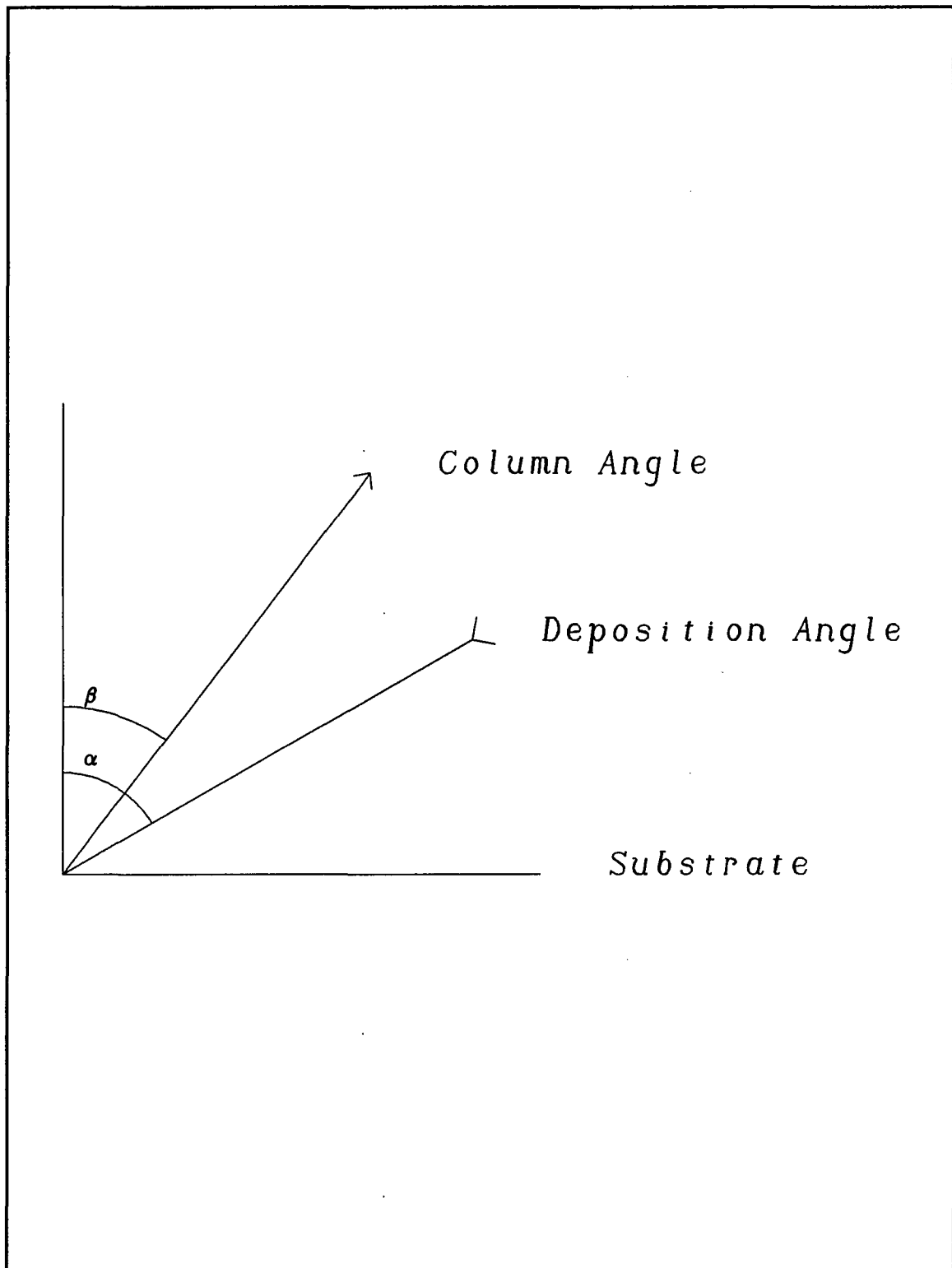


Figure 3.1 The tangent rule [$\tan \beta = 1/2(\tan \alpha)$] for oblique growth of Zone 1 grains.

rule, but the tangent rule values are among the possible results.⁶⁴ A variation in the Zone 1 to Zone 2 transition temperature with angle of deposition is also predicted. This tilted growth enhances roughening at oblique angles of deposition.

Finally in Zone 3 the activation energy is quite high, commensurate with bulk diffusion within the film.⁵⁸ Such diffusion requires time though, so if the film is not kept in this temperature range for a sufficient length of time, a Zone 3 structure will fail to fully develop. Representing the last area deposited, the surface of the film will naturally be the last area to transform to a Zone 3 structure. The film roughening observed for nickel films when entering Zone 3 is likely caused by a lack of time for the full structure transformation to take place while the temperature is barely sufficient to support Zone 3 structure. High film stress can assist the transition to a Zone 3 microstructure. In fact, normal lattice stress is assumed to be the general cause of the transition from Zone 2 to Zone 3. In extreme cases it is possible to form a Zone 3 microstructure at room temperature by stressing the film.

For this research a four zone scheme was used encompassing aspects of the Sanders classification (as reported by Thornton) and the intermediate Zone T structure identified by Thornton for sputtered films.⁵⁸ This last zone was included because the fibrous grain structures associated with it on sputtered films are duplicated on e-gun films deposited on HOPG substrates where the graphite structure is near perfect. Thus the final classification scheme was: Zone 1 ($T/T_m < 0.2$), Zone T ($0.2 < T/T_m < 0.3$), Zone 2 ($0.3 < T/T_m < 0.45$) and Zone 3 ($0.45 < T/T_m < 1$). For nickel, these zones correspond to the temperature ranges (1) below 75°C, (T) between 75°C and 270°C, (2) between 270°C and 450°C, and (3) above 450°C. Here the three numbered zones correspond to the like-numbered Movchan and Demchishin zone in both structural signature and dominant physical processes, even though the temperature ranges have been adjusted somewhat. The additional Zone T structure is characterized by grains that are fibrous and difficult to resolve, with dense grain boundaries. The film also has respectable lateral strength in this case, unlike the Zone 1 structure. Zone T represents the extreme fine-grained limit of Zone 1 growth and forms only on very smooth substrates. Features that induce preferential nucleation, like steps on the surface of HOPG, can easily disrupt it and force the growth of the less well ordered Zone 1 structure instead. Whereas in Zone 1 surface diffusion was

almost absent and shadowing dominated the formation of microstructure, in Zone T enough surface diffusion occurs to partially combat the roughening caused by shadowing during nucleation.

Note in conclusion that several factors can act to distort zone boundaries such that low temperature zones are found on high temperature films or vice versa.⁵⁸ Rough substrate regions, for instance, can precipitate the formation of a Zone 1 structure even on very hot substrates because of preferential nucleation. In these cases the individual Zone 1 grains may recrystallize and look like Zone 3 grains, but the film as a whole will retain the porous nature of Zone 1 microstructure. Very oblique deposition can also drive Zone 1 growth because of shadowing as discussed in the previous section. As mentioned above, film stress can cause the opposite effect, the early formation of high temperature microstructures.

Growth Mode Models

Film growth is usually divided into three modes based on the type of coalescence exhibited as the film grows. In crystal growth literature these are known as the layer (or Frank van der Merwe) mode, the island (or Volmer-Weber) mode, and the mixed island on layer (or Stranski-Krastanov) mode. Adsorption studies are more cryptic, usually calling these types I, III, and II growth modes.²⁶ Each of these modes applies to a different set of film, substrate and deposition parameters, but all of them are characterized by the same four stages of film growth.^{27,60} However, before any film can form at all there must be a supersaturation of evaporant atoms over the substrate to overcome the high vapor pressure of small groups of adatoms on the substrate and provide a driving force for nucleation. As explained above, the need for nucleation to occur before film formation can begin is a result of the kinetic barrier to film growth on perfect substrates. A source of excess energy is typically needed before evaporant atoms will adhere to a substrate permanently and this is provided by the energy of the critical nucleus. Naturally defects on the substrate can provide this excess energy just as well, circumventing the need for nucleation.²⁶

The first stage of film growth is the initial nucleation stage often called the island stage.^{26,27} In this stage monatomic adatoms first assemble into critical clusters and form permanent film islands.

These are often three-dimensional, but lateral growth is usually much greater. Early nuclei often have well defined triangular crystallographic shapes, though this did not appear to be true of the nickel films in this research. A few small islands were observed to be triangular, but most were just elongated droplets. Nucleation is usually detected by a sudden profusion of small nuclei, 10 to 30 Å in diameter. While STM can easily detect film aggregates smaller than this, the smallest clusters observed in air were in this range.

The second stage is coalescence, where film islands grow together to form larger structures and begin to form a significant cover on the substrate.²⁷ Coalescence of individual atoms is a rapid process, often taking less than a tenth of a second. This is far too fast to observe with STM even if it were in situ. However, it is possible to observe coalescence frozen at the end of the deposition process. Often coalescence is liquid-like with well defined islands merging into a blob before gradually regaining their crystallographic triangular or hexagonal shape. Liquid coalescence is driven by the reduction in surface energy which results from the reduced surface area to volume ratio of one large island compared with two smaller ones. The actual coalescence is achieved by surface diffusion, cluster mobility and, at higher temperatures, bulk diffusion. Taking on a proper crystallographic shape also reduces energy somewhat. In most film systems there is a certain island shape and height to diameter ratio that is optimal and minimizes island energy. Substrate coverage is actually reduced immediately after islands coalesce, commensurate with the increased height of the new deposit. This phase is followed by a more gradual island growth from accumulation of mobile adatoms and incoming flux atoms. A few researchers have reported that coalescence is preceded by a bridging of the gap between the islands by a thin ribbon of film material, however this idea has been largely discounted by others.²⁷ Nonetheless, close inspection of STM scans has indeed revealed the presence of thin bridges between nickel islands on HOPG. These are by no means universal, but appear to occur when fairly large but equal sized islands have grown in close proximity. This behavior is similar to the channel filling discussed below and indicates that the small region between any islands that are sufficiently close together can be treated as a channel.

As the coalescence stage proceeds, substrate coverage becomes significant and the individual islands become quite large. At this point they are separated only by thin strips of open substrate, so this phase

is known as the channel stage.²⁷ These channels often contain small islands that are continually being swept up by the large bounding islands and replaced by new atoms from the impinging flux. These form secondary nuclei on the substrate areas bared by surface area reduction following incorporation of a small island into a much larger one. Liquid-like behavior persists at this stage, with channels being bridged by fingers of film material and then rapidly filled by a shallow layer of film. The channel coverage thickens more slowly, forming grooves in the film with faceted boundaries.

At some average thickness the film becomes basically continuous, although perhaps marred by a few holes. For nickel this stage happens at a very low coverage and few holes are observed. As a result the channel stage is very short-lived and is sometimes not observed at all. The islands that have grown to make up the film start with random plane orientations, but recrystallization during coalescence reduces these mismatches, enlarging the film grain in the process. At room temperature some 100 or more initial nuclei may combine to form a single grain. For the fine grained structure of the nickel films in this study though it is more likely that only about 10 nuclei are responsible for each grain of the final film.

No study of film growth modes would be accurate without considering the effects of incorporating defects into the film. Even under the most perfect conditions on the most perfect substrates a considerable number of defects occur which become part of the final film.²⁷ No attempt was made to identify film defects in this research so only a brief review is attempted here, a detailed review of the subject is deferred to existing literature. If no substrate defects are present, the initial film islands that form are generally perfect single crystals. However as they grow and touch, lattice defects and grain boundaries are introduced and incorporated into the film. It is possible to grow a film as a single crystal, but not with simple e-gun deposition equipment. Substrate defects can also disrupt single crystal growth by introducing defects of their own. The most common defects observed in the films studied were diffuse grain boundaries where the film would be rough and poorly formed. Large dislocation loops were also observed in a few cases, especially as the films aged. Smaller defects were no doubt in abundance, but they were not explicitly searched for.

In view of all the possible ways to disturb film growth just discussed, it is perhaps not surprising that layer growth is rarely observed, even when it is the intended growth mode.⁶³ Layer by layer growth

can be disturbed by anything which perturbs the smooth addition of film material from the first adsorbed atoms to the bulk film.²⁶ Indeed it was not observed at all in the films studied here.

Since it requires limited layered growth, the Stranski-Krastanov growth mode was not expected either but it was observed in a few exceptional instances. Marked by the nucleation of islands atop a monolayer of film material, this mode requires high quality substrates, well matched film and substrate materials, and undisrupted film growth. It is also commonly associated with large nucleation barriers and large critical nuclei, 7-10 atoms at least.²⁶ It was observed twice on large 2-D islands of nickel growing on a good quality HOPG substrate underlayer.

By far the most common growth mode observed was Volmer-Weber island growth. This mode is precipitated by strain, lattice mismatch, crystal type mismatch or even orientation mismatch between a film material and substrate with the same crystal structure. These conditions also lower nucleation barriers and critical nuclei size. In fact, single atom critical nuclei are quite common when island type growth is observed.²⁶ Molecular dynamics models of film growth reinforce these expectations, predicting pure Volmer-Weber growth for FCC film-substrate systems with lattice mismatches greater than 19% regardless of how strong the film-substrate interaction is.⁶³

The nickel films studied in this research exhibited some strain and their FCC (111) structure differed somewhat from the HCP (0001) structure of the HOPG, but the major factor contributing to the observed island type of growth was the huge 43% lateral lattice constant mismatch between nickel and HOPG. Nickel normally exists as an FCC structure with a lattice constant of 3.5238 Å while HOPG is hexagonal with a lattice constant of 2.4614 Å.⁶⁵ STM observations of the ZYH grade of HOPG used in this research has shown this value to vary by up to 20% from unit cell to unit cell though. Fortunately, the closest approach distance for nickel atoms, 2.491 Å,⁶⁵ is small enough to allow nickel atoms to occupy the vacant central sites above HOPG unit cells if they are only slightly distorted. Moreover, free nickel dimers can have bond lengths as short as 2 Å and small vacuum deposited clusters have average atomic separations not much greater.⁶⁶ Thus a small nickel cluster could easily form directly on the HOPG surface by assuming a tighter FCC structure than normal. As the cluster grew the bonds would lengthen and eventually the bulk FCC structure would appear. By then the cluster would have sufficient energy of its own to remain bound to the HOPG despite the large lattice

mismatch. However, it is obvious that the first nickel film layers will be stressed. High resolution STM scans of small 2-D nickel islands support this view, revealing compressed nickel spacings at the edge of islands and normal 3.5 Å bond lengths at the center. Detailed results will be presented in Chapter 5 along with rest of the STM data.

A number of other factors can play a role in the type of film growth observed. One of these is suppressed nucleation on perfect crystal planes. As discussed previously, islands tend to start out two-dimensional and only gain appreciable height after coalescing. This would be expected if surface diffusion was strong because the islands would accumulate more atoms adatoms along their boundaries than flux atoms on their upper surface. For metal films though two-dimensional islands are common even in temperature regimes where surface diffusion is almost non-existent. In these cases the defect free crystal planes of the 2-D islands discourage adatom incorporation because doing so would increase the surface energy of the island. In fact 2-D island formation is often driven by the difficulty of adding atoms to perfect crystal planes.²⁶ Three-dimensional growth is delayed until a defect appears on the 2-D island or flat terrace unless an adatom cluster forms which is large enough to overcome the nucleation barrier. In the later case growth is no longer purely island type, but rather is of the hybrid Stranski-Krastanov type.

Another important feature of growth on HOPG substrates is preferential nucleation along steps. Steps are the most common form of defect on HOPG, rarely being separated by more than 5 μm on the ZYH grade material used. Enhanced nickel build-up along the top side of these steps is almost universal on the films studied. Clusters or thin ribbons of nickel form along these features and grow out onto the adjacent flat graphite terraces much faster than nuclei form on the terraces directly. Film growth on rough areas of HOPG thus largely short circuits nucleation, forming droplet-like above step defects and coalescing into large deposits very rapidly.

Nucleation

The final microstructure of a film is quite dependent on the very earliest stages of deposition when adatoms first form stable nuclei. As a result, a careful study of this phase of film development can yield a vast amount of information about the physical properties of the film. Unfortunately quantitative data has been difficult to obtain in the past, but the use of STM simplifies matters greatly. It allows film islands to be studied in groups and cataloged or viewed individually in atomic detail. These "island demographics" can then be turned into hard information on the nucleation behavior of the film as a function of the experimental variables including substrate temperature, deposition rate, deposition angle and so forth.

Studies of nucleation center around two parameters, the critical nucleus size and the nucleation rate. From a thermodynamic standpoint, the critical nucleus size, i^* , is simply the largest collection of film atoms that is still in local equilibrium with the population of single adatoms. It follows then that under equilibrium conditions critical nuclei have the largest free energy of any cluster size.²⁶ They are likewise the least common cluster size. Above critical size, stable clusters form when an adatom joins a critical nuclei. Individual adatoms can also re-evaporate before joining a critical cluster or be swept up by other growing stable clusters. In the case of nickel, the critical nucleus size is usually just one atom, so the smallest stable cluster is a dimer.

The nucleation rate relates the critical cluster size to the deposition conditions and the energy parameters of the film-substrate system. Usually the nucleation rate equation can only be expressed as one of a family of coupled kinetic rate equations, but in the case where only monatomic adatoms are mobile, such as is the case with nickel films, a great number of simplifications apply. This system is best modeled by the coupled rate equations first introduced by Zinsmeister of which there are only three for $i^* = 1$ systems. These are the single adatom concentration, the nucleation rate and the growth rate of stable clusters.²⁶ Working with only the nucleation rate equation it is possible to divine information about i^* or activation energies by making some simple assumptions. Since nickel films have $i^* = 1$, the critical cluster binding energy, E_i , is simply zero. Thus the nucleation rate equation can be

used to determine the activation energies for surface diffusion, E_d , and re-evaporation of adatoms, E_a . The exact form of the equation depends on whether the islands being studied are 2-D or 3-D, and if film condensation is complete or not.²⁶ Film condensation is considered complete if re-evaporation of adatoms is negligible and the sticking coefficient for evaporant atoms is close to unity. Incomplete condensation covers the broad range of other possibilities where re-evaporation of adatoms is appreciable and the sticking coefficient is less than one. This usually occurs at elevated temperatures. A generalized form of the nucleation rate equation is given below and the variable parameters are listed in Table 3-1 below.

$$\dot{I}^* = Ra_0 y N_0 \cdot (R/N_0 \nu)^p \cdot \exp(E/kT) \quad (3-3)$$

where \dot{I}^* is the nucleation rate, R is impingement rate, a_0 is the adsorbed monomer jump distance which can be approximated by the lattice spacing of the substrate, y is the average linear substrate periphery outside the capture zone of each island that is available for nucleation, N_0 is the density of adsorption sites on the substrate which is often equated to the monolayer density of the substrate, ν is the frequency of substrate lattice vibrations ($\approx 10^{13}$ Hz), p is a variable parameter given in Table 3-1, E is a variable energy parameter also given in Table 3-1, k is the familiar Boltzmann constant, and

Table 3-1 Nucleation rate equation variable parameters for various condensation regimes.

Regime	3-D Islands	2-D Islands
Extremely Incomplete Condensation	$p = 2i/3$ $E = (2/3) \cdot (E_i + (i+1)E_a - E_d)$	$p = i$ $E = (E_i + (i+1)E_a - E_d)$
Initially Incomplete Condensation	$p = 2i/5$ $E = (2/5) \cdot (E_i + iE_a)$	$p = i/2$ $E = 1/2(E_i + iE_a)$
Complete Condensation	$p = i/(i+5/2)$ $E = (E_i + iE_d)/(i+5/2)$	$p = i/(i+2)$ $E = (E_i + iE_d)/(i+2)$

lastly T is the substrate temperature.²⁷ Note that the instantaneous nucleation rate will change with time while equation (3-3) above represents the average nucleation rate over the entire time the film is deposited. In point of fact, almost all nucleation occurs very early in a deposition when the adatom population is at its peak.

Another important nucleation predictor is the reciprocal temperature dependence of N_{∞} , the saturation density of stable nuclei. A positive slope to the plot indicates that nucleation is complete, a negative slope that it is incomplete.^{26,27} The temperature at which the slope changes sign is the critical condensation temperature, T_0 , where condensation first becomes incomplete. Abrupt changes in slope without a change in sign indicate temperatures where the critical nucleus size changes, say from one atom to two or two atoms to three. For critical nuclei larger than about 5 atoms no significant slope changes will be observable.

In order to utilize the nucleation rate equation and determine N_{∞} , it is necessary to convert raw "island demographics" into the necessary nucleation parameters.²⁷ Doing so requires several steps which are best understood if the nucleation theory behind them is reviewed first. There are two basic ways to look at nucleation, as a bulk phenomenon or as an atomic level phenomenon. The bulk approach is more intuitive and works better when the critical nucleus size is large, during Stranski-Krastanov and layer growth. The atomic view is more successful when the critical nucleus size is small, as it is for Volmer-Weber growth. For the nickel films studied, the atomic approach is sensible since $i^* = 1$. However, it is still best to touch on the bulk approach to nucleation first. An excellent review of both theories is presented by Neugebauer²⁷ and his approach is followed closely below.

Known as the capillarity or droplet model because it deals with film aggregates as geometric shapes (droplets) instead of collections of atoms, the bulk approach is the classical method for analyzing nucleation.²⁷ Paradoxically it was put forward by Volmer and Weber among others, yet it rarely applies to the growth mode named after them. It centers around the bulk surface Gibbs free energies to the nucleation process beginning with the Gibbs free energy of the cluster with respect to disassociation, ΔG , which depends on the volume, surface area, substrate contact area and free energy of condensation of the film material in the bulk. The critical cluster size, r_* , and free energy, ΔG^* , can be found by calculating the maximum free energy as a function of cluster radius, r , from

$$\partial \Delta G / \partial r = 0 \quad (3-4)$$

The density of critical nuclei is then given simply by

$$n^* = R \cdot \exp(-\Delta G^* / kT) \quad (3-5)$$

neglecting the small Zeldovich factor which converts equilibrium cluster populations to steady-state cluster populations.^{27,60} The nucleation frequency in this case is

$$I^* = CR \cdot \exp[(\Delta G_{des} - \Delta G_{sd} - \Delta G^*) / kT] \quad (3-6)$$

where C is the nucleus shape dependence, ΔG_{des} is the Gibbs free energy of activation for monomer desorption, and ΔG_{sd} is the Gibbs free energy of activation for surface diffusion. These last two energies correspond the atomic energies E_a and E_d respectively.

The atomic model on the other hand depends on atom-specific energies instead of the bulk surface energies because the latter do not strictly apply to tiny droplets of material. The only real difference between the models is that the atomic model uses discrete atom arrangements instead of modeling nuclei as geometric droplets.²⁷ For example ΔG in the droplet model is the free energy to form clusters with respect to the gas phase. The equivalent atomic model term is E_i , the energy released by disassociating an i atom cluster in monomers. As a result the atomic model is ideally suited to cases where the critical nucleus is small, as is the case for nickel films on HOPG.

The best place to start analyzing the atomic nucleation model is with the question of complete or incomplete condensation. If essentially all of the evaporant atoms that impinge on a surface stick, then the sticking coefficient is unity and condensation is complete. At higher temperatures though re-evaporation of adatoms is significant so the sticking coefficient is less than one and condensation is incomplete. However, only atoms that are outside the influence of stable deposits on the surface are subject to re-evaporation. Within a certain radius, r_s , of stable deposits, known as the capture zone, adatoms are gathered into the growing deposit and cannot re-evaporate. This distance is determined by the surface diffusion coefficient, D , and the mean residence time, τ_a , of adatoms on the surface from

$$r_s = \sqrt{D\tau_a}. \quad (3-7)$$

The fraction of the substrate covered by stable clusters and capture zones is then given, as a function of time, by

$$F(t) = N(t)D\tau_a, \quad (3-8)$$

where $N(t)$ is the density of stable clusters on the surface. The rate at which new nuclei are forming is, per $\text{cm}^2 \cdot \text{s}$,

$$dN(t)/dt = \dot{I}^* [1 - F(t)], \quad (3-9)$$

where the coverage function is given explicitly by,

$$F(t) = 1 - \exp(-\dot{I}^* D\tau_a t) \quad (3-10)$$

and the density of clusters on the substrate surface is given explicitly by

$$N(t) = (1/D\tau_a) \cdot [1 - \exp(-\dot{I}^* D\tau_a t)]. \quad (3-11)$$

Naturally all of these equations only apply to the island stage of nucleation before coalescence starts and disturbs the island distribution. Before coalescence begins though, the density of nuclei on the surface saturates. This saturation density, N_∞ , is dependent on \dot{I}^* and τ_a and approaches

$$N_\infty = 1/D\tau_a \quad (3-12)$$

as complete saturation is achieved.

The time-dependent substrate coverage $F(t)$ can be roughly equated to the instantaneous sticking coefficient, α_s , and this leads to powerful relationships between N_∞ , which is observable with STM, and the nucleation rate, \dot{I}^* , which is necessary for application of equation (3-3) to film nucleation behavior. The instantaneous sticking coefficient is simply the amount of mass deposited at one instant divided by the mass impingement rate on the substrate,

$$\alpha_s = (dM/dt)/M \quad (3-13)$$

Setting α_s equal to $F(t)$ and integrating,

$$M(t) = M_\infty [(t + \exp(-\dot{I}^* D\tau_a t) - 1)/(\dot{I}^* D\tau_a)]. \quad (3-14)$$

After a sufficiently long period, $t > 3/(\dot{I}^* D\tau_a) \geq 3 \text{ s}$, $M(t)$ can be approximated by the much simpler expression

$$M = M_\infty [1 - 1/(\dot{I}^* D\tau_a)]. \quad (3-15)$$

By substituting equation (3-12) then \dot{I}^* can be calculated from known or observable values as

$$\dot{I}^* = N_\infty / (1 - M(t)/M). \quad (3-16)$$

Thus it is possible to determine the nucleation rate, and hence calculate various activation energies using equation (3-3), knowing only the deposition rate, mass deposited, and the saturation density of

nuclei on the substrate.²⁷ Care must be taken however when investigating low nucleation rates, below 10^9 per $\text{cm}^2 \cdot \text{s}$, that nucleation near defects is not driving the nuclei population distribution and true nucleation is occurring. The nickel films studied exhibited sufficiently high nucleation rates to prevent this, but it was still necessary to avoid areas of the HOPG that had large numbers of defects.

Equation (3-16) allows the nucleation rate equation (3-3) to be used easily, but it is often still necessary to make some assumptions. Chief among these is the size of the critical nucleus. This is easy for nickel films, but often the question is open, especially when wide temperature ranges are involved. The transition from one critical size range to another can be calculated rather easily however by simply equating the applicable forms of (3-3) across the boundary. At the $i^* = 1$ to $i^* = 2$ boundary for instance the transition temperature in the incomplete growth regime for 2-D islands is given by

$$T_{1-2} = -(E_d + E_2)/[k \cdot \ln(R/\nu N_0)]. \quad (3-17)$$

Here E_2 is the binding energy of a two atom cluster, which is 2.7 eV for a nickel dimer.⁶⁵ Nickel films retain a one atom critical nucleus up to at least $T_{1-2} \approx 1250^\circ\text{C}$ for any reasonable deposition parameters. Thus for this research $i^* = 1$ is always assumed for nickel films.

It should be pointed out that as cluster size increases, there will often be more than one way to arrange the atoms in the cluster. This complicates calculation of the correct, minimum, value for E_i . The straight-forward equation below simplifies this process for the small clusters appropriate to the atomic treatment of nucleation.²⁷

$$E_i = X_i E_b - h E_a \quad (3-18)$$

where E_b is the nearest neighbor bond strength, X_i is the number of inter-atomic bonds and h is the number of atoms not in contact with the substrate.

Finally it should be pointed out that all of the formulations above assume the re-evaporation of super-critical aggregates is totally negligible. Zinsmeister (as quoted by Neugebauer)²⁷ points out that this is not always the case, but for high boiling point films such as nickel where a two atom cluster is stable against re-evaporation, this assumption is quite safe.

Film Stability

Because the films used in this research were studied in air for a period of some months following their deposition, it is possible that some artifacts could have been produced in the film structure. On a bulk scale, minor breakdown of some of the films was noted after about three months of aging in air. Stress tears and dislocation loops were the usual defects, but damage from handling also built up over time. Dust contamination was also a problem, but it could usually be cured with ozone-safe canned air. Chemical contamination, especially oxidation, was not observed to be a problem. High humidity brought on by the rainy "monsoon" season in Arizona did make STM scans more difficult. It appeared as though the samples adsorbed a thin layer of water over the graphite areas, probably hydrogen side down and oxygen up. This layer acted as an insulator, but could be easily swept aside by the electric field of the STM during scanning. However doing so required increasing the bias voltage somewhat to avoid a loss of resolution.

A more subtle concern was the loss of extremely small nickel islands from the nucleation regions of the films due to exposure to the atmosphere. As mentioned earlier, real nickel films are observed to have critical nucleus sizes of only one atom range when deposited and analyzed in vacuum. However, the stability of such small clusters in air at room temperature is doubtful. Indeed, atomic resolution scans did not reveal any nickel clusters smaller than 7 to 10 atoms.

CHAPTER IV

FABRICATION AND CHARACTERIZATION OF THIN NICKEL FILMS

This chapter is devoted to discussing the equipment and techniques used to deposit and characterize thin nickel films for this thesis. First, the deposition of the nickel films themselves is described, including sections on the vacuum system, substrate and source materials, deposition techniques and film handling. The Nanoscope® II STM system used for primary film analysis is then described in detail, followed by a brief review of the more conventional thin film analysis equipment used to complement the STM results.

Nickel Film Deposition

Since STM was central to this thesis, it was necessary to modify normal film deposition procedures somewhat to produce films well suited to STM study. This requirement limited the choice of substrates to conductive materials that could be imaged with STM and suggested fabrication of films with thickness gradients produced by shadowing of the substrate. The films could then be imaged by STM at several points along the thickness gradient to yield information about film formation and microstructure at different phases of development.

The Vacuum System

Almost all of the films used in these experiments were deposited in a bell jar evaporation system which had initially been used for aluminizing telescope mirrors but which had recently been used for the deposition of a variety of films including cadmium sulfide, cadmium sulfoselenide, and aluminum oxide.⁶⁷ The bell jar was an 18"x18" Pyrex piece mounted on a stainless steel collar sporting seven 2.75" flanges and nine 1" feedthroughs. Vacuum was provided by a 4 inch diffusion pump with LN_2 cold trap backed by a rotary mechanical pump. This combination was capable of base pressures below 2.0×10^{-7} Torr as measured by an ion gauge mounted just above the cold trap. A complete diagram of the vacuum system is shown in Figure (4.1). Since the presence of dirty contaminants like sulfur and selenium could have degraded performance, a series of thick nickel depositions were performed to cure any problems. The presence of cadmium in the system was also of concern because of its toxicity. To minimize risk, the vacuum system was placed under a large fume hood and all work on it was performed with gloves and dust masks. In addition special attention was paid to washing exposed limbs after working on the vacuum system.

The system was equipped with two sources, a custom built 10 V, 100 A resistive source and an Airco-Temescal TIH-180 electron beam gun (e-gun) with a 2.5 cm^3 hearth capacity driven by a 4 kV, 750 mA Thermionics Perma-Beam 150 power supply. This supply was limited to 30 A of filament heating current and so could only utilize relatively thin e-gun filaments. Only the e-gun was used for these nickel film depositions. The two sources were separated by a water cooled steel barrier previously needed to prevent the e-gun from heating the resistive evaporation material. Deposition progress was monitored by a water cooled quartz crystal monitor (Xtal or XTM) mounted about 9 inches directly above the e-gun. This monitor viewed the e-gun only through an aperture previously installed to prevent it from recording evaporant from the resistive source during codepositions.⁶⁷

The e-gun power supply had been modified to accept dynamic feedback control from the Inficon XTC deposition controller used to drive the e-gun crystal monitor.⁶⁷ This allowed for programmed control of e-gun operation that eliminated the wild fluctuations in source material evaporation rates caused by rapidly changing melt geometry typical during e-gun depositions.

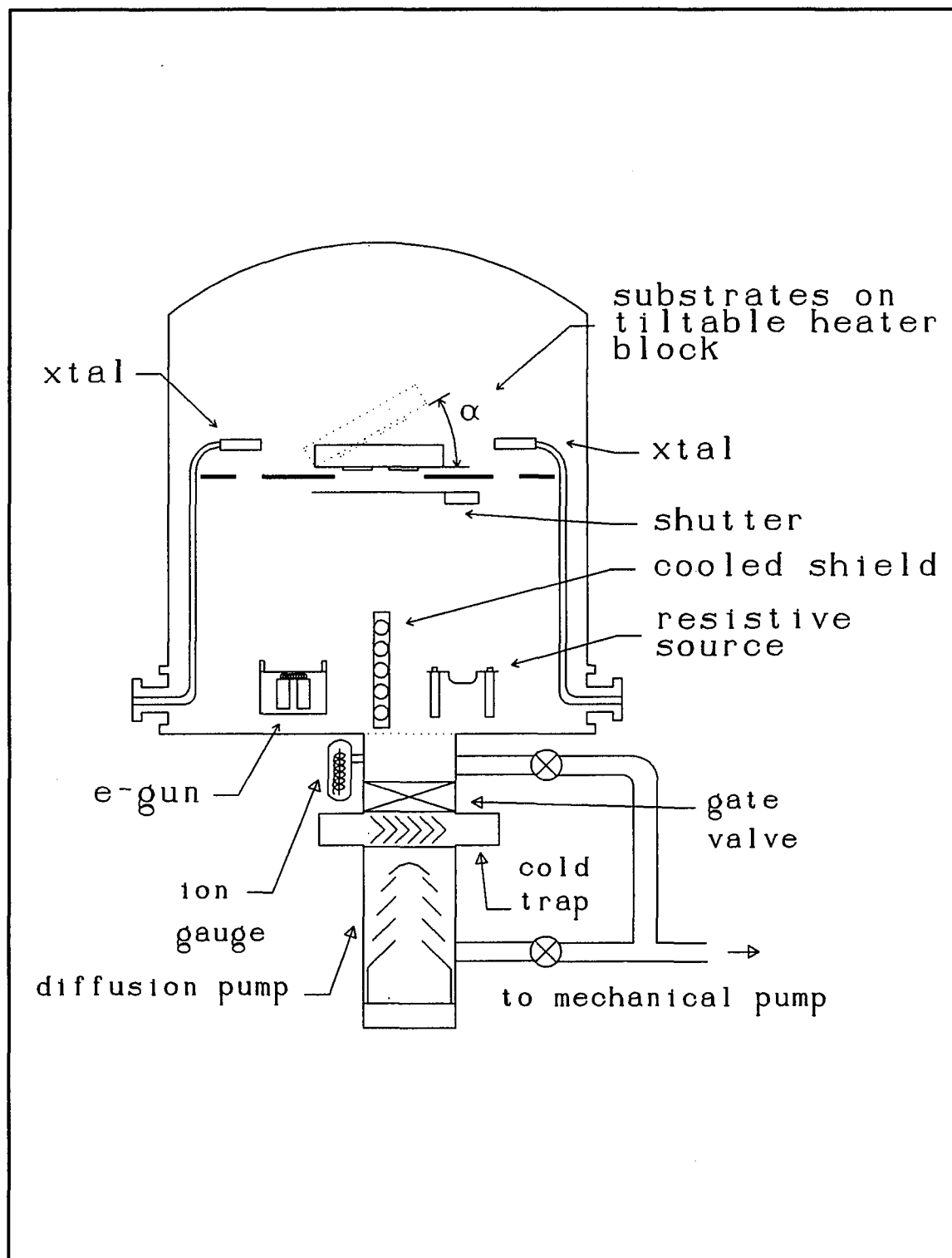


Figure 4.1 The vacuum system used to deposit most of the nickel films used in this research (from F. Suits, 1988).⁶⁷

The XTC is capable of complete deposition process control for one source including ramping power up in stages to achieve a stable rate, shutter opening, deposition of a preset film thickness, shutter closing, and power down.⁶⁸ With a little experimentation all manual intervention can be eliminated, however, manual override is always available.

Dynamic feedback control with the XTC is adjusted via a gain parameter, α , which can range from 1-99% and determines how quickly the XTC changes e-gun power in response to variations from the preset deposition rate. The XTC control signal can be expressed as

$$V_{e\text{-gun}}(t) = \int_0^t \alpha[r_0 - r(t')]dt', \quad (4-1)$$

where r_0 is the rate setpoint and $r(t')$ is the rate as measured by the crystal monitor. If the e-gun is initially at zero power then, it will start to ramp up as

$$V_{e\text{-gun}}(t) = \alpha r_0 t. \quad (4-2)$$

Thus if α is set too high, the e-gun will ramp up quickly and overshoot the desired rate producing chaotic rate oscillations. If α is too low, the e-gun will not respond fast enough to changing melt conditions and the actual deposition rate will depart from the preset value for significant amounts of time. Appropriate gain values vary widely depending on the nature of the deposition, but in general materials that melt well require lower gains than materials that sublime.^{67,68}

Substrates were mounted on a molybdenum block threaded with alumina insulated tungsten wire to allow heating of the substrates up to 600°C. Despite the large thermal inertia of this block, it was still possible to accomplish rapid heating, equilibrium temperatures of 200°C being attainable in about an hour. Masks screwed to the heater block were used to hold the substrates in place. These provided better thermal contact between the substrates and the heater block than simply attaching the substrates with screws, held the substrates with more uniform pressure, and served to keep deposited material off the heater block itself.⁶⁷ However, the aluminum mask used to hold shadow masks over highly-oriented pyrolytic graphite (HOPG) substrates during deposition effectively limited heating of HOPG substrates to 350°C to prevent warping of the aluminum. The entire holder could be tilted up to 80° for angle of deposition studies, using a protractor and plumb bob for calibration. The heating block was also drilled out in the center to just below the substrate face so that a thermocouple lead could be attached to monitor temperature. However, the thermocouple would often simply be placed under the

unused half of the substrate holder mask to more closely approximate the thermal contact between the heater block and the actual substrate. To protect the substrates during e-gun warm up, the whole heater block was shielded from the e-gun hearth by a large motor-driven shutter.

Materials and Preparation

The nickel source material used in the e-gun for these experiments was all from one batch of 99.9% pure metal in the form of crude spheres ranging from 1/4" to 1/2" in diameter which was purchased from Cerac. This material proved to be quite satisfactory but was difficult to condition initially because of a high gas content. Early melts showed a tendency to spit until heated to well past normal evaporation temperatures to allow for complete outgassing. In addition, a few nickel depositions were done by dc magnetron sputtering on float glass and silicon (111) substrates. These films, and some resistively evaporated films deposited by a fellow researcher, provided a source of external data with which to compare the electron beam films.

Nickel films were chosen for examination because they are well suited for STM study and because fellow researchers were already engaged in related studies of nickel film properties. Nickel films are easy to deposit and they do not tend to oxidize extensively at room temperature in atmosphere as do iron and aluminum films.¹⁸ This is critical to STM imaging of the films in air. In addition nickel film growth and microstructure formation have been explored by conventional means providing a sizeable body of information to compare with and help analyze STM images.²⁸

The primary substrate in all of these investigations was highly-oriented pyrolytic graphite (HOPG) obtained from Union Carbide. This material was initially intended for use as monochromator crystals in X-ray diffractometers, but is equally well suited to STM use. Like all pyrolytic carbon, HOPG is grown by thermal decomposition of hydrocarbons in the absence of oxygen.²¹ The high crystal quality is obtained by using premium materials and firing at very high temperatures, above 3000°C. The various grades of this HOPG are differentiated by the degree of mosaic spread they impart to a beam of X-rays when used as monochromator crystals.⁶⁹ The spread reflects the amount of disorder present in the graphite and in turn provides a relative measure of the surface quality of the material. The most

common grade of graphite used was ZYH, characterized by mosaic spread of $3.5 \pm 1.5^\circ$. This grade made a satisfactory substrate but suffered from atomic step defects and relatively numerous microscopic surface faults. A small piece of near perfect ZYA HOPG with a mosaic spread of $0.4 \pm 0.1^\circ$ was used as a reference to calibrate the STM. All graphite substrates were prepared from 12x12x2 mm pieces of HOPG by razor cleaving. Typically one 2 mm thick piece would yield three or four substrates. Cleaved pieces with rough edges were trimmed with a razor. Messy pieces were recleaved with tape (the Scotch Magic Tape variety is preferred) in the fashion now standard in STM circles.⁴³

HOPG was chosen for this application because it has been so exhaustively studied by STM that atomic images of HOPG are a standard by which instrument performance can be judged.^{3,44,45} HOPG surfaces are characterized by atomically flat regions up to 1000 \AA^2 separated by nanometer scale steps⁵ and occasional large surface faults and defects. In many ways it is perfect for nucleation studies using STM because it is easy to differentiate between film nucleation sites and the structure of the underlying HOPG. At high resolution it is possible to image the atomic structure of HOPG with STM, making it a simple matter to distinguish nickel film growth on the surface. Unfortunately the large number of surface discontinuities make it nearly impossible to employ optical surface profilometry or any other interferometric tests on HOPG surfaces even when coated with reflective thin films.

Fused silica was used as secondary substrate because it is commonly used in thin film studies and because its surface properties were more uniform on a macroscopic scale. The material chosen was a moderately uniform grade of Vitreosil from Thermal American cut into 25x25x1 mm plates. Films on these substrates were amenable to optical surface profiling and could be more easily compared to existing literature. The most common defects observed on these substrates were grooves produced during production or polishing.⁷⁰

Neither of these substrates reacted with the nickel films to any significant extent, even at elevated temperatures. Nickel on HOPG might be expected to form NiC, but this only occurs in restricted circumstances and never to a great extent.^{18,66} As mentioned above, nickel oxidation is also quite limited, especially under vacuum or in air at room temperature. Residual sulfur in the vacuum system could be a source of nickel film corrosion, but since time in the vacuum system was limited, the effect should be minimal. This is especially true since the films were never exposed to temperatures above

643°C, the melting point of the eutectic formed between nickel and the sulfide Ni_3S_2 .¹⁸ However, the long periods for which the films were exposed to air could have resulted in some surface contamination by sulfur. Since fused silica is extremely stable at the deposition temperatures used, no interaction with the nickel film is expected in these studies.⁷⁰

Since the HOPG provided by Union Carbide was packed clean at the factory and was cleaved before use, no special cleaning was needed prior to deposition except for blowing with dry nitrogen to remove dust. However, care was required in handling the substrates during loading to prevent contamination at that point. STM scans of bare substrates revealed the presence of occasional piles of "crud" on the surfaces, but it was not clear if this represented surface contamination or just areas of graphite disordered during cleaving. Tape cleaving left more of a residue but this did not appear to materially affect the film studies. Various STM studies have been performed on tape cleaved HOPG before without any notice of ill effects.^{6,43}

The fused silica substrates on the other hand did require cleaning prior to use. The complete process used is described below (from F. Suits).⁶⁷

1. Wearing polyurethane gloves, clean both sides of the substrate with Liquinox soap using a few minutes of circular action with a cotton swab.
2. Use tweezers to place the substrate in an ultrasonic bath of dilute Liquinox for 30 minutes.
3. Using tweezers, rinse the substrate thoroughly in DI water.
4. Submerge the substrate in Chromerge under a fume hood, heat the solution to 80°C on a hot plate, and bathe at temperature for 30 minutes.
5. Flush the Chromerge coated substrate in DI water for 5 minutes.
6. Place the substrate on a rack submerged in warm DI water and clean ultrasonically for 30 minutes.
7. Rinse the substrate briefly in running DI water and immediately blow with dry, filtered nitrogen using a downward gas flow so the water quickly collects at the bottom of the substrate and drips off.

8. Place the clean substrate in a desiccator for storage.

The intention of the Liquinox soap cleaning is to remove organic contamination, so if the substrates appeared clean with no visible grime, spots or streaks the initial Liquinox cleaning was omitted. The Chromerge bath is then supposed to remove both the soap film and any inorganic contaminants on the substrate. Additional soap cleaning or methanol rinses are therefore not necessary and may actually do more to contaminate the substrate than to clean it.

The glass and silicon substrates used in the dc-sputtering comparison films also required cleaning prior to deposition. The silicon was subjected to an HF etch followed by ion pre-cleaning in vacuum while the float glass was cleaned with soap and solvents to remove organic grime. An acid etch to remove inorganic contaminants was not used because it tended to roughen the glass surface too much.

Once any of these substrates was loaded, it was necessary to quickly pump down since no further cleaning could be performed. The availability of ion pre-cleaning would have been nice for the fused silica, but likely would have done more harm than good to the delicate atomically flat surface of HOPG. Clean room wet lab facilities would also have been beneficial, but even without them film quality was more than adequate.

Shadowing

A large number of the films made on HOPG substrates were shadowed to yield a thickness gradient from continuous film coverage down to bare substrate. This was done to produce a variety of film growth stages from initial nucleation to complete film microstructure on one sample for direct comparison. The shadowing was accomplished by installing a piece of stainless steel or HOPG over the substrate at about a 30° angle to form a kind of loose mask. As exact and repeatable positioning was difficult, shadowed regions varied in width from sample to sample. The HOPG masks seemed to produce longer, more reproducible thickness gradients, especially at elevated temperatures. In any case STM scans allowed easy categorization of film growth stages across the thickness profile so variations in shadow width were not critical.

Deposition Procedures

In many thin film studies information about film deposition is limited at best and little or no account is taken of subtle issues such as substrate mounting, temperature monitoring, and anomalous interactions between instruments in the vacuum chamber.

One point of concern is the difference in temperature between the surface of the substrate and the location of the thermocouple.⁶⁷ This difference can be quite substantial if the substrate is a poor thermal conductor, is being radiatively heated by the e-gun, or is in poor contact with the heater block. In addition, poor thermocouple contact can also lead to erroneous temperature readings. These effects have previously been measured in the vacuum system used for this research.⁶⁷ To do so the normal substrate thermocouple was mounted in the hole in the back of the heater block and a second thermocouple was attached to the face of a fused silica substrate with low temperature indium solder. Both thermocouples were then monitored during two aluminum oxide evaporation runs, one with the substrate at room temperature, and one with it stabilized at 140°C. The results are shown in Figure (4.2). Note that the substrate temperature was observed to rise above the temperature of the heater block when the shutter was opened, with the effect being more pronounced at room temperature. Because evaporating nickel requires considerably less e-gun power than evaporating aluminum oxide, radiative heating, and hence the temperature difference, should be reduced in this research. The additional step of securing the thermocouple leads between the heater block and substrate holder masks should reduce this difference even further.

Another issue to address is the level of various contaminants in the vacuum system. This is of special concern in this case because of the presence of dirty contaminants such as sulfur and selenium and highly toxic materials like cadmium. The system background had previously been analyzed with a Spectramass SM100D Residual Gas Analyzer (RGA) after pumping down for several hours.⁶⁷ The detailed partial pressure spectrum is shown in Figure (4.3) and confirms the presence of small amounts of sulfur and selenium along with the usual complement of light gases and hydrocarbons.

Finally, the usual procedures followed during a deposition run should be discussed. To begin, clean substrates were blown off with dry, filtered nitrogen and then mounted on the heater block outside the

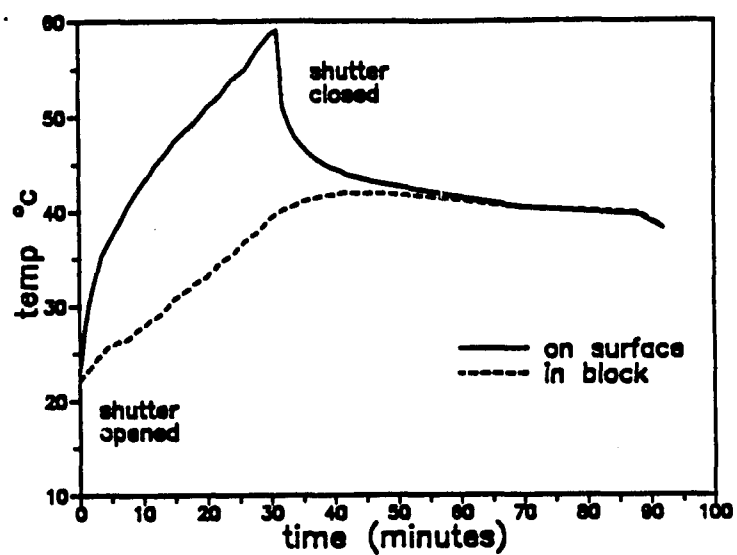
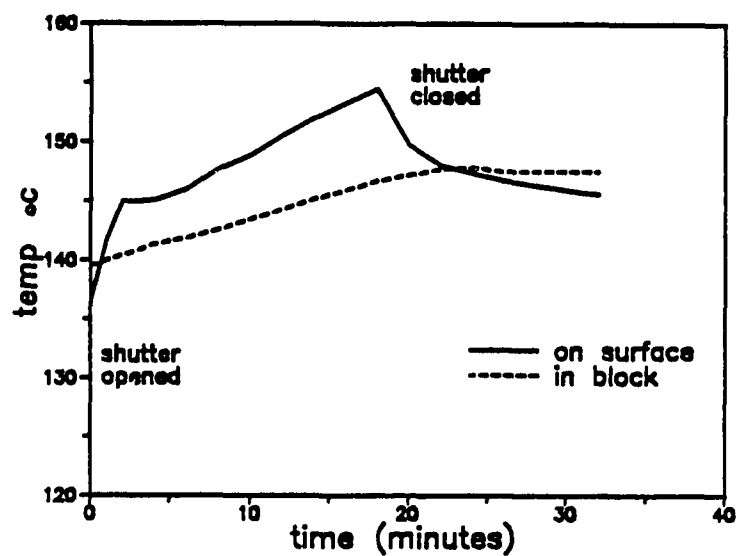


Figure 4.2 Temperatures on the surface of a fused silica substrate and within the molybdenum heater block during e-gun depositions of Al_2O_3 at room temperature and 140°C (from F. Suits, 1988).⁶⁷

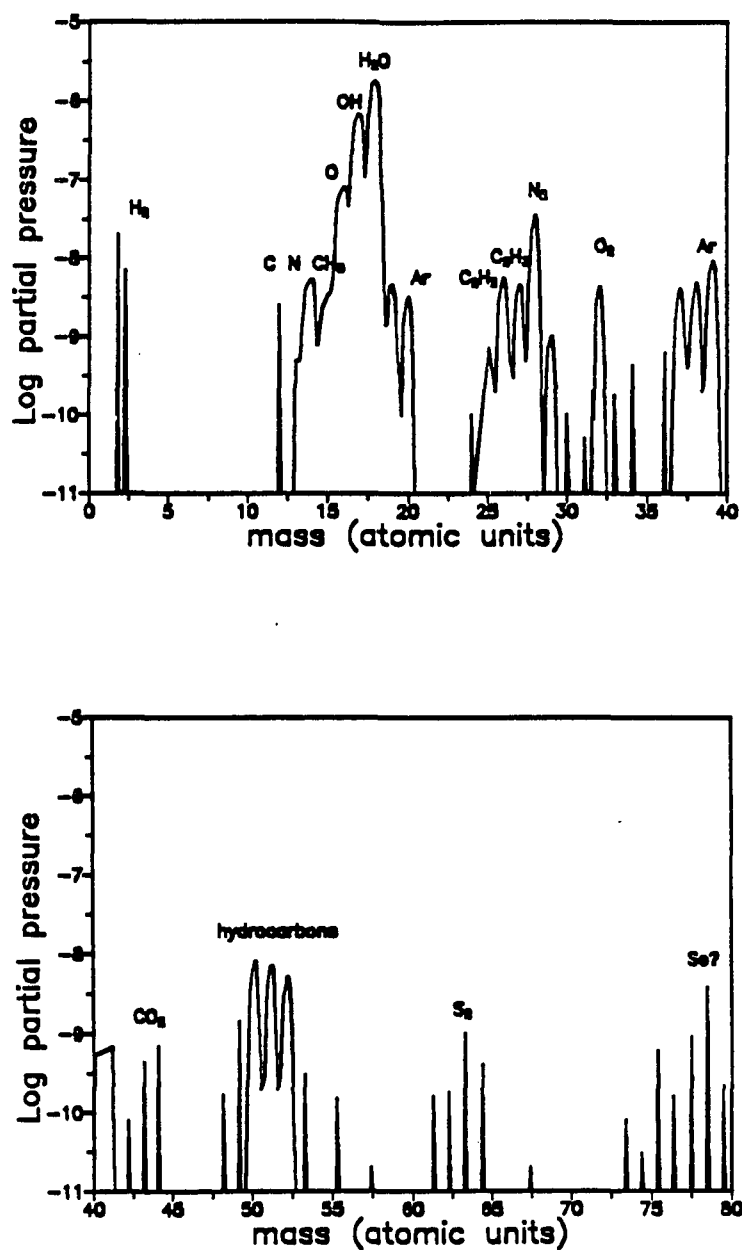


Figure 4.3 RGA spectrum of background gas partial pressures in the vacuum system after pumping for three hours (from F. Suits, 1988).⁶⁷

vacuum system and hastily placed in the chamber. The heater, thermocouple, and substrate tilt attachments were made at this time and pumpdown was commenced as soon as possible to minimize contamination of the substrates. For room temperature evaporations about one hour was allowed for pumping, usually resulting in a pressure below 3.0×10^{-7} Torr. For heated runs, pumping continued until the substrate reached the required temperature and equilibrated for thirty minutes, a process sometimes requiring four or five hours for high temperature runs. The deposition was then performed under XTC control. Afterwards the system was allowed to cool to room temperature before being opened. Completed films were then removed from the heater block outside the system and stored in small plastic sample boxes.

Film Handling

Once outside the system the sample films were stored at room temperature and atmospheric pressure. No special effort was made to keep them dust free although they were handled with care to keep them free from fingerprints. All handling was done with tweezers, but gloves were not usually used. Ozone safe canned air or dry nitrogen was used to blow any dust particles off the films each time they were analyzed. Over time the films did show some wear from handling, mostly scratches from the tweezers, but all such damage was quite local in nature as shown by the STM scan of a scratch shown in Figure (4.4).

Scanning Tunneling Microscope Operation

Seeing as most STM's are custom built and vary widely in their operation and capabilities, it is necessary to discuss in some detail how the Nanoscope® II STM used for this research operates and how it was utilized. As this instrument is sold commercially its construction and operation are in some ways superior, or at least better integrated, than is typical. At the same time however the manufacturer

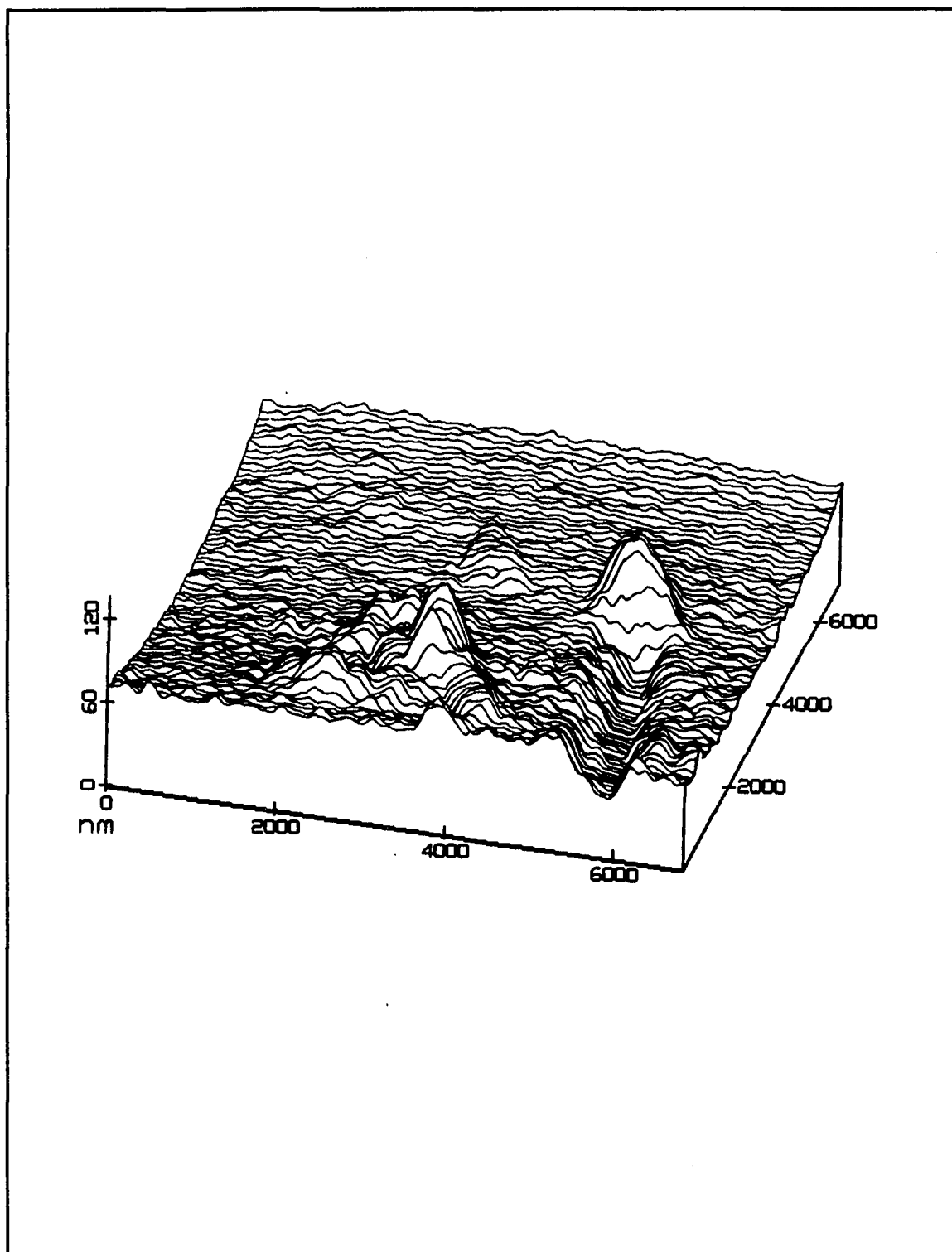


Figure 4.4 STM lineplot image of a region of nickel film showing a scratch caused by handling the film. Notice the pile of film material at the end of the scratch.

naturally does not wish to publicly divulge everything about the design of the instrument so comparatively less is known about the internal workings of the Nanoscope® II than would be known about an instrument built in-house.

The Nanoscope® II System

The Nanoscope® II is a computerized STM produced and sold by Digital Instruments of Santa Barbara, California. It has been available commercially for a couple of years and has been used successfully by other researchers. It was designed from the older Nanoscope® I STM also sold by Digital Instruments. The Nanoscope® I is a manually controlled instrument capable of producing only analog output -- usually a full screen trace on a storage oscilloscope. Both instruments use very similar microscope heads, all of them being based on a design originally developed at the University of California at Berkeley. Virtually all of the STM data for this thesis was produced by the Nanoscope® II, although some early work was done on a Nanoscope® I.

The Nanoscope® II design itself is quite modular, consisting of a microscope unit, a control unit, and an IBM AT compatible (Intel 80386 based) computer which actually runs the instrument. A schematic of this layout is shown in Figure (4.5) to help illustrate this brief overview of the instrument, most of which is condensed from the Nanoscope® II operation manual.⁴⁸ Computer software drives the control unit through an interface board, taking data and displaying images in real time. The software also performs off-line signal processing and data analysis. A Sky 321 digital signal processor (DSP) is used to provide real time dynamic feedback control of the tip. The control unit is split into two parts, an X-Y board and a Z board, with the former consisting only of the 16 bit digital to analog converters (DAC) that translate signals from the computer into X-Y raster scans of the tip. The Z board handles all the other control functions including providing bias voltage, reading tip tunneling current via a 12-bit analog-to-digital converter (ADC), controlling the z position of the tip, and running the stepper motor during fine approach of the tip towards the surface. The signal from the ADC is used directly by the Sky 321 DSP to calculate the dynamic feedback response used in controlling the z position of the tip. If tunneling current is being imaged the ADC output is also stored as data,

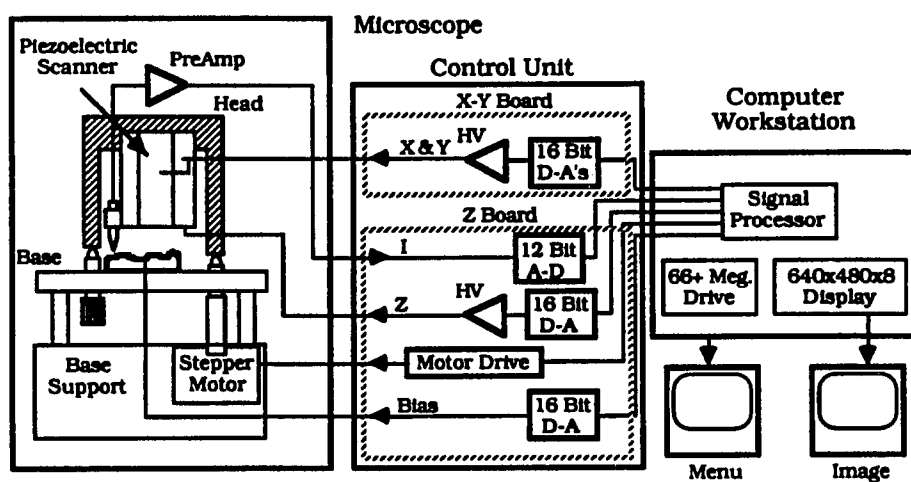


Figure 4.5 Block diagram of the layout of the Nanoscope II (from *Digital Instruments, 1989*).⁴⁸

otherwise the change in the z position of the tip determined by the DSP feedback response is stored as z-height data for the surface being scanned. During spectroscopic scans the ADC and feedback signals are manipulated further before being stored as data.

The microscope unit itself consists of four major sections: a lower stainless steel housing, an upper housing which is supported by teflon tubes for vibration isolation, a sample base, and the microscope head. A photograph of the whole assembly is shown in Figure (4.6). The lower housing holds the low torque stepper motor used for fine advance of the tip into tunneling range of the surface. The upper housing includes the sample base which contains the two fine pitch screws for rough tip advance and a flexible shaft connecting the stepper motor to its drive screw. The microscope head is magnetically coupled onto ball bearings atop these three drive screws. Two sample bases were available, one fixed, the other allowing sample motions of ± 1 mm in both X and Y. Simple micrometers were used to control this motion, yielding a resolution of about 5 microns. With a little dexterity it was possible to safely move the sample while tunneling was in progress. Samples are held in place on the bases with a small V-clip. The microscope head itself consists of the piezoelectric actuator, the preamp and the tip. Two heads were available during this research, one for atomic imaging capable of scans up to 500 \AA^2 , and one for large scans up to $6.5 \mu\text{m}^2$. The upper portion of the microscope could be covered with a hood during use to help eliminate acoustic vibration problems.

All of the upper microscope parts are set in Invar to reduce thermal distortions of the tunneling gap. Without the Invar, thermal expansion mismatches between the piezo crystal and the metal shell would cause intolerable tunneling gap instabilities if operating temperatures varied by as little as 1°C during a scan. With the Invar variations of as much as 10°C can be withstood.⁴⁸

Digital Instruments uses an unique Pentrode™ piezo design in its microscope heads.⁴⁸ A variation on the single tube piezo introduced by Binning in 1986,⁷¹ it uses a hollow single piezo tube wired for $\pm X$, $\pm Y$, and Z control. The piezo materials used are not disclosed by Digital Instruments. The small, light tip holder is mounted on the front of this assembly, slightly encumbering the piezo in the Y direction and typical resulting in a reduced Y voltage sensitivity for the head.

Amplification of the output from the tip is handled in a extremely simple manner involving only one preamp.⁴⁸ The preamp consists of one FET, wired as a non-inverting amplifier with a gain of 100 and



Figure 4.6 A photograph of the whole microscope unit including the large scan head.

a cutoff frequency of 15 KHz, following a 1 M Ω resistor. The tip is coupled to the input of this FET and to ground across the 1 M Ω resistor, yielding a transimpedance gain of 100 mV/nA. The preamp is Johnson noise limited with an rms voltage noise of 2 mV, equivalent to 0.02 nA of noise on the input current. The disadvantage of this arrangement is that the actual tunneling voltage trails the nominal value set by the software by 1 mV per nA of tunneling current. Fortunately, the Nanoscope® II software automatically compensates for this discrepancy during scanning.

Tunneling voltages in this system are always read sample to tip so that positive tunneling voltage means the tip is negative with respect to the sample and electrons flow from the tip to the sample.⁴⁸ The available voltage range is ± 10 V in 0.3 mV steps low pass filtered with an RC time constant of 0.1 ms. Tunneling current is limited to ± 48 nA, but values above a few nA are not physically necessary.

Regardless of their origin, all STM designs depend on a feedback system to maintain tunneling gap stability during scanning. The Nanoscope® II uses a Sky 321 digital signal processor to accomplish this, reading the instantaneous tunneling current and adjusting the z piezo voltage to compensate for changes in current. This system is easily capable of keeping the tunneling gap steady within 20%, so the vertical resolution of the Nanoscope® II is a respectable 0.2 Å or better. Feedback is controlled by three gain parameters: proportional gain, integral gain, and 2-D gain. Primary feedback control is usually maintained by the integral gain which integrates the variation of the tunneling current from its set point over time, acting to keep the tip tracking over the surface. The higher this gain value, the longer the integration time and hence the tighter the surface tracking. Too low a setting can cause the tip to drift away from the surface while too high a setting can lead to tip oscillation. Secondary control is managed by the proportional gain which reads instantaneous current variations and directly modifies the tip Z position to bring the tunneling current back to its set point. This helps stabilize the feedback circuit and improves response time at high frequencies. Setting the proportional gain opposite the integral gain can also be used to cancel the effect that oscillating the bias voltage during spectroscopic scans has on the feedback response. Higher gains here lead to the use of a larger fraction of the difference between the actual and setpoint currents in modifying tip position. Low proportional gains can result in sluggish tip response to surface features possibly leading to a tip crash while high gain values cause rapid jumps of the tip which add high frequency "fuzz" to scans. A third level of feedback tuning is

called 2-D feedback because it improves tracking on surfaces that are similar from one scan line to the next, like most atomic images. It works by predicting tip Z position in the current scan line based on tip Z position at the same point in the previous scan line. Higher 2-D gain values use a larger fraction of the difference between the present tip height and the Z position at the same point in the previous scan line to predict the current Z position. Thus 2-D gain values only range from 0 to 1, which is not true of the other gain values. Large gains are highly predictive which is helpful in atomic scans but can cause unwanted oscillations in large scans. Low gain values are not actually detrimental, but a small amount of 2-D gain is usually needed to optimize the performance of the feedback loop. For example, atomic scans of graphite typically use a 2-D gain of 0.7 while most large scans only need a setting of 0.3. Taken together, the settings of these gain parameters define the response of the tip to variations in the surface height or electrochemical properties of the surface. Several rules of thumb apply to setting these values, but optimizing feedback for a given scan or a particular sample remains a difficult task requiring considerable perseverance.

Vibration isolation for the Nanoscope® II is primarily provided by a trio of elastic bungee cords hung from an oversized camera tripod supporting a flat concrete slab on which the microscope unit rests during scanning. Under the weight of the microscope and slab the bungee cords deform by a foot or more, yielding a resonant frequency of approximately 1 Hz, quite sufficient to damp out typical building vibrations. Secondary vibration isolation is provided by the teflon tubes supporting the upper microscope assembly and the hood used to shield the head from acoustic vibrations. Further isolation is achieved by careful design of the microscope head itself. The rough positioning screws are decoupled from external vibrations during use by the teflon tubes while the flexible stepper motor shaft serves to decouple the fine tip advance mechanism when the stepper motor is disengaged. The use of a low torque stepper motor also reduces vibrations during tip approach. The efficacy of this system is demonstrated by its ability to maintain atomic-resolution tunneling in a normal lab environment despite the usual noise, commotion, and occasional heavy equipment use.

Calibration

While the microscope heads arrived from the factory already calibrated, it was desired to cross-check the values before using the heads. In addition, occasional checks were needed to insure that the piezos were not drifting out of calibration. The small scan head piezos typically had lateral sensitivities of 15 to 25 Å/V, yielding maximum scan sizes of at least 500 Å² when using the full ±150 V of the Nanoscope® II piezo drivers. The large scan head had sensitivities around 275 Å/V providing scan sizes of 6.5 μm². The Z sensitivities of the piezos were somewhat different, about 20 Å/V for the small head and about 100 Å/V for the large head. Because of the Pentrode™ design of the piezo electrodes discussed above, all microscope heads suffered from slightly lower voltage sensitivities in the Y direction compared to the X direction.

Lateral calibration procedures for the two heads differ because of their divergent scan sizes.⁴⁸ The small head was well suited to atomic imaging so it was calibrated by scanning HOPG at high resolution and recording an image containing several well formed hexagonal atomic patterns. The unit cell spacing in these structures is known to be nominally 2.46 Å, so calibration is simply a matter of scaling the spacing observed with the instrument to the known spacing value in both the X and Y directions. The scale factor is then used to adjust the previous sensitivity values. The large head can resolve atoms on HOPG, but not with sufficient detail for calibration. Besides, it is usually used at the large end of its scan range so it is instead calibrated using a grating ruled on a gold film. This grating has a nominal periodicity of 1 μm, several repetitions of which can be imaged in a single scan by the large head. Simply scaling the observed spacing of the rulings to the known value accomplishes the calibration. Note that two scans must be taken in this case, one with the rulings positioned in the X direction and one with them in the Y direction. Head calibrations are stored by the Nanoscope® II computer and are used to automatically scale images. If several iterations of the calibration procedure are performed it is possible to achieve a calibration uncertainty of as little as 5 percent.

Vertical calibration of the heads is a trickier and less accurate proposition since it depends on the exact shape of the tip used. The operation begins with pulsing the stepper motor an even number of times and recording the change in the Z piezo voltage reading. This yields a Z piezo sensitivity in

volts/step, V_s . Converting this to $\text{\AA}/V$ can then be done crudely by assuming a typical sensitivity of 500 $\text{\AA}/\text{step}$ for the stepper motor. A more accurate calibration can be obtained by determining the mechanical disadvantage (MA) of the stepper motor in combination with each head. This is the distance from the point of the tip to the line between the coarse positing screws divided by the distance from the same line to the stepper motor drive screw which is the same for all heads at 0.65 inches. The MA is usually near 0.125 but it depends of the exact position of the point of the tip in use and thus varies from tip to tip somewhat. The final vertical calibration is then

$$Z_{\text{cal}} = (4000)(\text{MA})/V_s \text{ [in } \text{\AA}/V]. \quad (4-3)$$

Due to the difficulty in accurately determining the MA this procedure is not generally as accurate as lateral calibration, with an uncertainty of 10-15% being likely. Vertical calibration can also be performed by scanning features of known vertical extent such as the poly-balls used in electron microscopy, but even then significant uncertainty remains because of variations in the sizes of the individual calibration objects.

Note that all of these calibration concerns apply only to absolute scaling of STM images. In all dimensions the relative sizes of objects in STM scans are extremely well known, being limited only by the resolution of the instrument or the data acquisition system.

Tips

The quality of the tips used with a STM can have a dramatic effect on the usefulness of the results it produces because tip quality directly affects lateral resolution. To insure repeatable tip quality, all of the tips used in this research were purchased directly from Digital Instruments, even though it would have been possible to manufacture tungsten tips in the lab. As a result, very little is known about the processes used to produce these tips. Both platinum-iridium and tungsten tips were purchased. The former were mechanically formed, probably by grinding or cutting, while the later were chemically etched so any one of a number of effective techniques could have been employed. Because all STM work was done in air, tips made of $\text{Pt}_{0.8}\text{Ir}_{0.2}$ alloy were preferred for their contamination resistance. They are excellent for atomic work under any conditions,^{46,48} but since they are mechanically formed

they are irregular in shape and rarely symmetric. This can be detrimental in scanning large features because tip response can vary with scan direction and feature geometry. The typical problem is that tall surface features appear different in forward and backward scan lines. Problems of this kind were only noted on a few occasions using these tips. Tungsten tips were used on a limited basis, but because of their tendency to become dirty and oxidized in air it was necessary to store them in a desiccator prior to use. When no obvious improvement in image quality was noted, they were judged too troublesome and their use was discontinued. SEM micrographs of a typical $\text{Pt}_{0.8}\text{Ir}_{0.2}$ tip are shown in Figures (4.7) and (4.8).

Because the great majority of tips purchased from Digital Instruments were observed to work properly, the usual process of examining the tips under a microscope was deemed unnecessary. Since changing tips is so easy with the Nanoscope® II it was more productive to try the tips out. If the resulting images were noisy, unstable, or appeared to contain artifacts, the tip was just replaced.

Sample Requirements

The relatively small size of the Nanoscope® II microscope heads limited the size of the sample platform, often requiring the use of uncomfortably small sample dimensions. Sample width was limited to 12 mm, length to about 40 mm, and thickness to less than 3 mm. Thus it was quite often necessary to cleave or cut samples before using the STM. This was the primary reason for using 12 mm square HOPG substrates throughout these experiments.

Sample conductivity was not such a problem. A very large range of materials can be scanned by the Nanoscope® II, although samples with resistances above 1 M Ω require bias voltages greater than 100 mV. A number of tricks are available to improve tunneling on some otherwise marginal surfaces. One favorite is the use of diffusion pump oil as a coating to stabilize surfaces and isolate them from the air. This approach even allowed freshly cleaned silicon surfaces to be scanned in air, albeit only well above atomic resolution. Grounding samples to the sample base with silver paint was also useful when scanning high-resistance metal surfaces such as partially oxidized silver. A interesting recent

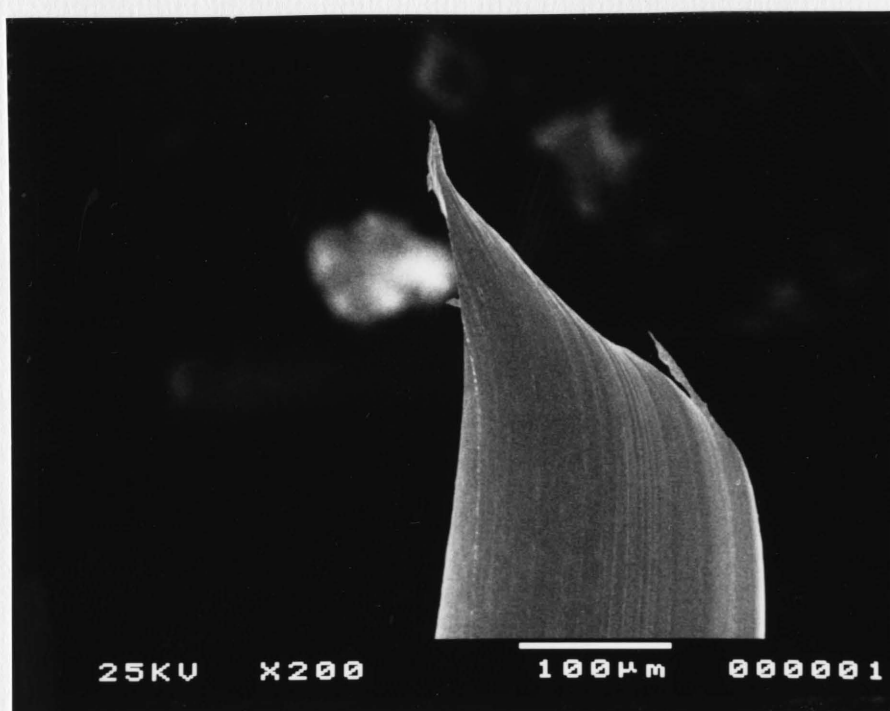


Figure 4.7 SEM micrograph of a typical Pt_{0.8}Ir_{0.2} tip in good condition taken at 200X.

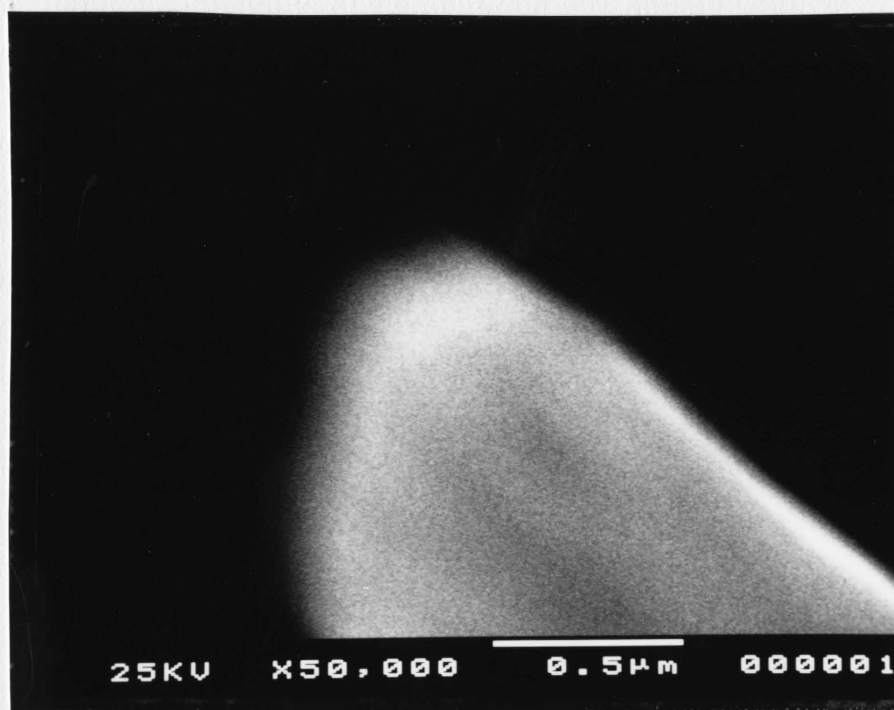


Figure 4.8 High magnification SEM micrograph of the end of the tip shown in Figure (4.7).

development is the use of the Nanoscope® II to scan films in cross section by using TEM preparation techniques to make substrate-film/film-substrate sandwich samples.

Scanning Modes

Several imaging modes are available on the Nanoscope® II, including topographic (STM) scans of Z dZ and I , spectroscopic (STS or dI/dV) scans, work function profiles (dI/ds scans) and an experimental dI/dx mode where the lateral tip position is oscillated slightly during scanning. Imaging current variation maps tunneling current contours directly instead of displaying the resultant tip height variations as is done in normal STM operation. This is advantageous during atomic scans because it enhances the minute surface corrugations and improves image quality. The dI/dx mode is occasionally useful for imaging the surface topography of very noisy samples.

In addition several non-imaging spectroscopic modes were available for investigating the I - V and I - s properties of the film surfaces. These all operate by probing spectroscopic features while hovering over one point on the surface. Three modes are available, $I(V)|_{s=C}$ where bias voltage is scanned while tip height is held constant, $I(V)|_{I=C}$ where voltage is scanned while tunneling current is held constant, and $I(s)|_{V=C}$ where tip height is scanned while bias voltage is held constant. Data acquisition in the $I(V)|_{s=C}$ mode is performed by running the feedback loop briefly to establish the setpoint current and then cycling the bias voltage while measuring the tunneling current. In the $I(V)|_{I=C}$ mode data is acquired by cycling the voltage in steps and running the feedback loop between each step. At each step the voltage is modulated 16 times while I and ΔI data is gathered. Finally, in the $I(s)|_{V=C}$ mode, feedback is run to establish the setpoint current and then the tip height is cycled upward and tunneling current is measured. All of these acquisition schemes are shown graphically in Figure (4.9). In the first two modes either I , $d[\ln(I)]/d[\ln(V)]$, or $d[\ln(I)]/dV$ can be displayed as a function of V . In the third, constant bias voltage, mode either I or $\ln(I)$ can be displayed as a function of s , the scanned variable.

The bulk of this work was done using the STM mode, except for certain atomic images which tend to look better if tunneling current variation is imaged instead of surface height variation. Limited use

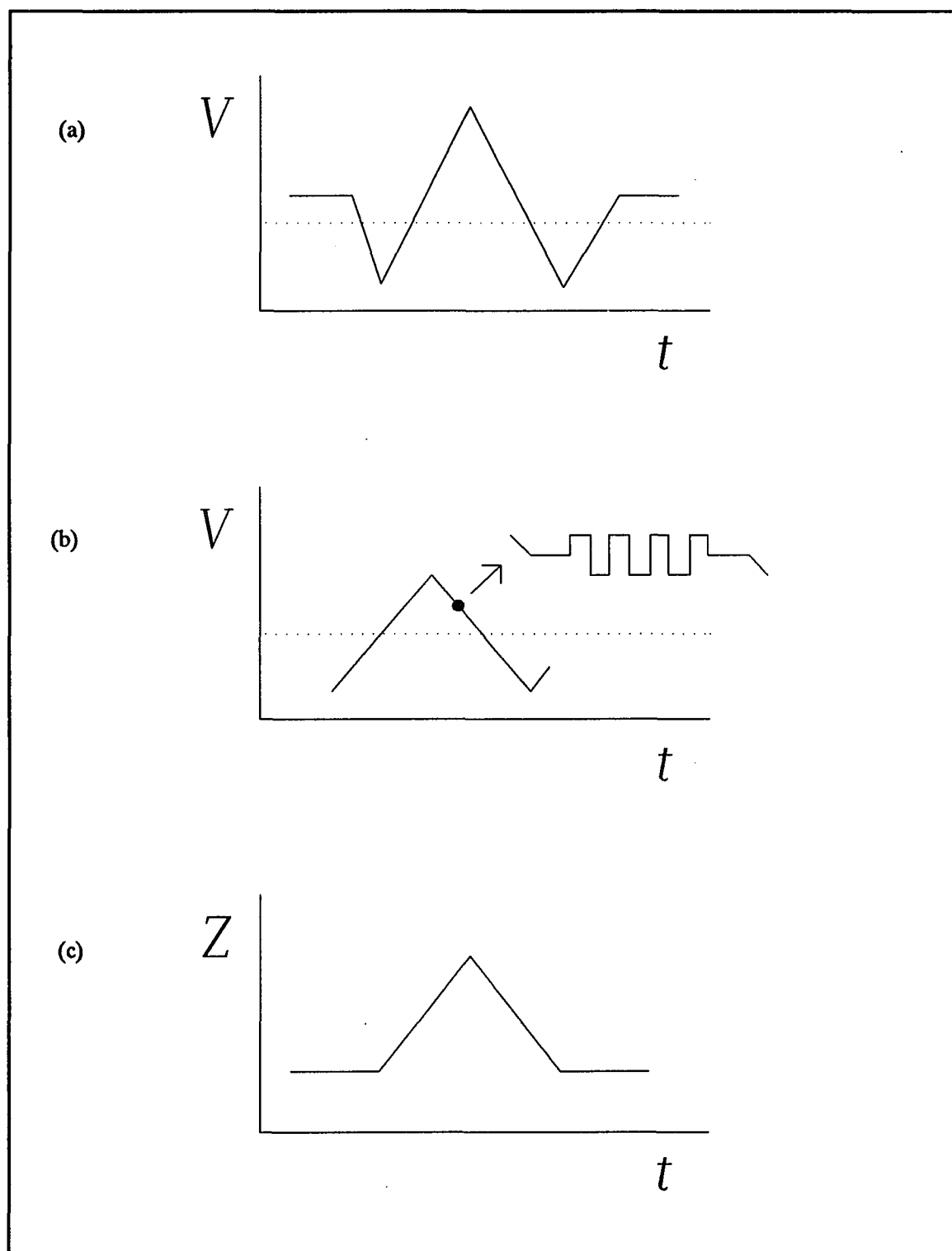


Figure 4.9 Graphical representations of the data acquisition cycles for spectroscopic plot modes a) $I(V)|_{s=C}$, b) $I(v)|_{I=C}$, and c) $I(s)|_{V=C}$ (adapted from *Digital Instruments, 1989*).⁴⁸

was made of the dI/dV , dI/ds and non-imaging spectroscopic modes as well. Imaging the derivative of the surface topography is sometimes useful in enhancing image contrast but was never needed. All of the commonly used modes have limitations on the Nanoscope® II, particularly with respect to scan speed. Limited microscope bandwidth required the use of scan speeds as low as one scan line per second during large scans, sometimes causing excessive image drift and mechanical noise. The limited bandwidth also restricts the useful scan size and available spectral range of the spectroscopic modes. Furthermore, the STM heads were not initially designed with spectroscopy in mind so dI/dV spectroscopy suffers from some residual capacitive coupling between the tip and the bias voltage, which distorts the spectra slightly.

Signal Processing

One of the best features of the Nanoscope® II is its control software, which features a wide array of filtering and display options for massaging raw scan data.⁴⁸ Almost all of the data manipulation performed on STM scans in this thesis was done with this software. The one notable exception is statistical analysis, including RMS roughness calculations. While the software was capable of calculating RMS roughness, it was found to be more convenient to use a custom written program to do so. This programming was done by the author personally using Turbo Pascal 5.0.⁷² The signal processing features of the Nanoscope® II software can be divided into two categories, image display and digital filtering. The filtering options are discussed first.

Just as with any good analog data acquisition system, the digital Nanoscope® II system allows the user a variety of common filtering options to remove noise from STM scans. All of these options are performed off-line by software which reads and modifies a copy of the raw STM data files. Nine separate functions can be performed including: lowpass, highpass, and median filtering, X-Y power spectrum editing, 2-D FFT, planefitting, image flattening, resizing, and finally inverting. The lowpass filter simply removes high frequency noise by comparing each data point to the running average of the last 2 to 8 data points and smoothing out large discrepancies. Conversely the highpass filter cuts out low frequency information by removing the average background level thus exposing the high frequency

oscillations in the data. This effect is useful in enhancing the edges of features but is limited in general usefulness because it distorts the features of the scan. Median filtering is a type of two-dimensional lowpass filtering which compares each data point to the average of its eight neighbors. The power spectrum editors calculate 1-D Fourier transforms of the data and allow parts of the spectrum to be attenuated. This is especially useful with atomic scans because the atomic periodicity shows up clearly in these spectra as strong peaks allowing almost all the extraneous noise to be removed by editing. Similarly, the 2-D FFT calculates the two-dimensional fast Fourier transform and allows it to be edited. The plane fit function automatically fits a second order polynomial to each scan line in either the X or Y direction to remove curvature. Third order polynomial fits can also be performed manually. The flatten command is somewhat similar in that it removes image bowing and mechanical noise in the Y direction by subtracting the average line height in the X direction from each scan line in the Y direction. Manual control allows the operator to specify which areas of the surface are to be used in these calculations. The resize option shrinks the STM data files from 400x400 points to 200x200 points by removing every other data point. This feature is used to conserve disk space when storing scans. It can also reconstruct 400x400 images using linear interpolation. Surprisingly, this operation preserves scans without any noticeable degradation unless they contain very minute detail. The last function, invert, simply flips all the Z data about the origin, providing a "worms-eye" view of the surface instead of the usual "birds-eye" view.

Because of the sophisticated graphics hardware used, the image display capabilities of the Nanoscope® II are almost as varied as its filtering options. At the heart of the system is a Professional Graphics Array (PGA) graphics card (Matrox PG640-A) driven by a dedicated graphics coprocessor (Texas Instruments TMS 34010 chip), which allows the Nanoscope® II to display an amazing variety of output on the color monitor provided with the system. Three basic display modes are available: topview, surfaceplot and lineplot. Topview mode is simply that, an overhead view of the data. Surfaceplot mode shows the data as a 3-D surface while lineplot mode displays separate scan lines of data as X versus Y + Z. This has the effect of revealing data that would be hidden behind hills in a true 3-D view like a surfaceplot. Both topview and surfaceplot modes allow images to be viewed either as contour maps of feature heights or as maps of illumination "reflected" by the surface under various

artificial "lighting" conditions. This latter mode closely approximates how the surface would appear in a micrograph taken with a polarizing light microscope. Lineplots always display contour maps of surface height, but only as a series of discrete scan lines. This makes it possible to get hard copies of lineplots on matrix printers whereas topview and surfaceplot hard copies can only be obtained with expensive full color printers. All images can be rotated in ninety degree steps, scaled, displayed in one of 22 color tables and annotated with a variety of important information about the scan. In addition, lineplot and surfaceplot scans can be tilted at either 30 or 60 degrees. Special mouse-driven controls allow distances, angles and surface roughness to be calculated on topview images as if they were photographs. Finally, it is also possible to magnify a section of a scan up to about 8:1 to enlarge detail.

Spectroscopic data are displayed a bit differently since STS scans contain four separate images, one topographical image and one spectroscopic image at both a high and low bias voltage setting. Small voltage oscillations are then used at each of these setpoint voltages to gather spectroscopic data. Thus it does not make sense to display all these scans together, so only one can be displayed at a time except in topview where there is the option of viewing all four simultaneously.

Conventional Film Characterization

The traditional method of studying thin film microstructure is to examine the films with both optical and electron microscopes and categorize the observations. While effective, this technique is restricted by the analog nature of the pictorial data taken and by the complications of electron microscopy. STM circumvents many of these problems with its superior surface resolution, ease of operation, elementary sample preparation and digital data acquisition for easier computer manipulation of results. However, it is still necessary to check the results of the STM scans with photomicrographs of the films. These pictures provide an important link between previous studies of thin film nucleation and growth and the STM images gathered in this study. Without them it would be more difficult to interpret the STM scans with complete confidence or to show direct relationships with the large body of published

literature. Finally, the larger areas probed by these instruments permit observation of large scale effects lost in minute STM scans.

Thickness and Roughness

Data on film thickness and roughness were obtained from several sources besides STM. A rough determination of the thickness of all sample films was made using an Alpha-Step stylus profilometer from Tencor Instruments.⁷³ This device can measure films up to about 100 μm thick with an uncertainty of ± 5 nm. It typically uses a stylus force of 15 mg dispersed over a 5 μm diameter area during measurement, which is low enough not to scratch the nickel films tested. Due to the extreme thinness of the films tested, any compression of the film by the weight of the stylus would have been well within the uncertainty of the instrument. Unfortunately, because all of the test films were quite thin, the Alpha-Step data was not particularly precise.

To make good measurements with the Alpha-Step it is necessary to have a sharp film edge such as those provided by the masks used to attach the substrates to the substrate heater during deposition. However, the mask should not be attached so securely that they damage the film edge when removed. Furthermore, good stylus profiles require nice flat substrate areas to start on, so using masks that overlap the substrates by a millimeter or more are helpful since they create the necessary take-off zone.⁶⁷ This prohibited the use of the Alpha Step on the HOPG films because large scale discontinuities on the surface of graphite make it impossible for the stylus to accurately track the surface. Finally, good stylus profiles are characterized by sharp edges and nearly flat traces over the film. Any tendency of the trace to rise or fall across the profile indicates improper profiler contact or perhaps a poor quality film.

Additional surface profilometry was done with a Wyko Topo-2D optical profiler,⁷⁴ but it was not used for film thickness measurements. Due to the discontinuous nature of the surface of HOPG on a macroscopic scale, none of the films made on HOPG could be examined with the Wyko at all, but the surface profiles of the films on float glass, fused silica, and silicon were all examined. Since the

Wyko is computer driven, it stores data digitally and can determine the power spectrum and RMS roughness of a surface as well as the thickness of a film.

The Wyko relies on optical interference to measure film properties by comparing the light reflected from the film surface with that reflected by a reference flat. Naturally this requires that the film be reflective, which was not a problem in this case. For any reasonable sample to reference spacing, interference fringes appear along contours of equal height difference between the two surfaces. By stepping the reference flat in $3/4$ wave steps, the phase of the pattern of interference fringes can be ascertained to within $\lambda/2000$, or about 0.3 nm in the vertical. The lateral resolution of the Wyko is only about 1 μm , but this is sufficient for film thickness measurements.⁷⁴

One major drawback of interferometric techniques like this is that the entire surface must produce the same phase change on reflection, since any phase changes are assumed to represent differences in the optical path between the sample surface and the reference flat. This is not a problem for a homogeneous sample, but must be considered when examining metal films on glass substrates since the two materials impart entirely different phase changes upon reflection unless the film just happens to be a multiple of $\lambda/2$ thick. The solution is to coat such samples with a metallic film thick enough to yield constant reflectance properties without changing the step height from substrate to film surface. Because this procedure is destructive it was not performed here, prohibiting the use of the Wyko to determine the thickness of the nickel films made on fused silica. However, the Wyko was used to make RMS roughness and power spectrum measurements on these samples since only film regions had to be examined to do so.

Optical Photomicrography

To get pictures showing the large scale features of both the nickel films and the HOPG substrates, a research quality Olympus BH2-MJL optical microscope complete with Nomarski capability was used. This instrument provided excellent high magnification images of the continuous film, substrate, and gradient thickness regions of the samples. Features such as the incredible density of macroscopic

surface faults present on ZYH grade HOPG were best illustrated with this equipment, as was the general shape of the film regions produced by shadowing of the HOPG substrates during deposition.

Scanning Electron Microscopy

Higher resolution micrographs were taken using a JEOL-5200 SEM with a nominal maximum resolution of 55 nm. It was hoped that this instrument could be used to complement the STM work as much as possible by imaging the same film regions as the STM. Unfortunately, the nature of the films studied greatly limited the useful results obtained. Despite employing a variety of techniques including grounding the films with silver paint, sputter coating (or "humming") the films with AuPd and tilting the sample during observation, only the grossest features of the films could be resolved. Apparently, the major problem is that such thin nickel films simply do not generate enough secondary electrons to produce a substantial image. However, close agreement between SEM photographs and STM images has been demonstrated by other researchers using more amenable samples.⁵³ Allowances must be made for the superior resolution of the STM however.

X-ray Diffraction

Diffraction studies were carried out on selected films to determine the crystalline structure of the nickel in different temperature regimes. Nickel is expected to remain in a bulk FCC structure at any temperature below melting, but this can be influenced by stress in thin film structures possibly leading to the formation of tetragonal crystals. It was also important to determine if the film had any preferred grain orientation. Most FCC metals tend to form in the (111) orientation and any deviation in the films studied would be of interest.⁷⁵

CHAPTER V

SCANNING TUNNELING MICROSCOPE RESULTS

During the course of this research it gradually became apparent that STM was capable of producing quantitative data about the formation of thin films which far exceeded early expectations. Initially it was only hoped that the superb surface resolution of the STM would ease microstructure determinations and provide some qualitative insights into the growth of thin films. Later the ability to image, count and catalog individual film islands was exploited to complete a solid quantitative study of the nucleation and growth of thin nickel films on both HOPG and to a lesser extent, fused silica.

Scanning Conditions

Nickel was chosen for this research because it resists contamination and oxidation in air, and could thus be examined with STM. It is also an important coating material in its own right. Scanning nickel in air with the STM proved to be quite simple and no major problems were experienced. Only very contamination-resistant materials like gold and graphite provide superior STM scanning properties outside of an UHV chamber.

Conductivity, Noise and Feedback

Unlike many other metals, nickel has little tendency to form an oxide in air at room temperature. In fact oxidation of nickel is usually insignificant below about 750°C unless chemical factors act to

catalyze it.¹⁸ As a result the conductivity of nickel films is quite good and no problems were encountered during STM scans. Typical scan voltages were 100-200 mV for full sized $6.5\ \mu\text{m}$ square scans and 20-50 mV for atomic resolution scans, comparable to the voltages needed to properly scan graphite. As noted earlier, a slight problem was encountered during periods of high humidity. Scan resolution dropped off markedly unless bias voltage was raised above 150 mV. Occasionally it was even necessary to scan over the surface a few times to "clean" it before high quality images could be obtained. Adsorbed water molecules were probably at fault, increasing film resistance and decreasing the quality of the scanned surface until sufficient voltage was applied to sweep the water molecules off the surface.

Scan noise was more variable and often presented a challenging problem. Over complete nickel films the only problems encountered were due to the inherent mechanical and electrical noise of the STM except where the films had sharp features. Steep islands, rough grain boundaries and the occasional hole in the film were all capable of producing line noise in scans. In all but the most extreme cases however this problem could be eliminated by adjusting the scan feedback parameters or by filtering the image. Pure graphite regions never presented a noise problem at all, but the film nucleation regions where nickel and graphite were mixed required special treatment. Since the chemical properties of nickel and graphite are quite different, crossing the boundary from one to the other often required adjustments to the scanning parameters that could not be made by dynamic feedback control alone. Optimizing the feedback for graphite led to noisy nickel regions while optimizing for nickel washed out the graphite structure. The extremely low tip ride height over graphite also presented a problem at the boundaries of nickel islands, often producing anomalous "dips" around their periphery. Because the nickel regions were usually of paramount interest, feedback was normally set close to the optimum for nickel, although it was sometimes possible to use very low feedback levels that worked well over either region.

Typical Signal Processing

For the vast majority of scans taken only one standard filtering scheme was needed. For large scans two iterations of the low pass filter, one pass of the median filter and one pass of the flattening filter usually produced excellent results. In all cases the image was plane fit to remove curvature immediately after being stored and before any other filtering was attempted. If a scan contained one or two unusually large features the flattening would be done manually to exclude the anomalous regions and prevent them from skewing the filtering. Failing to do so enhanced the X direction of the artificial dip around island-like features. Small images were usually only filtered by two passes of the low pass filter unless they contained a strong periodicity. In such cases the 1-D Fourier spectra of the scans were analyzed in X and Y, and high frequency noise was removed. This enhanced imaging of periodic atomic structure as long as the filtering was not so severe as to distort the power spectrum and remove necessary information from the scan.

Initial Nucleation

Because the island zones of the nickel films studied were produced by shadowing of the substrate, growth in these areas effectively occurred over a fairly long interval at very low deposition rates. The usual deposition time was just over 250 seconds. As a result, nucleation was quite mature in all of the films studied with most of the initial film islands having grown far beyond their critical size. Nonetheless, because coalescence had not begun in most areas, it was still possible to study the process of nucleation by extrapolating backward in time.

Substrate Structure

At this early stage of film development, the influence of the substrate on film growth is still easy to see, at least with STM, because it is possible to directly observe islands growing on substrate features. The HOPG substrate surfaces used are marred by large numbers of defects covering all size ranges from atomic structure disruptions to micron-scale ledges and canyons to grain boundaries visible to the naked eye. Micron-scale defects were the most important in large STM scans because they changed the film structure observed on a scale easily visible in the STM scans. Acting as strong sites for preferential nucleation, the upper side of ledges or canyons completely disrupted nucleation in their vicinity. Instead of the film growing from small, evenly distributed islands, in the vicinity of defects it formed rapidly from large nickel deposits which spread outward from the upper edge of defect sites across adjacent HOPG terraces. This effect is shown clearly in Figure (5.1) where large nickel deposits are shown in white existing only along a ledge and around a canyon on the surface of HOPG. In order to observe true nucleation, it was necessary to concentrate on regions where the HOPG was flat and smooth. In all but the best areas on graphite though, some substrate structure was still visible in the form of small surface ripples. These did not present a major problem but it did appear as though the island distribution was modified in small domains around these ripples. An example of rippled HOPG and the resulting distribution of nucleation islands is shown in Figure (5.2). The nickel islands appear as little droplets sprinkled on the surface and the ripples are most visible in the lower right of the photograph where the island density seems slightly higher along the top of the ripples.

Nucleation Sites

On uniform HOPG terraces nucleation appeared to occur with appropriate randomness, yielding a sprinkling of small islands across the graphite. A good example of this is shown in Figure (5.3) where the islands are shown in purple. Most of the islands are two atoms high with very flat top faces indicating that the atomic layers are near-perfect and have resisted collecting incoming evaporant atoms. Note that some of the islands have joined in the picture, although they have not actually coalesced.

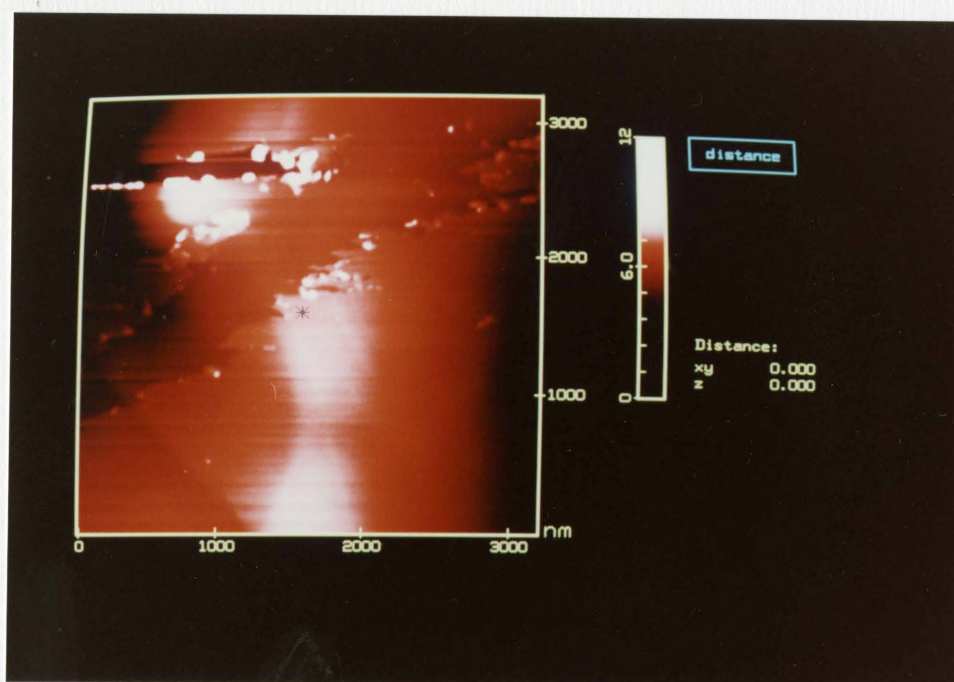


Figure 5.1 Preferential nucleation and growth of nickel deposits along the upper side of ledges and canyons on HOPG.

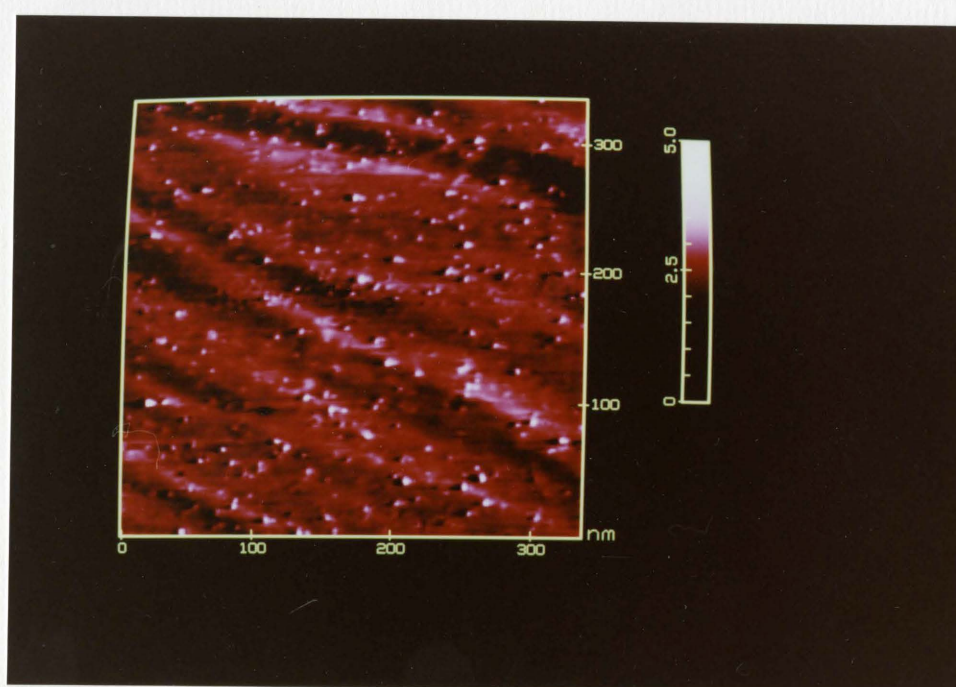


Figure 5.2 Nucleation of nickel islands on a slightly rippled section of HOPG.

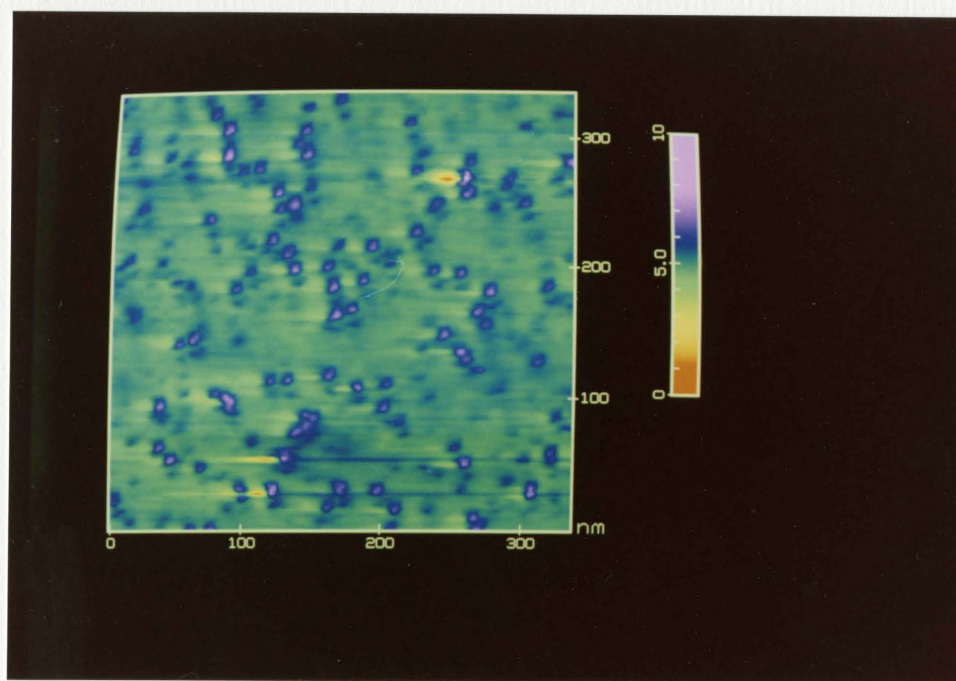


Figure 5.3 A top-view of nickel nucleation islands, shown in purple, with indications of island bridging.

Instead they have retained a two atom height and are joined by bridges, shown as a dark purple, that are only one atom high. This result is better shown in Figure (5.4) by a three-dimensional view of the same region shown only in top-view in Figure (5.3). A different style of nucleation island growth is shown in Figure (5.5) where the islands consist of a single atom layer partially topped by single atom thick clusters. Here the layer growth is probably more imperfect, allowing atoms from the evaporant flux to find a hold on the monolayer base of the islands.

The dense packing of these islands suggests that the size of their capture zones are quite small, approximately equal in magnitude to the diameter of the islands themselves, about 30 Ångstroms. Even large islands tend to be lacking a significant capture zone, as is shown clearly in Figure (5.6) by a three-dimensional view of the edge of a large island and the adjacent field of nucleation sites. The small islands appear almost right up to the base of the larger island. Also note the orange dip at the left edge of the photograph caused by overshoot of the tip as it left the nickel island and adjusted to the different tunneling behavior of the graphite surface. Note that some preferential nucleation is visible even here in the field of nucleation islands. First there is a small ledge just below the orange-colored dip where nickel is growing in a ribbon just along the top of the ledge. Second, more toward the right side of the image just below the large island edge there is a row of nucleation islands apparently growing on a small ridge on the graphite.

On a smaller scale it is possible to image nucleation islands at atomic resolution. While this is usually not possible on metal surfaces^{5,76} because of electron sharing which reduces STM resolution to about 4 Å, it was possible on a few of the very smallest one-atom tall nickel islands on HOPG. As expected though, atomic resolution was marginal. Other researchers have reported success in resolving the unit cell structure of nickel,²⁴ but not individual atoms. An example is shown in Figure (5.7) where a small nickel island about 15 Å long is imaged with marginal atomic resolution. A hexagonal array of atoms is just barely resolved in the center of the image, sitting above the washed out HOPG terrace below. It might be argued here that this island is no more than a bump of graphite, but after scanning graphite hundreds of times and consulting the literature on the subject^{5,19,20,21,22} no evidence of such features was uncovered on HOPG although similar sized features were found on less well ordered pyrolytic carbons where atomic resolution was not possible. Note that as mentioned

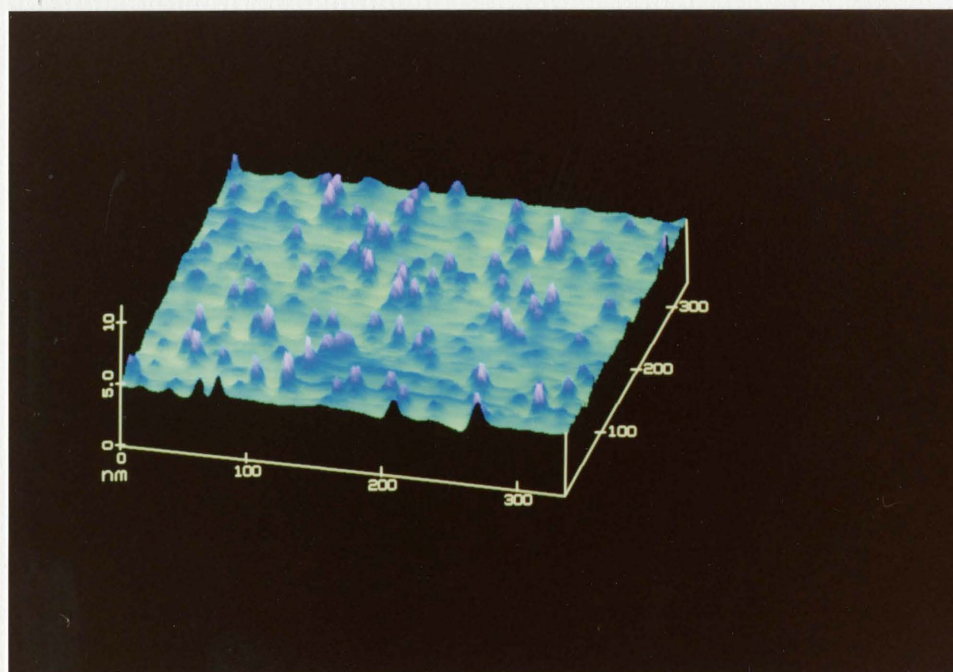


Figure 5.4 A three-dimensional view of the same nickel nucleation region shown in Figure (5.3) which reveals the occurrence of island bridging more clearly.

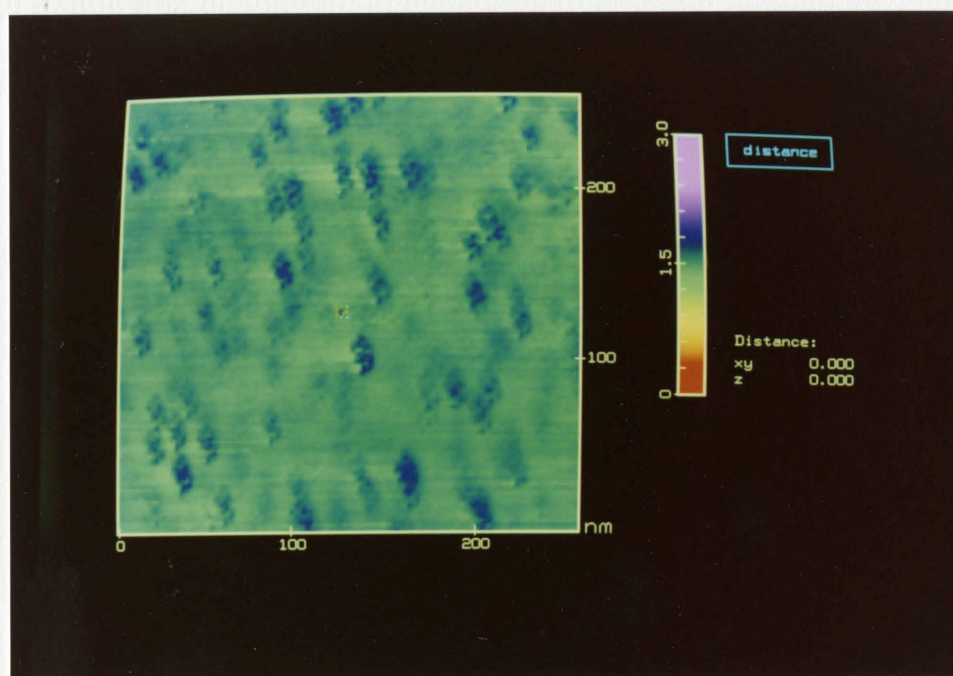


Figure 5.5 Single atom thick nucleation islands on HOPG partially covered by clusters of nickel, also only one atom thick, which form a partial second layer of atoms.

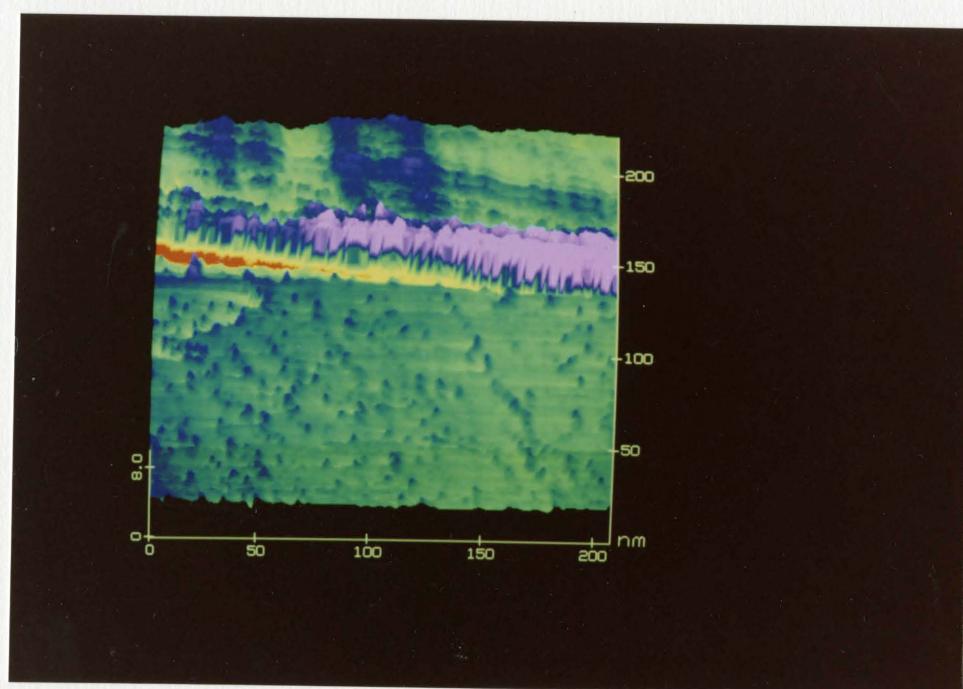


Figure 5.6 A three-dimensional view of the edge of a large island and adjacent field of small nucleation islands.

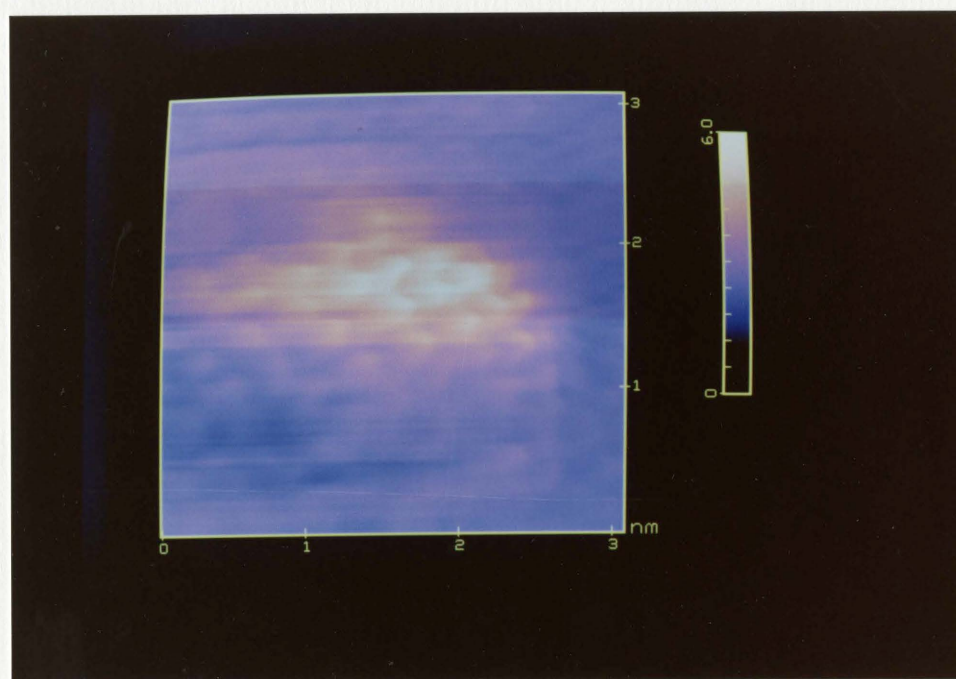


Figure 5.7 Three-dimensional view of a small nickel nucleation island showing barely resolved nickel atoms.

earlier the nickel atoms appear lower at the edge of the island than in the center. As predicted, the Ni-C and Ni-Ni bonds are compressed at the edge of the island while in the center they are closer to the bulk length of 3.5 Ångstroms. Measurements show the atomic spacing to be about 3 Å in the center of the cluster.⁶⁶ At the very edge of the cluster the nickel atoms also appear to become disorganized as if they were not yet fully integrated into the cluster. While nickel does not form a hexagonal lattice, it is possible for FCC nickel to superimpose itself directly onto the HOPG structure in extremely thin layers, as discussed in Chapter 3. The resolution of individual nickel atoms in a hexagonal pattern in this scan seems to support that view. In this regard it is quite fortunate that FCC structure is so similar to HCP, otherwise this phenomenon might not be possible.⁷⁷

Critical Nuclei

Because of the maturity of the nucleation zones on the films studied, no critically sized nuclei were expected. After all, they should be the least common after deposition is stopped anyway.²⁷ There were no surprises in this regard, no islands smaller than the one shown in Figure (5.7) were found anywhere after considerable searching. Even if some had been, identifying a nickel dimer or trimer with compressed bonds on a graphite surface would have been virtually impossible.

Quantitative Nucleation Analysis

The basic information gathered from the nucleation regions of the films studied was an island size count at various distances from the edge of the continuous film. The lateral and vertical extent of each island seen was recorded from the scan directly with the aid of a computer mouse. To insure that islands of all possible sizes were recorded, three scans were taken at each location examined. The first of these was a large scan, typically 6 μm or more on a side, which afforded the possibility of observing even large islands and surface features. The second was a one micron zoom scan taken in the center

of the large scan to cover the mid-size islands. Finally a small scan, only 250 nm on a side, was taken to record the population of small nucleation islands. This last scan was taken over the flattest, least populated area found within the initial 6 μm scan window to insure that coalescence had not begun yet. Naturally counting islands was a somewhat subjective process as it was occasionally difficult to separate islands from graphite features. Getting accurate size readings off of small islands was also difficult, even with the mouse.

The minimum observable island size was approximately a two-by-two-pixels, corresponding to 30 nm, 5 nm, and 1.25 nm minimum lateral island sizes for the three standard scan sizes. Realistically though, mouse positioning difficulties reduced the minimum measurable island size to 45, 7.5, and 2.5 nm respectively. Measurement errors varied with scan size and island height. For small islands on large scans measurement uncertainty ranged from 8-15 nm, for larger, irregular islands it could have reached 60 nm. On small scans the lateral measurement uncertainty was limited by instrument resolution to about 5 Ångströms. Medium sized scans had lateral measurement uncertainties ranging from as little as 12 Å for uniform structures to as much as 50 Å for irregular islands. Typically mouse measuring uncertainty was less than 10% except for the smallest islands discernible on a scan for which errors as large as 30% might occur. The solution was to simply avoid counting islands that were not readily measured. Any islands skipped in this manner would be more accurately represented at the next smaller size scan. At the smallest scan size, anything that could be distinguished from noise could be measured. It was only by using the small scan head that good atomic resolution images could be obtained.

In the vertical direction island measurement was quite accurate, thanks to the strong exponential decay of tunneling current away from the surface. On the large 6 μm scans island height uncertainty was no worse than 0.5 Å, while on both of the lesser scans uncertainty was limited by the feedback control system to about 0.2 Ångströms.

Nucleation and Condensation

The island survey information was transformed into direct nucleation data using the approach outlined in Chapter 3. First the raw island count was reduced to the density of nucleation islands on the substrate at each location. Then a number of deposition parameters and material constants were determined. The mass impingement rate, \dot{M} , was $1.78 \times 10^{-4} \text{ g/cm}^2 \cdot \text{s}$, calculated from the bulk deposition rate of 2.0 Å/s at room temperature using the bulk density value for nickel, 8.90 g/cm^3 . This value was adjusted for the heated films by interpolating the density of nickel linearly based on its melting point density of 8.3 g/cm^3 at 1453°C .⁶⁵ The mass of material actually deposited on the substrate, M , was determined from the volume of material discovered during the island count. It differed from location to location, ranging from a high of $8 \times 10^{-7} \text{ g/cm}^2$ to a low of only $1.4 \times 10^{-9} \text{ g/cm}^2$. The spatial variation of this and other nucleation parameters will be explored in detail later. Once M had been calculated it was possible to determine the effective atomic impingement rate, R , in the nucleation zone of the films studied by assuming complete condensation, as expected for nickel. Using the largest mass deposit observed outside of coalescence regions, R was determined to be approximately $5 \times 10^{12} \text{ atoms/s}$ for all films. Finally the island periphery available for nucleation, y , was taken as the circumference of the average area of bare substrate associated with each island after removing an area with a radius of 30 nm to account for the average capture zone observed. Values of y varied greatly from a few hundred nanometers to almost $100,000 \text{ nm}$ in sparsely nucleated regions.

Other constants needed in the nucleation rate equation (3-3) were determined from material properties. The average adatom jump distance, a_0 , was simply taken as the unit cell spacing of the HOPG substrate, 2.5 Å . The adsorption site density, N_0 , was approximated as the atomic density of a monolayer of graphite, $3.8 \times 10^{15} \text{ atoms/cm}^2$. Lastly the frequency of surface vibrations was taken as 10^{13} Hz in accordance with other sources.^{26,27}

The nucleation rate at each location studied was then calculated using equation (3-16) and the results were applied to the nucleation rate equation. Before doing so though it was necessary to check the assumption that condensation was complete by exploring the reciprocal temperature dependence of the saturation nucleation density, N_∞ , for each film studied. The saturation density of nuclei for each

film was taken as the highest nucleation density observed without coalescence. This data is plotted in Figure (5.8) and has a positive slope, indicating complete condensation, as expected.

Surface Activation Energies

Using equation (3-3) under conditions of complete condensation of 2-D islands and assuming a single atom critical nucleus size for nickel, it was only possible to determine the activation energy for surface diffusion, E_d . In this condensation regime re-evaporation is so insignificant that it does not enter into the nucleation rate equation. The critical cluster binding energy was also unnecessary since it was zero for nickel. Despite the varying island populations and nucleation conditions observed on the films studied, the calculated values of E_d were quite consistent, working out to 1.97 ± 0.12 eV. This is an extremely large value, indicating strong nickel condensation. Such a large value certainly supports all of the assumptions made about nickel depositions including low inherent nucleation barrier, tight self-binding and extreme resistance to re-evaporation. Recall that the binding energy of a nickel dimer is 2.714 eV, meaning that the activation energy for re-evaporation of nickel adatoms must lie somewhere between E_d at 1.97 eV and the dimer binding energy.

From a material properties stand point though, this value of E_d seems far too high. HOPG is a layered material with a passive surface and should be a very poor source of tight-binding nucleation sites. Indeed, only significant surface diffusion could account for the prevalence of large islands along HOPG features. Previous studies of nickel nucleation on a variety of materials have revealed surface diffusion activation energies ranging between 0.6 and 0.9 eV,^{78,79,80} always considerably higher than for silver or gold.⁸¹ Values in this range are not incompatible with a reasonable amount of surface diffusion, even at room temperature. It would appear then that the observed value for E_d must include effects from factors not accounted for by the nucleation rate equation used. Lacking hard evidence as to the cause, it is only possible to present hypotheses, of which there are three.

First, sulfur contamination of nickel thin films has been observed after less than a week of exposure to air.⁸² All of the films studied were exposed for far longer than that, and much of the data presented was gathered after several months of exposure of the film surfaces to room air. It is likely then that

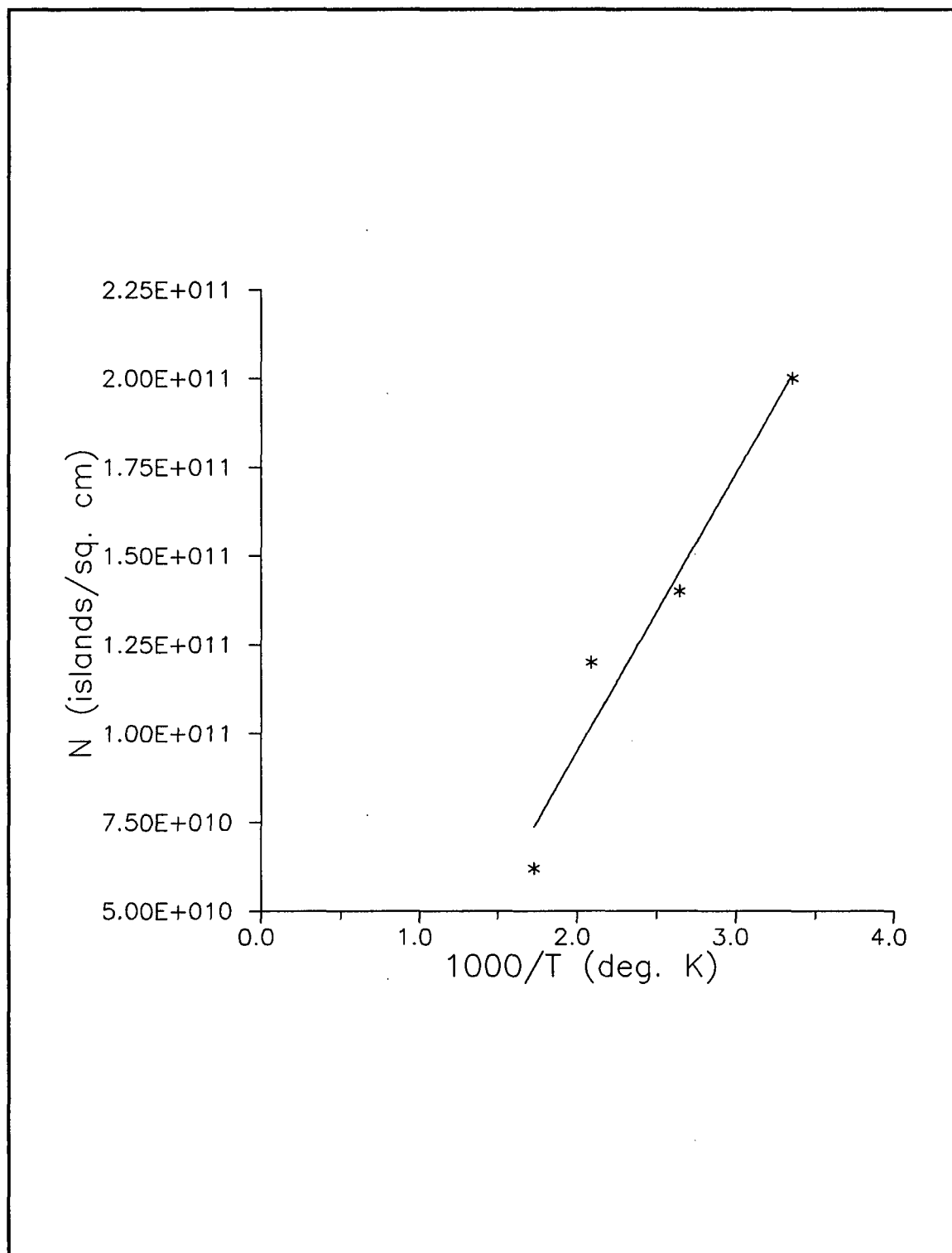


Figure 5.8 Reciprocal temperature dependence of the saturation nucleation density for nickel films on HOPG.

the films were at least partially covered by chemisorbed sulfur when they were scanned and this could have modified the observed island demography.

Second, electron microscope studies of metal films deposited with unity sticking coefficients have shown that a significant fraction of the metal material does not reside on the surface, but rather diffuses into the substrate.⁸² Since the mass of nickel deposited on the films studied here was determined solely by STM observation of the film surface, the mass deposited may well have been underestimated. However, underestimating mass deposited should have lead to an underestimated nucleation rate (see equation 3-16), and a resultant underestimation of the energy of activation for surface diffusion.

Finally, it is quite possible that the equation chosen to model nucleation was inappropriate and should have included an additional surface energy term to account for factors such as adatom trapping at minute surface defects. This extra energy term would then account for a portion of the otherwise overvalued surface diffusion activation energy. Overestimation of nickel surface diffusion coefficients due to the omission of unusual effects has been noted before, making accurate modeling of nickel nucleation difficult.⁶⁰

Spatial Nucleation Variations

Variations in the surface quality of HOPG from one local area to another also make it somewhat difficult to quantify the spatial variations of nucleation parameters on a single film. However, by comparing data from three films deposited at different temperatures, some common factors appear. The most striking observation is that the nucleation rate is often low near the edge of the continuous film region of the shadowed films studied. It then rises to a maximum several hundred microns out into the nucleation zone and then drops off. This same general behavior is observed in other nucleation parameters including the saturation nucleation density and the amount of mass deposited. Nucleation rate data for the three films studied is given in Figure (5.9) below showing the tendency for the rate to peak away from the continuous film edge. It appears as though the continuous film, which forms rather late in the deposition, has a significant influence on neighboring island growth areas, tending to gradually depleting them of material. In effect the continuous film edge has a large capture zone

extending out over adjacent island growth regions. However, since the final location of the continuous film edge forms only as deposition ceases, its capture zone effect is not complete. Also note that in all of the films deposited the film structure transitions from continuous deposit to pure island structure very rapidly. Little or no channel structure is observed, a fact shown in Figure (5.10) where the extreme edge of a continuous film growth is imaged.

Coalescence Stage

Because of the maturity of the nucleation regions of the films studied, areas where coalescence had begun were relatively easy to find. Often the catalyst was a nearby defect in the graphite substrate which provided tight binding sites for nickel atoms to adhere to. However, the style of complete island coalescence commonly observed during the formation of thin films²⁷ was less pervasive on the nickel films studied due to the extremely high effective activation energy for surface diffusion. More commonly, small islands appeared to combine more slowly by bridging gaps with a thin layer of material in manner similar to channel filling. This slow liquid coalescence is likely aided by the addition of atoms from the vapor flux.

Substrate Effects

The strong influence of graphite defects on the formation of the nickel films has been amply demonstrated in Figures (5.1) and (5.2) above, but an even more striking view is shown below in Figure (5.11). A small STM scan is shown where large islands have formed along a graphite defect nearly a full millimeter from the edge of the continuous film. The surrounding graphite is almost devoid of film clusters even far from the defect. Careful inspection shows several areas where slow liquid coalescence is occurring between these tightly bound nickel islands.

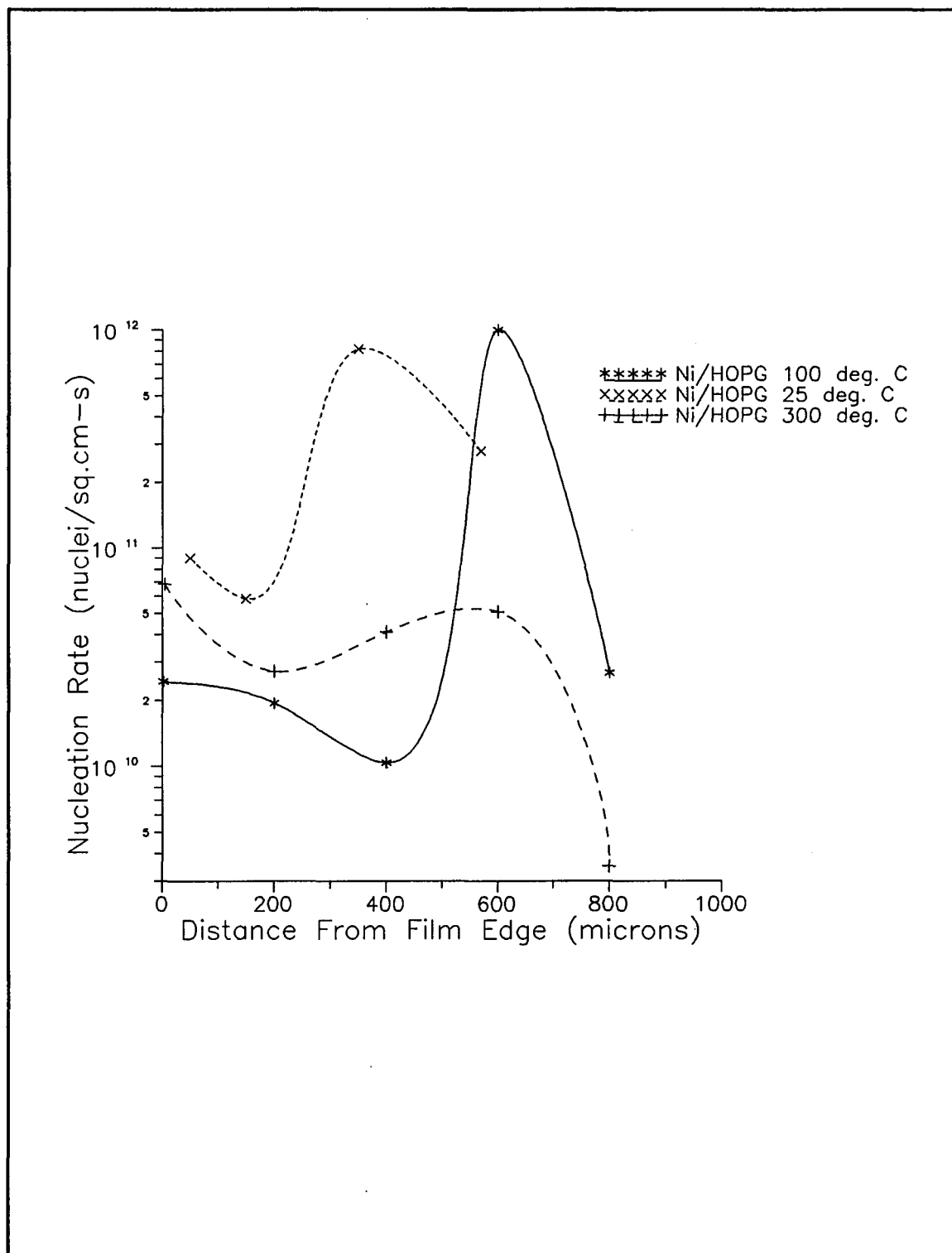


Figure 5.9 Spatial variation of the nucleation rate as a function of distance from the continuous film edge.

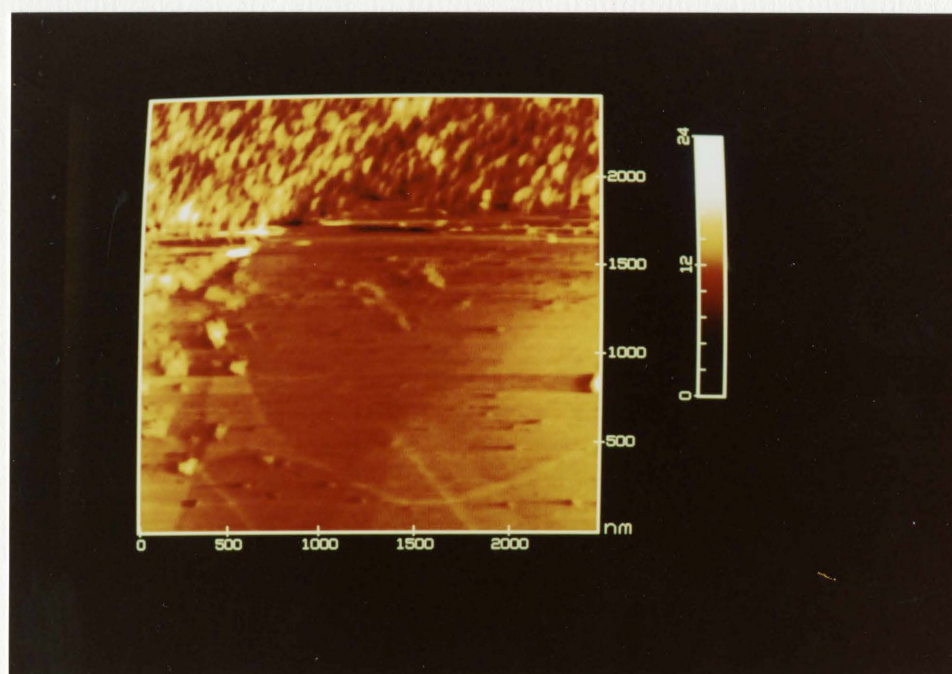


Figure 5.10 STM scan of the extreme edge of a continuous film growth.

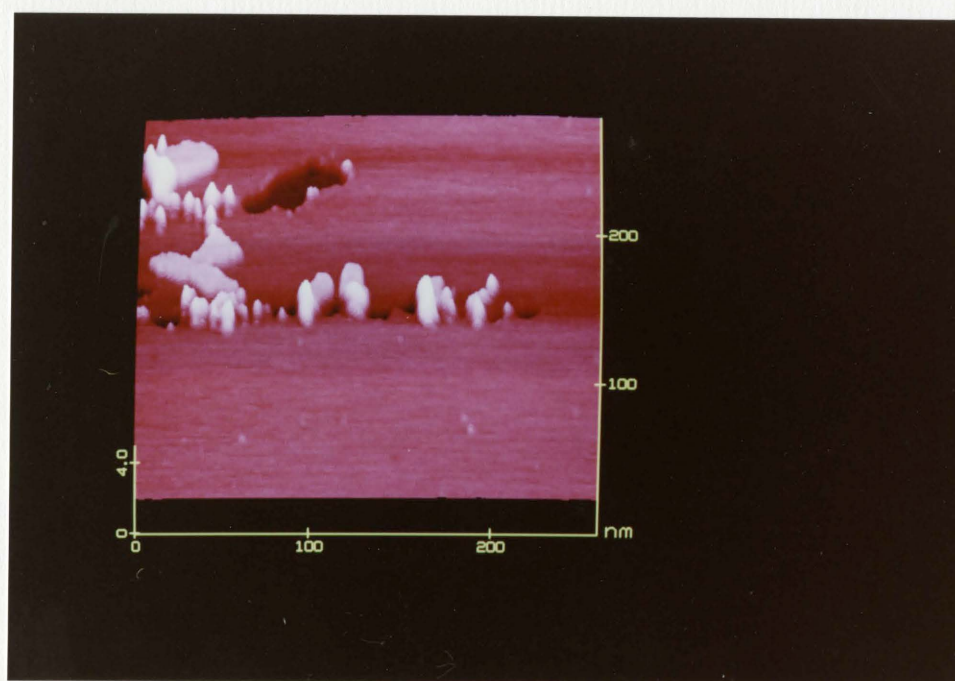


Figure 5.11 Small STM scan one millimeter from the continuous film edge showing island growth only along a graphite defect.

Island Formation and Structure

Because the high effective activation energy for surface diffusion on these films likely does not accurately represent the actual amount of surface diffusion present, it is not surprising that large island growth appears to proceed mainly from the collection of adatoms from the substrate. Most island growth seen was quite two-dimensional with typical film clusters having twenty times more lateral extent than height. Exceptions occur over large HOPG defects, but the majority of post-coalescence islands are similar in most ways to the one shown in Figure (5.12). It has a base growth three atoms thick with well defined, crystallographic corners and sharp edges. The edges show a typical tendency to grow first, but oddly the central plateau is populated by secondary islands. This might indicate Stranski-Krastanov growth on the island, where energy conditions are quite different from the HOPG substrate. A perfect upper terrace on a nickel island would present a large barrier to additional nucleation. This might force the critical nucleus size higher and could cause a transition to Stranski-Krastanov growth when combined with the zero lattice mismatch resulting from homogeneous growth. A few other examples of Stranski-Krastanov growth were observed, but they were too rare to quantify properly. A false-illumination top view of this island is shown in Figure (5.13) which provides a better view of the secondary island structure.

Island Distribution

Large islands tended to be distributed in clumps and along graphite defects rather than in the more random fashion of the small nucleation islands. Powerful preferential nucleation at these defect sites undoubtedly drives this distribution of islands since it would be difficult to assemble a large island away from a source of enhanced nucleation. The gradual coalescence evidenced on HOPG terraces also makes it unlikely that a large island could form in isolation. A good example of this cluster growth is given by Figure (5.14) where large islands, shown in white, appear almost exclusively in groups along graphite defects.

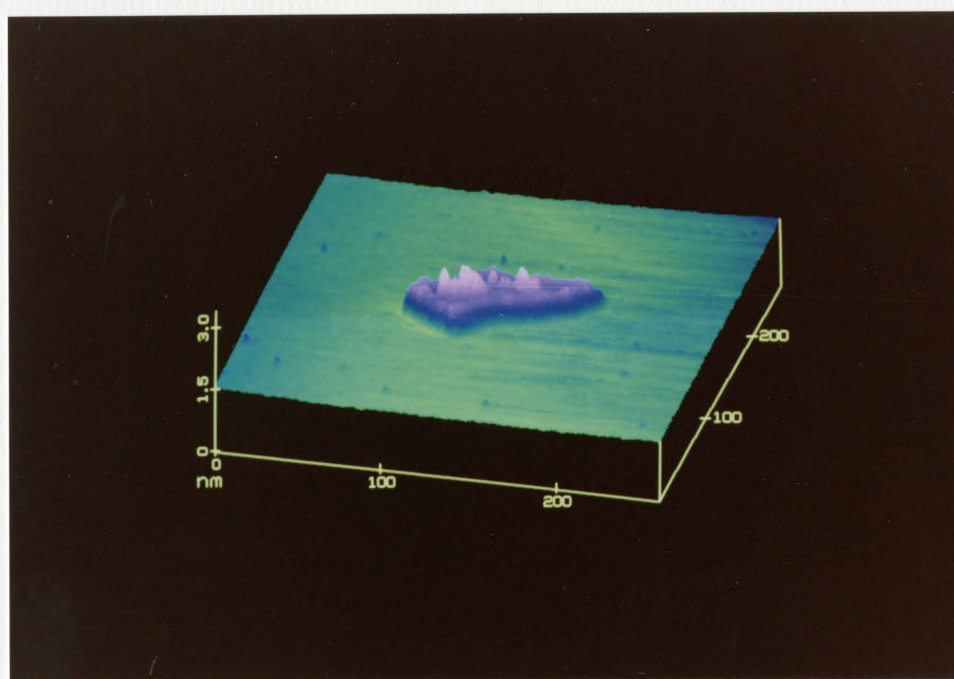


Figure 5.12 Typical coalescence stage nickel island shown in 3-D relief.

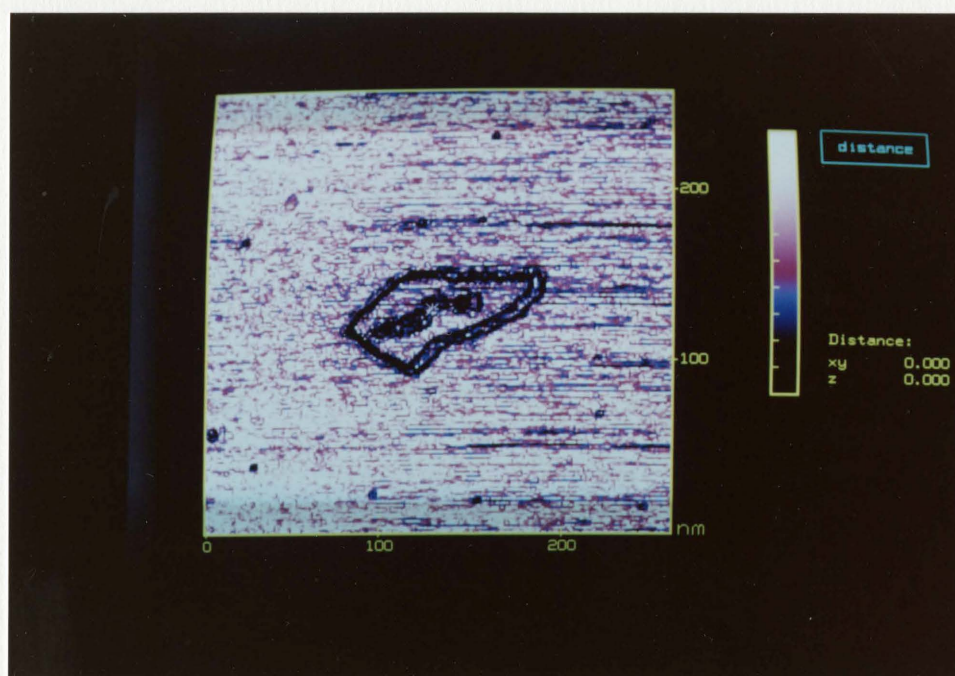


Figure 5.13 False illumination top view of the nickel island shown in Figure (5.12).

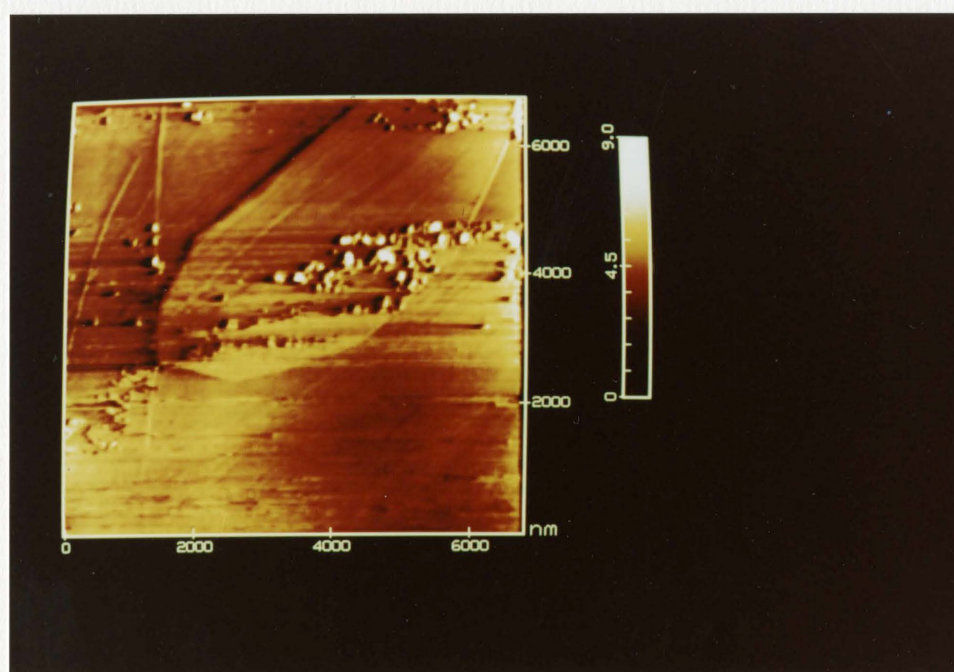


Figure 5.14 Large STM scan showing island growth in clusters and along graphite features.

Continuous Films

Whereas the nucleation regions of the various films studied were quite similar despite the differences in substrate temperature at which they were deposited, the continuous film structures differed greatly. Low temperature films were extremely fine grained while high temperature films had grain sizes about five times larger. Films deposited on fused silica substrates differed from the films made on HOPG as well. To expand the scope of the study, the effects of angle of deposition were also studied for films deposited on HOPG.

Microstructure and Surface Roughness

Using the structure zone scheme as a basis, all of the films were divided by their microstructure. Because of the number of microscopic features typical of graphite substrates, the films made on HOPG were expected to retain low temperature microstructures throughout the available temperature range from room temperature to 300°C. Films on fused silica were expected to more closely follow the zone scheme.

In reality the incredibly fine grain size of most of the films, often only 30 nm, made visual determination of zone classification difficult, even with the STM. Room temperature films did show the domed crystallites common to Zone 1 materials, but the transition to Zone 2 was difficult to discern. In addition, the films on slightly heated HOPG often had greatly elongated, fibrous grains very similar to those reported in Zone T for sputtered films. All low temperature grains were quite diffuse and the surface of the films were porous. At the upper end of the temperature range, nickel films on fused silica did show some Zone 2 columnar structure but no Zone 3 structure was visible, even at 500°C. Because the films were not left at elevated temperatures following deposition there was probably just not sufficient time for Zone 3 structure to evolve all the way to the surface of these films. Surface roughness calculations done on the STM scans were easier to interpret. Some zone boundary behavior was noted in the films on HOPG, but not in the films on fused silica, counter to expectations.

Examples of surface microstructure for various films are shown below. All of the films were nominally 500 Å thick and were deposited at 2.0 Å/s. Alpha Step measurements of the fused silica films indicated an average actual thickness of 543 ± 39 Å, in good agreement with the average crystal monitor reading of 507 Ångstroms. Nickel films were deposited on HOPG at both 10° and 30° angles of incidence and at substrate temperatures ranging from room temperature to 300°C. Additional films were also deposited at angles up to 80°. All fused silica films were deposited at a 30° angle of incidence, but the temperature range was extended upward to 500°C. Each film example given is presented in both top view and three-dimensional perspective in successive figures.

First compare the grain structure of a room temperature nickel film grown on HOPG at 30° shown in Figures (5.15) and (5.16) to a similar film grown at 300°C shown in Figures (5.17) and (5.18). The low temperature film is shown at five times the scale of the high temperature film to emphasize the ratio between grain sizes. Grains in the low temperature film are only about 20 nm in diameter, but they are quite smooth. The high temperature grains on the other hand are rougher and have diameters of about 85 nm. This heated film displays the beginnings of columnar Zone 2 structure, but it is too thin to display fully angled grains.

For the purposes of this discussion it is important to point out that since atomic orientation is not being imaged, it is possible that what looks like a single grain on a STM scan might actually consist of two or more smaller grains. Such a difference would be accounted for by X-ray analysis because the specific atomic orientation of each grain broadens the X-ray peak and contributes to the grain size determination. X-ray data actually averages grain size in three-dimensions whereas STM can only measure surface grain sizes. Thus the grain size data gathered with the STM should be considered an upper limit to the lateral size of film grains. It might be larger or smaller than the grain size determined from X-ray data depending on whether the film grains were flattened or extended perpendicular to the film surface. In general though STM and X-ray grain size data are quite comparable.⁸³

Next compare the surface textures of a room temperature fused silica film, Figures (5.19) and (5.20), to one of the auxiliary films sputtered on silicon shown in Figures (5.21) and (5.22). Both films are at least as smooth as the room temperature film on HOPG but they have a tighter grain structure,

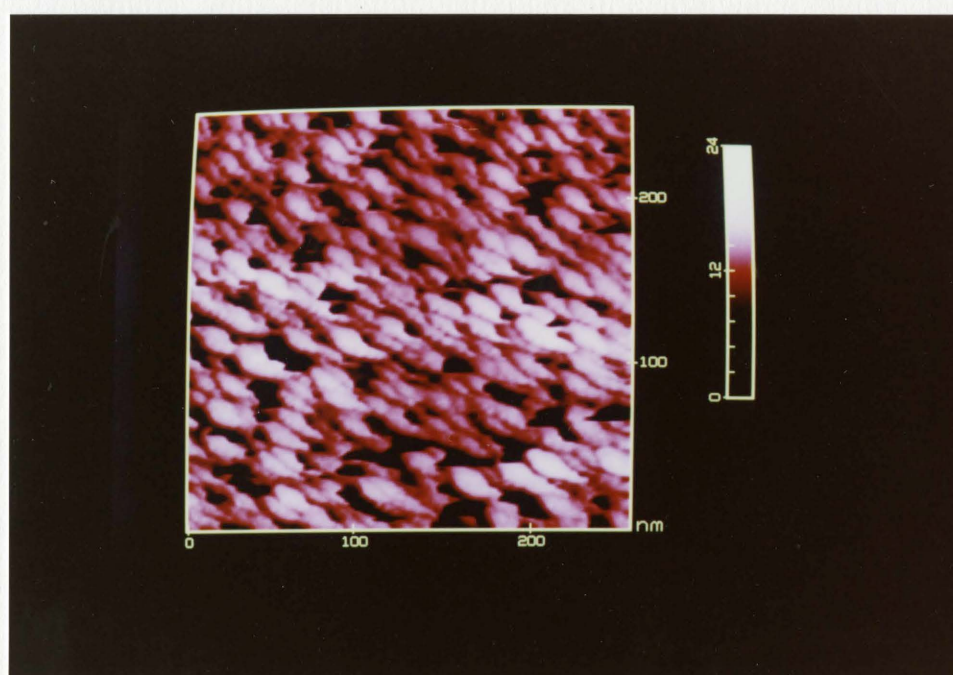


Figure 5.15 Top view of nickel film grown on HOPG at room temperature and a 30° angle of incidence.

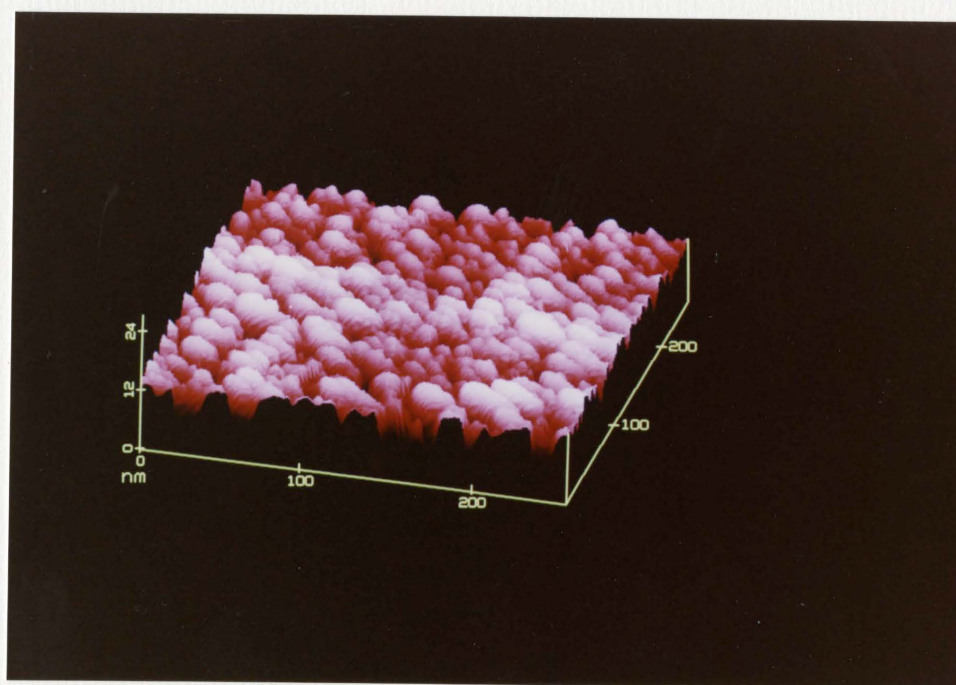


Figure 5.16 Three-dimensional view of a room temperature nickel film deposited at a 30° angle.

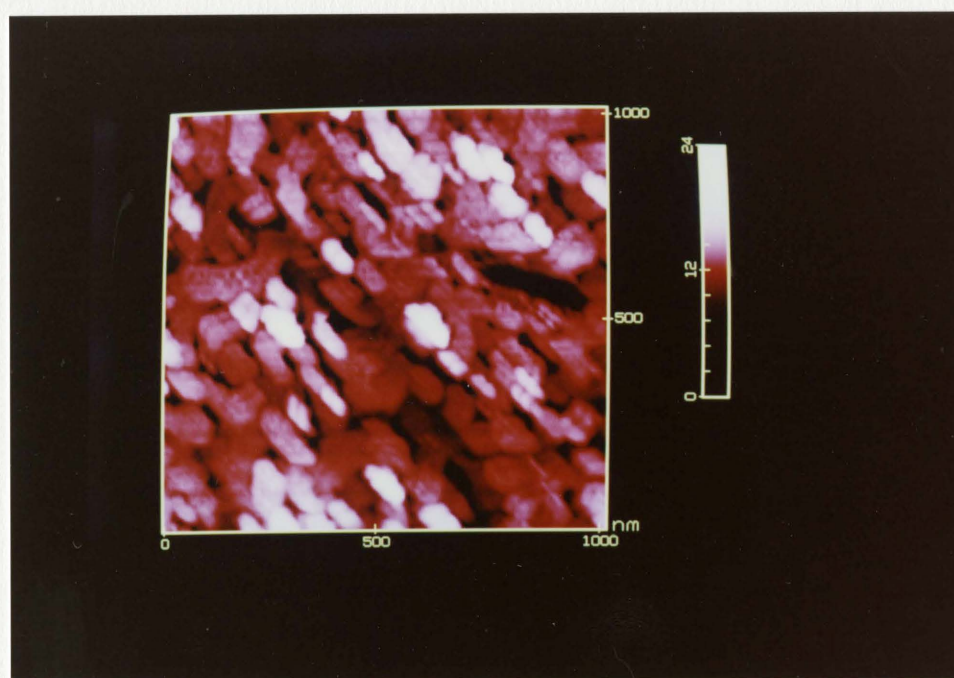


Figure 5.17 Top view of the surface of a nickel film deposited on HOPG at 300°C and an angle of 30°.

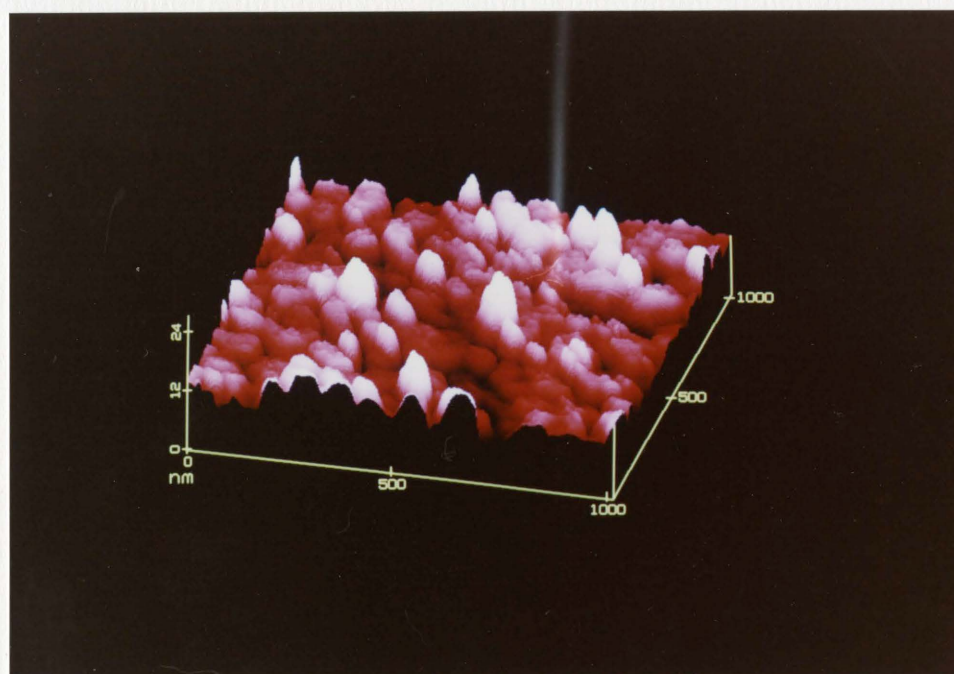


Figure 5.18 Three-dimensional view of a nickel film deposited on HOPG at 300°C and an angle of 30°.

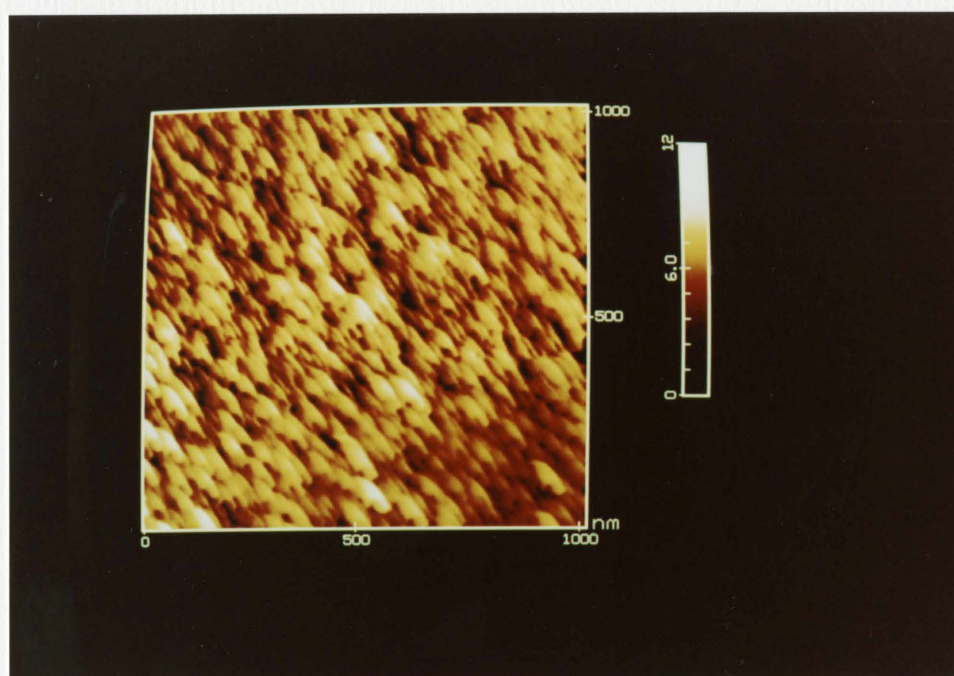


Figure 5.19 Top view of a room temperature film on fused silica.

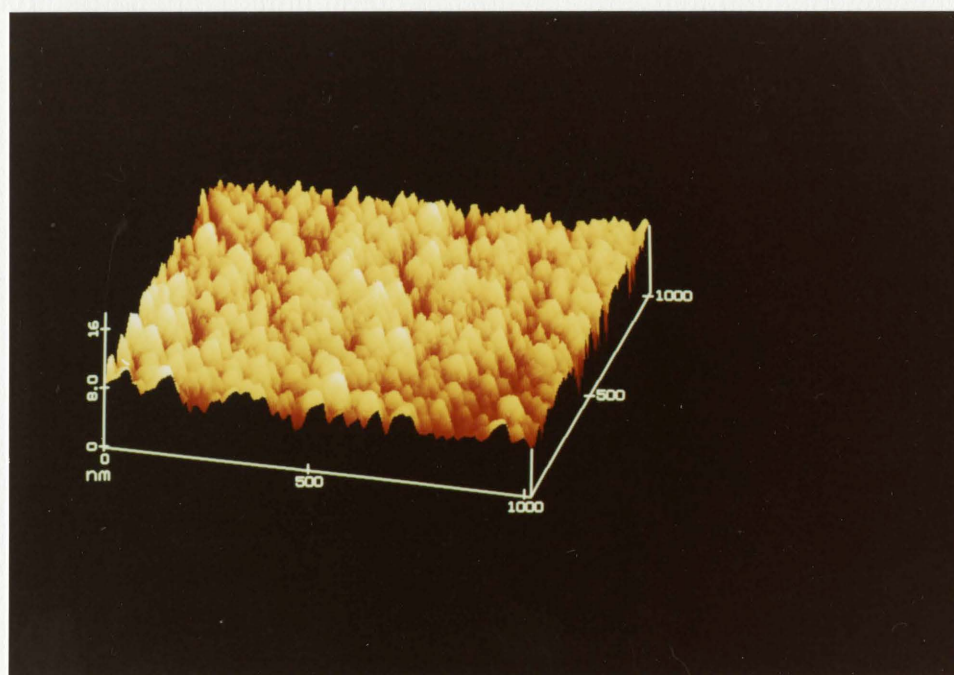


Figure 5.20 Three-dimensional view of the surface texture of a room temperature nickel film deposited on fused silica.

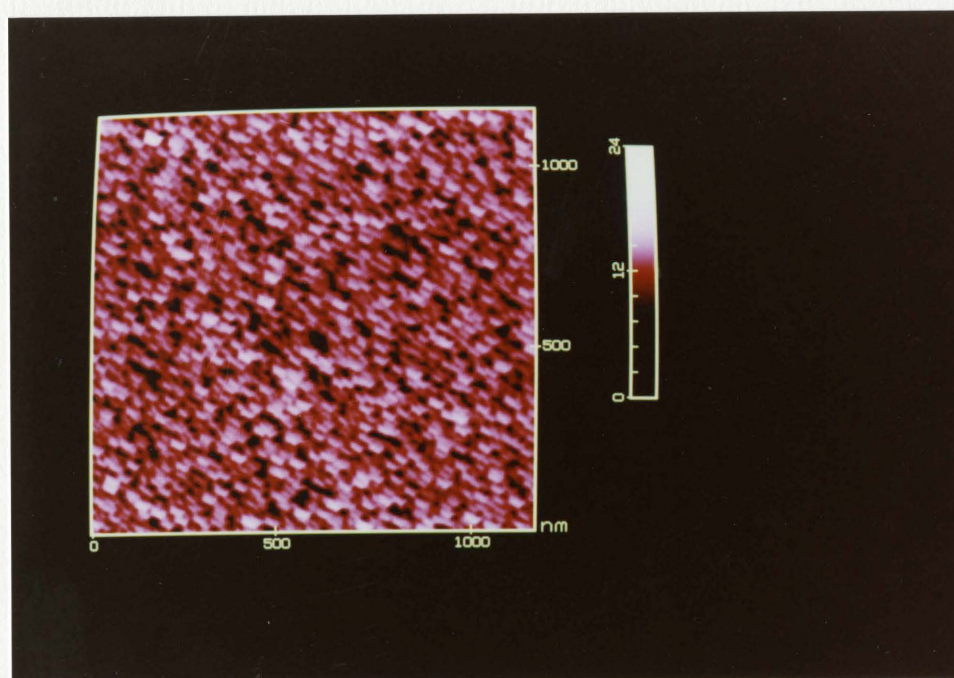


Figure 5.21 A top view of a sputtered nickel film deposited on silicon at just above room temperature.

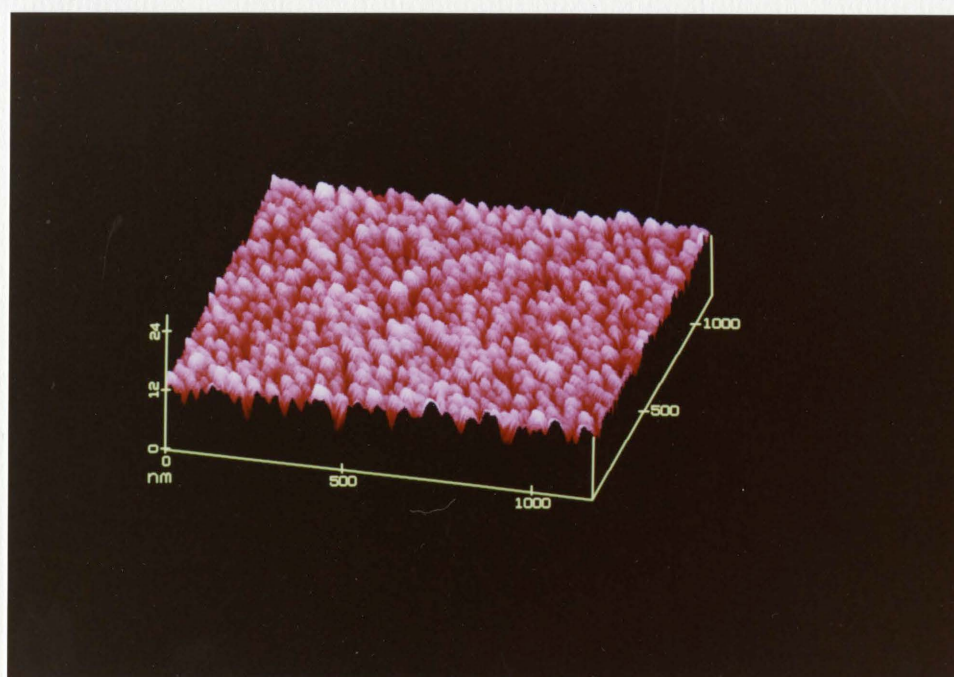


Figure 5.22 A three-dimensional view of the surface of a sputtered nickel film deposited on silicon at just above room temperature.

especially the sputtered film. At 30 nm, the grains of the sputtered film are not as small as those of the film on graphite, but they have smoother surfaces. The fused silica film has elongated grains with an average dimension of nearly 60 nm. Note that the vertical scale of the fused silica film is 50% smaller so that it is actually the smoothest of the films compared. The elongated, ill-defined structure of the fused silica grains resembles the Zone T structure observed on nickel films on HOPG at around 100°C.

The most coherent way to review the surface roughness variations of these films with angle and temperature is to simply plot out the data. The bulk of this data was gathered by calculating the RMS roughness of numbers of individual STM scans, but the Wyko was also used on the fused silica films. This data is shown in Figure (5.23) as a function of temperature for three series of films, nickel on HOPG deposited at both 10° and 30°, and fused silica deposited at 30° examined with the STM and with the Wyko optical profilometer. Error bars were excluded from this graph because of the density of material presented. The RMS data for just the HOPG films is also shown in Figure (5.24), with error bars included. The corresponding data, with error bars, for the films on fused silica is in Figure (5.25). The effect that increasing the angle of deposition had on nickel films deposited on HOPG at room temperature is shown in Figure (5.26).

The temperature dependence of the surface roughness of the HOPG films belies the underlying zone structure. At room temperature they are quite rough, but as deposition temperature is increased the roughness decreases until the vicinity of the Zone 2 boundary is reached between 200° and 300°C. The change in microstructure across the zone boundary causes a marked increase in film roughness. Within uncertainty, the films deposited at 30° were not observed to be any rougher than the films deposited at a 10° tilt.

The roughness of films on fused silica was quite interesting as well. Roughness rose gradually with temperature up to about 350°C, and then increased rapidly. This behavior is not consistent with a zone boundary explanation like that applied to nickel on HOPG, but it is in remarkable agreement with the increase in nickel grain size with temperature given by Fleet (and presented by Hoffman) for nickel films 500 Å thick.⁸⁴ More details on this will be presented below. It would appear then that grain size is the primary contributor to roughness on the scale measured by the STM. Normal metal film grains

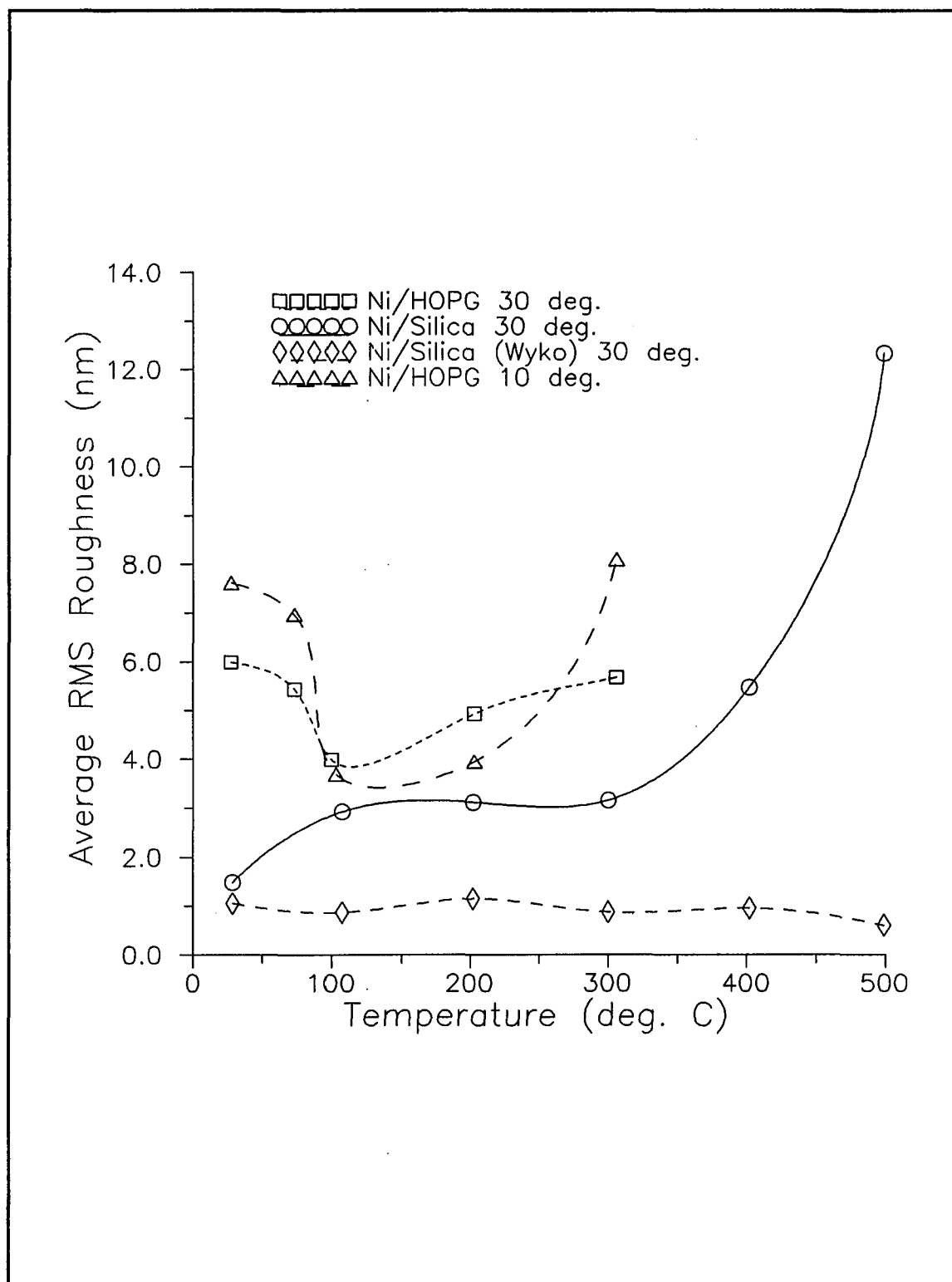


Figure 5.23 The temperature dependence of surface roughness for several nickel film series.

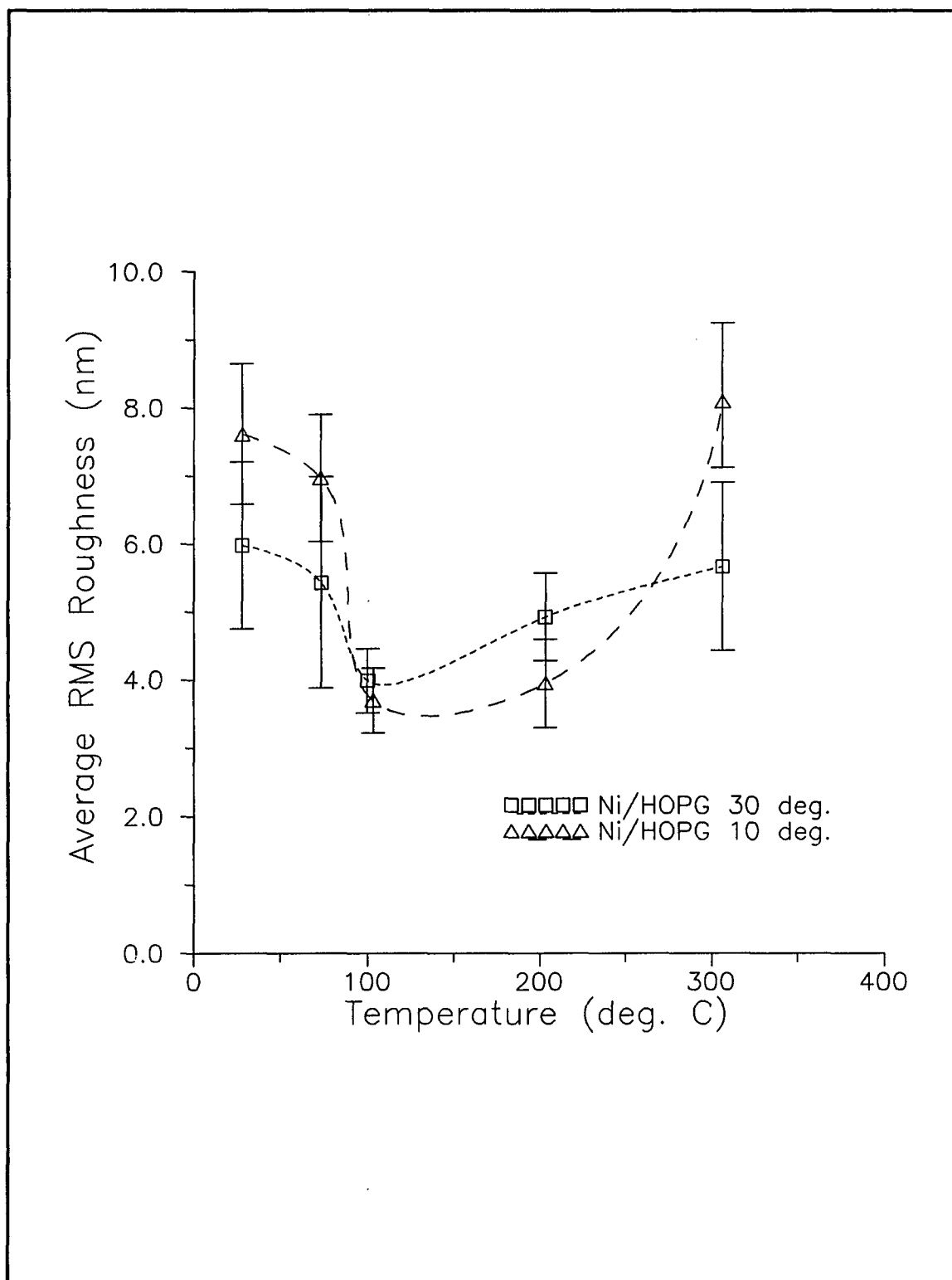


Figure 5.24 Temperature dependence of the microRMS of nickel films on HOPG showing uncertainty.

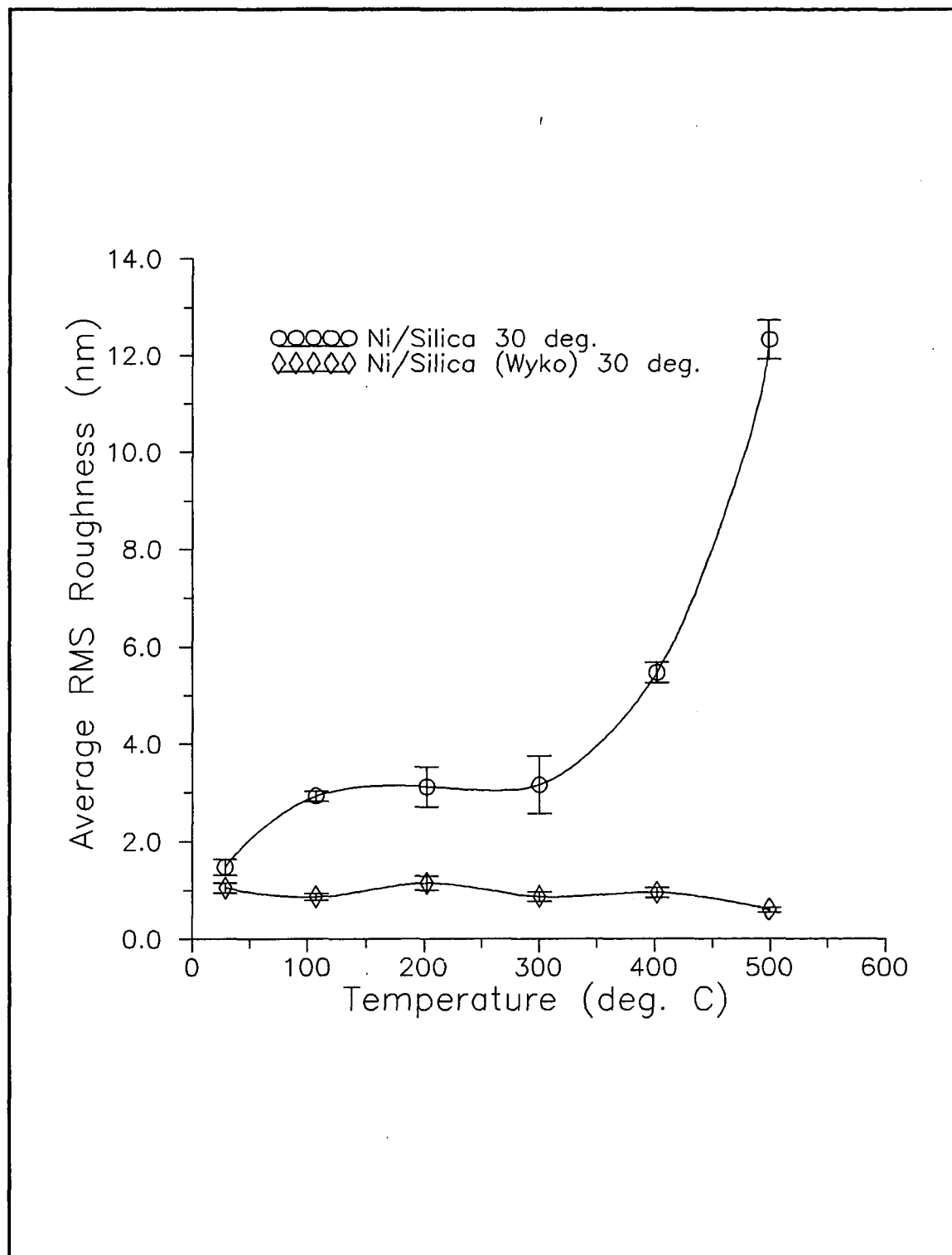


Figure 5.25 Temperature dependence of the roughness of nickel films on fused silica as measured with the Wyko and the STM, showing uncertainty.

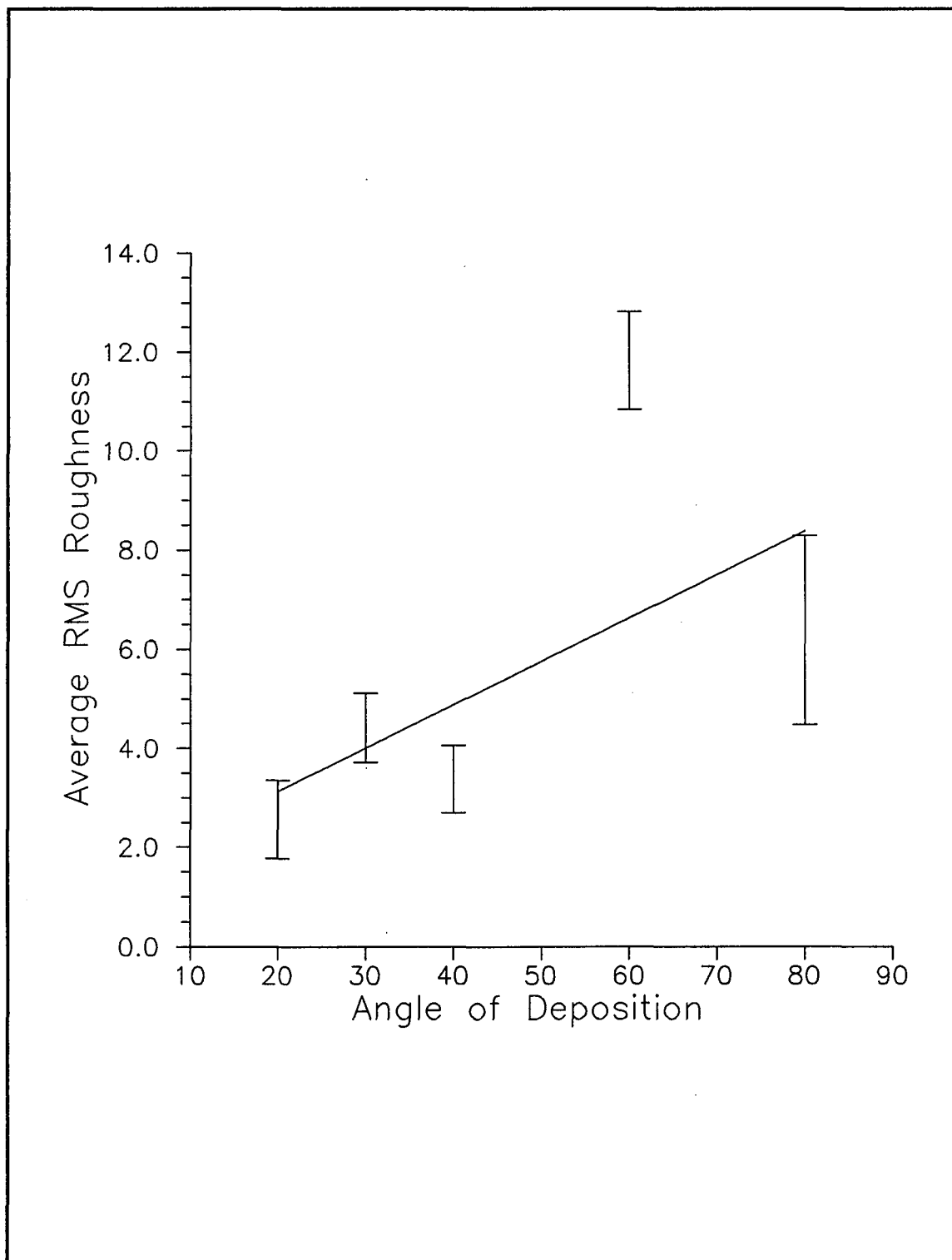


Figure 5.26 Observed angle of deposition dependence of surface roughness for nickel films deposited on HOPG.

are far smaller than the resolution of conventional roughness measurement instruments, including the Wyko. Highly surface sensitive RMS values such as those generated from STM data, often referred to as microRMS, are much more sensitive to actual surface texture than conventional RMS determinations which average their results over fairly wide areas. The Wyko for example generally averages surface roughness over a one micron area. This may be small when compared to optical micrograph resolution, but it is huge on a STM scale. Notice that the Wyko RMS scans of the nickel films on fused silica returned extremely low roughness values. Moreover, the RMS values fell slowly with temperature in direct opposition to the STM scans of the same films. This discrepancy can be explained by the different roughness regimes measured by the Wyko and the STM. As grain size increases with substrate temperature, the grains themselves become rougher and this increases microRMS. On a larger scale however film discontinuities at larger substrate features decrease with temperature, tending to reduce the conventional RMS.

The dependence of film roughness on the angle of deposition was not so well behaved on the films tested. Roughness did increase with angle up to 60° , but then appeared to drop off again on the 80° film. It is possible however that the 80° film was so severely tilted during deposition that it did not grow to anywhere near full thickness, which would tend to reduce the roughness observed somewhat. Thus a line is fit to the data in Figure (5.26) to avoid reading too much into the data. An example of the disturbance of film microstructure that results from high angles of deposition is shown in Figure (5.27). The base nickel film growth is disrupted by large numbers of large hilly growths which add very significantly to film roughness.

All of this analysis identifies film grain size as the most important factor in determining the microRMS value of a film. In some cases the correlation is poor, but on the whole the increase in film grain size with temperature is the driving force behind the increased microRMS of films deposited at high substrate temperatures. This can be seen more clearly by examining Figure (5.28) where film grain size is plotted as a function of temperature for films deposited on HOPG at 10° and 30° tilts and for films deposited on fused silica at a 30° angle. For reference, the data reported by Fleet (as presented by Hoffman)⁸⁴ in 1963 for 500 Å thick nickel films is also shown. Comparing these results with the increases in film microRMS with temperature shown in Figure (5.23) provides clear proof of

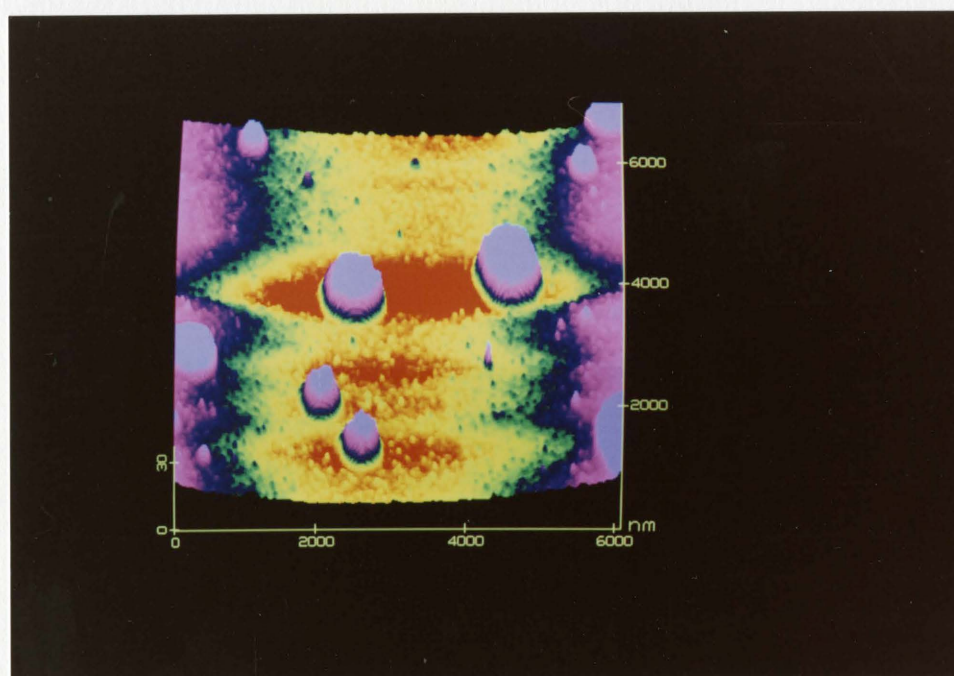


Figure 5.27 Disturbance of normal film microstructure by deposition at high angles of incidence.

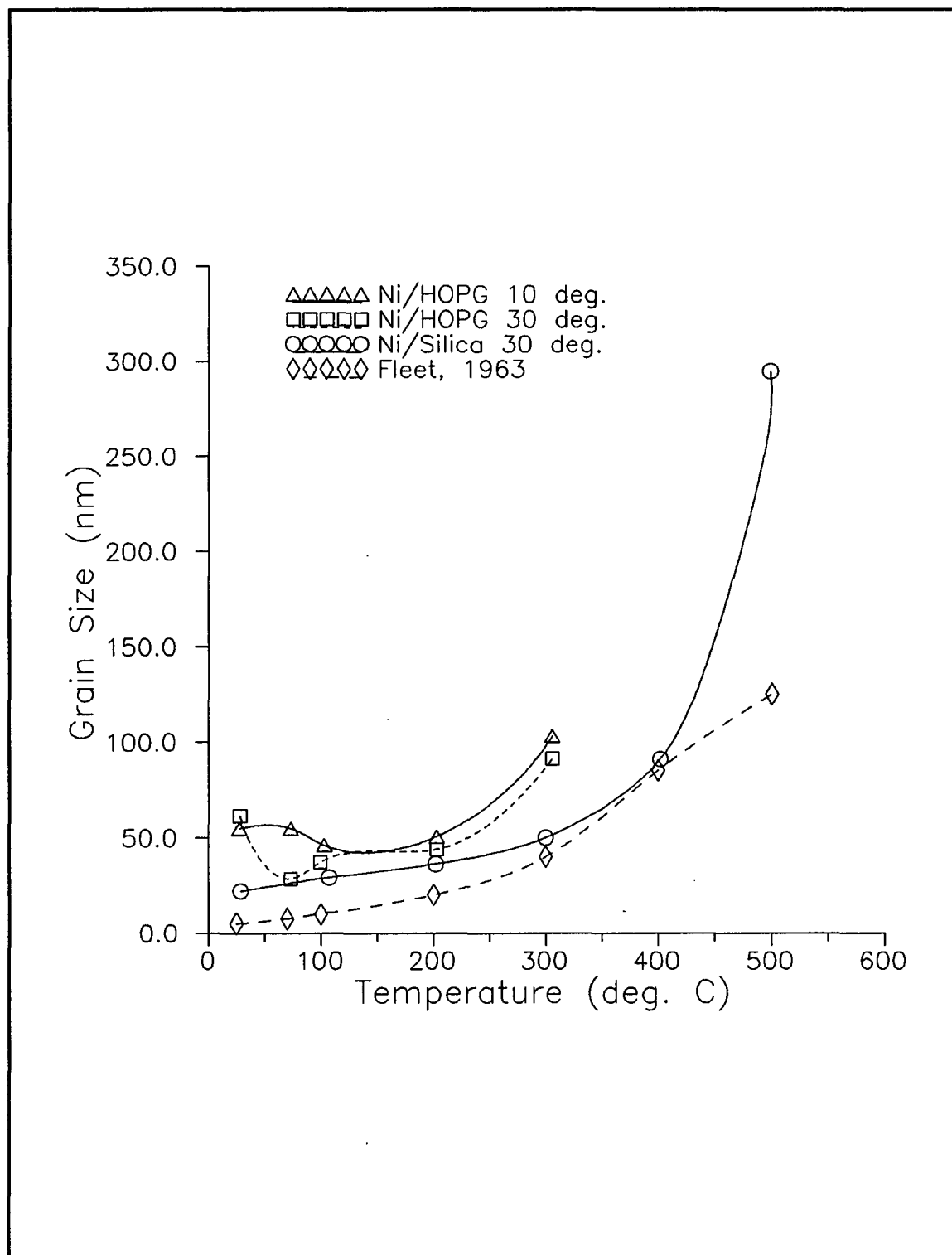


Figure 5.28 The increase in film grain size as a function of increasing temperature for several film families.

the link between the two phenomenon. The grain size of the films on fused silica are in good agreement with the data from Fleet (as presented by Hoffman)⁸⁴ except for the 500°C film, which is somewhat rougher than expected. The films on graphite are larger grained across the board. This is to be expected as a result of the roughness of the graphite though. Low temperature zone structures tend to linger on the films deposited on HOPG because of preferential nucleation near surface defects on the graphite which in turn leads to the formation of larger grains than normal at a given temperature. Because Figure (5.28) is quite dense, error bars were excluded from the data. Error bars are included with the data in Figure (5.29), showing only the grain size data for films on HOPG, and Figure (5.30), showing the grain size data just for films on fused silica.

Film Defects

The vast majority of the continuous film regions studied did not show any large scale defects whatsoever. However one of the oldest of the films studied did show some signs of breaking up towards the end of this research. One example is a circular film defect which resembles a large dislocation loop such as those sometimes imaged as dark dots in SEM micrographs. This feature is shown in Figure (5.31). Defects of this type were actually quite prevalent on the film in question and made it nearly impossible to scan the film. The picture in Figure (5.31) was only obtained by locating a relatively isolated defect. Another early film deposited at high temperature began to show signs of stress when lab humidity rose during the summer. A picture of a tear induced by stress on this film is shown in Figure (5.32).

Newer films did not show any structural defects such as these. However, some of the higher temperature films did have holes near the edge of the continuous film region. A striking example is shown in Figure (5.33) of a hole about 5 μm from the edge of a room temperature film deposited on HOPG at a 20° angle of incidence.

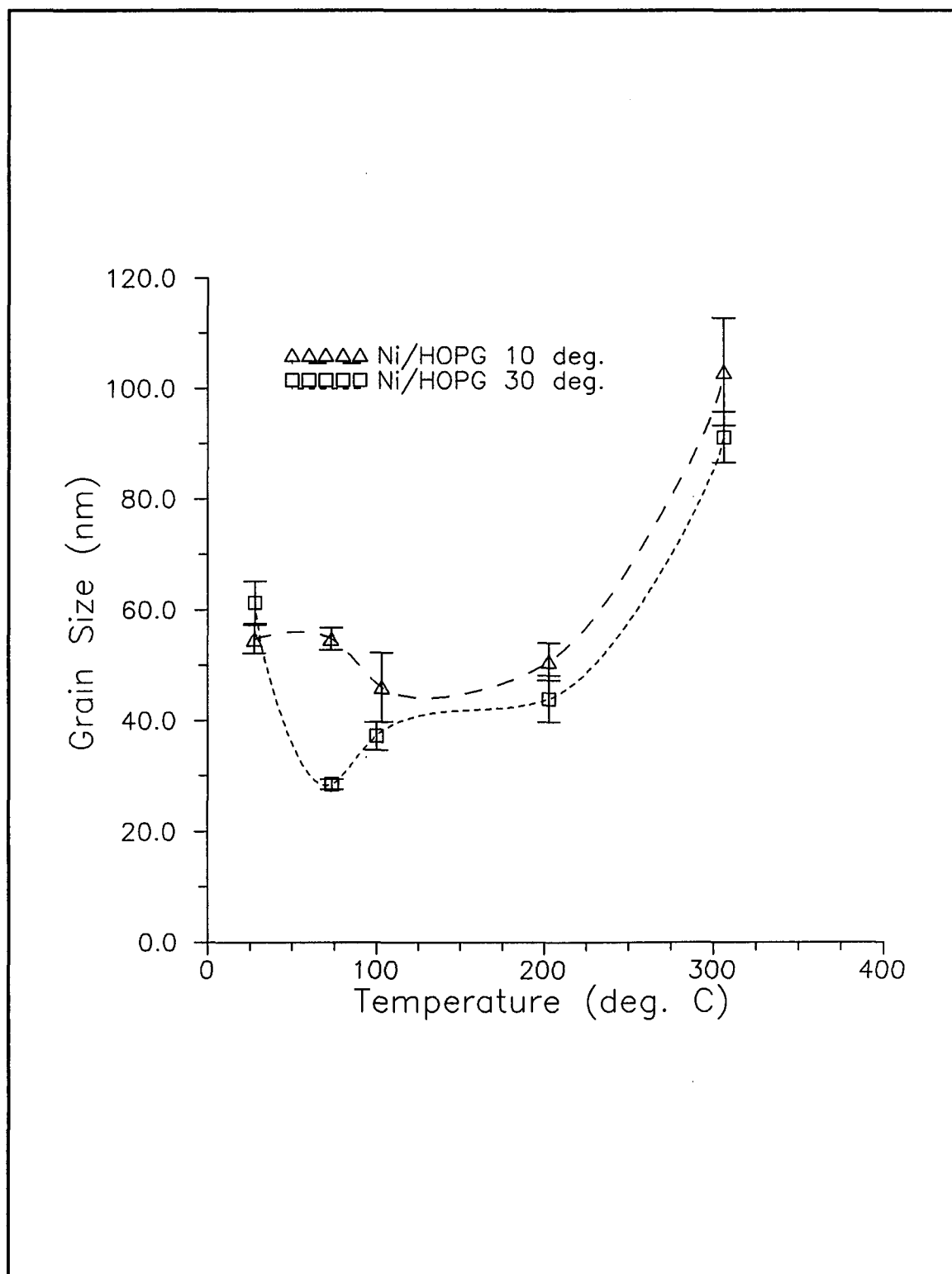


Figure 5.29 Temperature dependence of grain size for nickel films on HOPG, showing uncertainty.

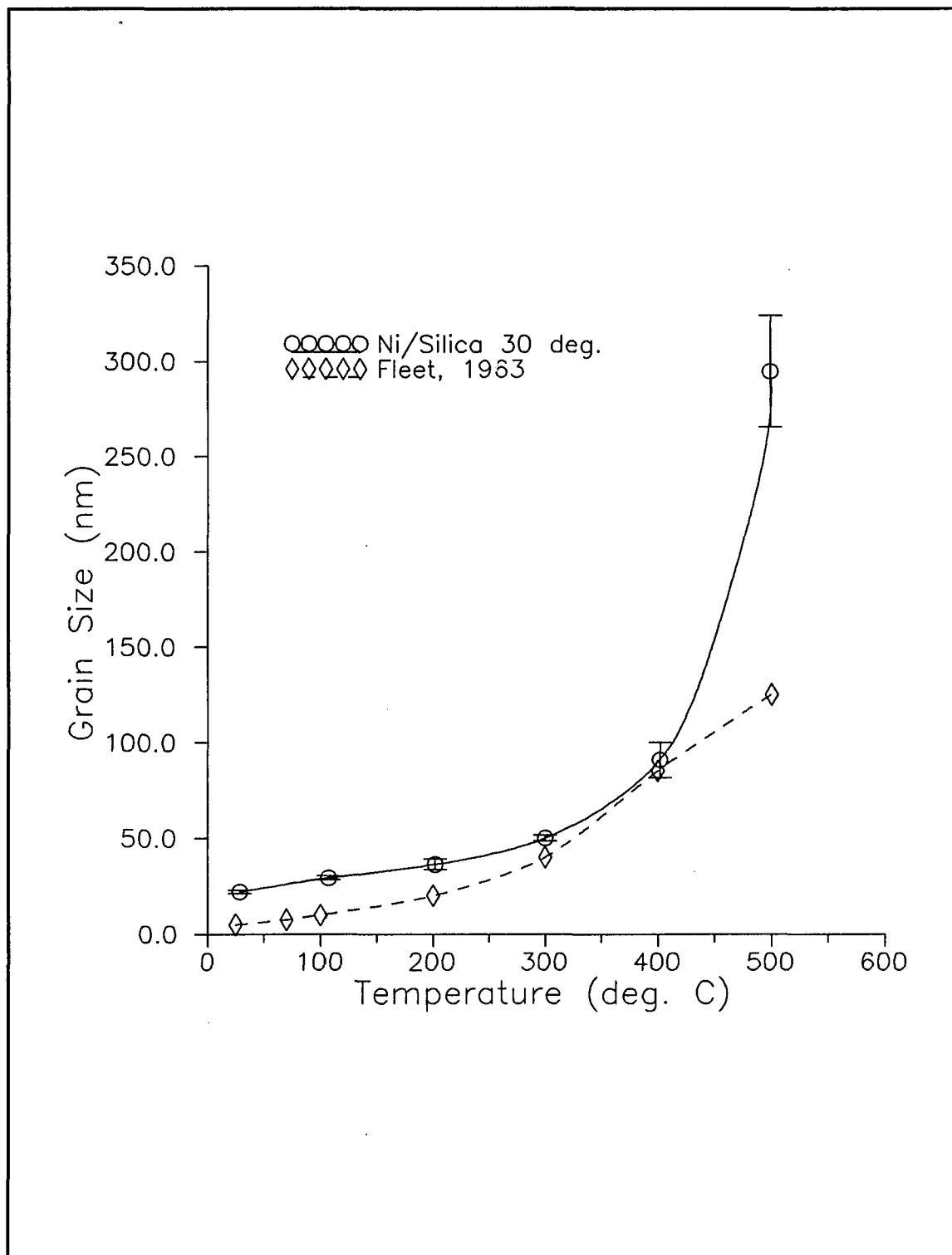


Figure 5.30 Temperature dependence of grain size for nickel films on fused silica, with uncertainty indicated and data from Fleet shown for comparison.

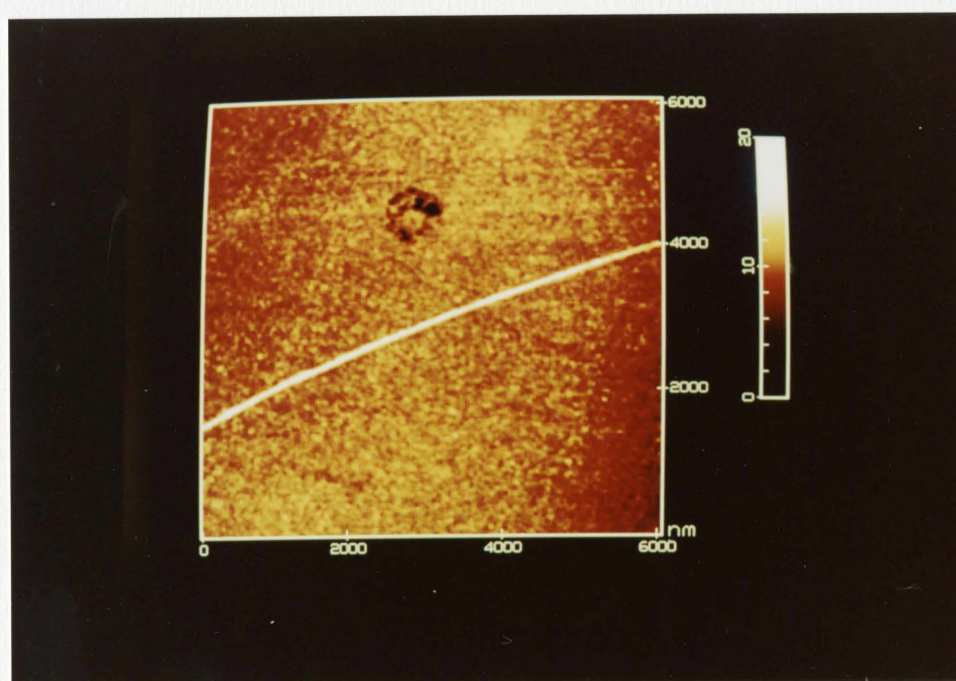


Figure 5.31 A large dislocation loop defect on an old nickel film.

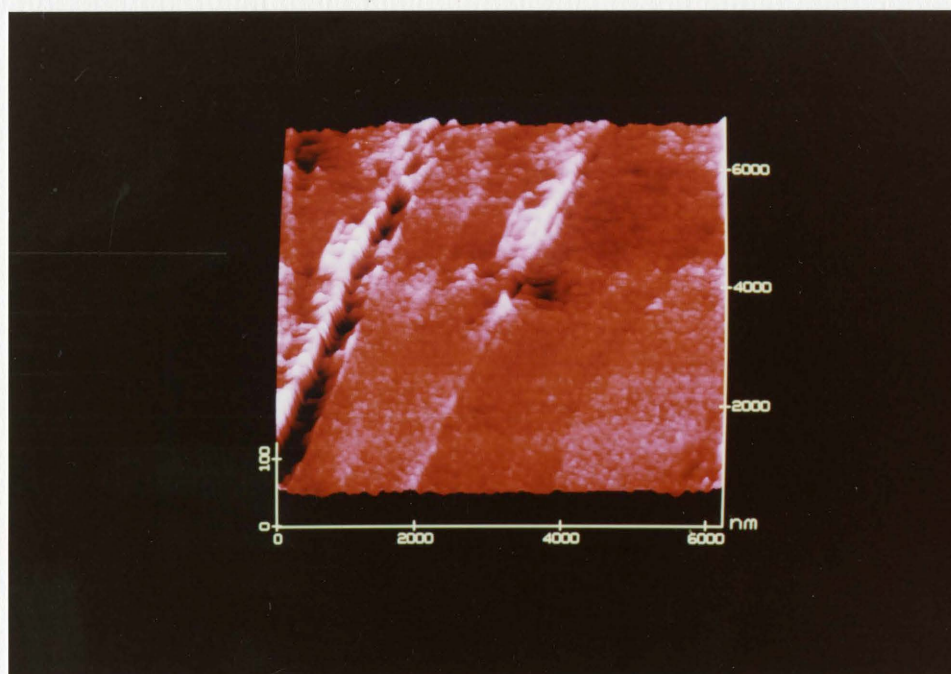


Figure 5.32 A stress induced tear in a nickel film.

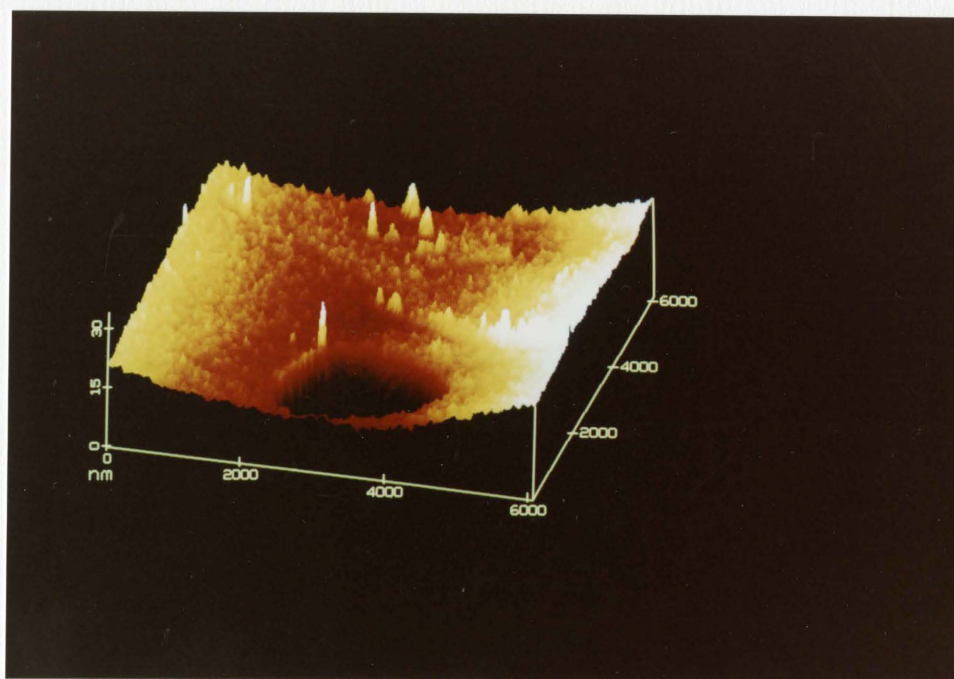


Figure 5.33 A large hole in a room temperature nickel film some $5\text{ }\mu\text{m}$ from the edge of the continuous film.

Surface Spectroscopy

Little actual research was carried out with STM spectroscopy, but it was essential in clarifying the structures being observed. In general nickel film regions had very complex spectra because of the presence of large numbers of grain boundaries. Each boundary is slightly different electrically and chemically from the adjacent grains and this difference shows up in both STS and work function profile modes as large numbers of spikes in the spectra. Nickel islands could also be differentiated from the HOPG substrate using STS since their conductivity was higher than the surrounding graphite. While this was not done for the actual island counts, it was done beforehand to build up experience in correctly identifying islands. Graphite itself has exceptionally dull spectra on a STM scale. Even large graphite surface defects can fail to show up on spectra unless they have very sharp edges or very high spatial resolution is being used.

The availability of spectroscopic plot modes was also important because it allowed the I-V characteristics of the nickel film to be studied and compared to reports issued by researchers working with nickel in vacuum.²¹ These reports indicated that nickel which was intentionally oxidized had a set of spikes in the I-V curve equal in number to the layers of oxide present. If the oxide became thicker than six layers the spikes washed out and tunneling became virtually impossible. Similar studies of the nickel films used in this research did not reveal any oxide layers. As mentioned earlier, all the nickel films studied could be scanned at low bias voltages which would normally indicate that no oxide was present. However it has also been shown that at rather moderate voltages nickel oxides are sometimes amenable to tunneling²¹ so the spectroscopic check was necessary.

Discussion

A great deal can be learned about thin film nucleation and growth by simply employing a STM in air to view the surface at moderate resolution. The ability of STM to probe electrical and chemical

properties or to yield atomic resolution if needed gives it a great deal of flexibility in meeting diverse research needs. For all this though the STM is severely handicapped by the dielectric nature of most interesting film systems. Most semiconductors are very difficult to scan in air, oxide films are impossible, and even important metal films such as aluminum oxidize so readily in air that they cannot be studied without a vacuum STM.

Nonetheless it proved possible to analyze a variety of features common to nickel films including the development of microstructure and surface roughness as the substrate temperature and angle of deposition were varied. Even more importantly, the nucleation of nickel films on HOPG was studied with little need for technical sophistication. All that was required was a time consuming count of several thousand nickel islands directly off of filtered STM scans.

CHAPTER VI

CONVENTIONAL FILM ANALYSIS

STM is a truly powerful experimental tool, but it is not the be all and end all of research equipment. There are things it simply cannot do, and STM data is subject to erroneous interpretation if unexpected electrical and chemical interactions are present. Thus while the results in Chapter 5 form the basis of this research, it is necessary to check them against other sources of data. In addition, STM results are somewhat difficult to compare to existing film growth literature because so little of it has been done with STM.

In this chapter results from a variety of conventional film analysis tools are reported including SEM, optical microscopy with Nomarski, optical and stylus profilometry, and X-ray diffraction.

Thickness and Roughness

Due to the limitations of HOPG substrates, conventional film thickness and roughness techniques could only be applied to the nickel films made on fused silica. These results were presented in Chapter 5 with the discussion of STM analysis of film microstructure and roughness. In addition, the stylus profilometer measurements of film thickness were in excellent accord with the nominal film thickness values recorded by the crystal monitor during deposition. Given the near unity sticking coefficient of the nickel films deposited this is no surprise.

Surface roughness measurements made with the Wyko optical profiler differed greatly with STM generated surface roughness data from the same fused silica films. Some disagreement was expected

as it had been observed before on sputtered nickel films. The films sputtered onto silicon had an average Wyko RMS of 1.19 nm, but a STM determined microRMS of only 0.83 nm. The nickel films sputtered onto float glass on the other hand had a Wyko RMS of 0.79 nm and a STM microRMS of 1.79 nm. These are not tremendous differences however, and they are easy to account for by examining the size of features recorded by each device. The Wyko can only record spatial frequencies up to 768 lines/mm⁷⁴ while the STM is easily capable of 21,000 lines/mm even on a large scan. The STM is thus much more sensitive to grain roughness and film porosity while seeing less large scale roughness. The Wyko on the other hand averages these factors and records only those features larger than the wavelength of light. Features of this size are responsible for scattering visible light. Thus a Wyko RMS value would apply to a film used as a coating for visible light use where microRMS is not a concern because it is too small to disturb light transmission or reflection. On the other hand, the STM provides a better picture of the actual disorder of the film surface which is important for shorter wavelength work like X-ray optics.

In this light, the huge difference between the STM and Wyko roughness values for the fused silica films can only be explained by the presence of roughness on several scales. Large features that would contribute to conventional RMS must be largely absent, a fact generally supported by Nomarski micrographs which will be presented shortly. Grain size induced microRMS on the other hand appears to start off quite low at low temperature but increases dramatically above 350°C. As mentioned in Chapter 5 this closely follows the increase in nickel film grain size with increasing substrate temperature reported by Fleet (as presented by Hoffman)⁸⁴ in 1963 for 500 Å thick nickel films.

Film Growth and Microstructure

Because it proved impossible to obtain quality SEM micrographs of the nickel films used in this research, a number of interesting comparative studies between SEM data and STM scans could not be

done. Still, Nomarski micrographs taken of the film surfaces provided some insight into film growth and yielded considerable insight into the large scale structures of the films studied.

Optical Microscopy

Because it lacked the resolution necessary to see the very fine grained structure of the nickel films studied, the Olympus optical microscope was instead used to explore substrate quality and large scale film defects. To better organize this information, it has been divided into sections covering HOPG, fused silica, and a few pictures of the auxiliary sputtered films for comparison.

The surfaces of the various graphite substrates varied widely in quality with the unusually rough films having the rougher substrates. A typical graphite surface area is shown in Figure (6.1) at 100 power. The surface has a large grain structure and a high density of thin grooves and specks. For contrast, a high quality graphite surface is shown in Figure (6.2) at 500 power. It still has a large number of grooves as well as a few nodules visible on the surface. There is also a larger canyon feature at the lower right. HOPG can get much worse though, just look at the canyon feature in Figure (6.3) taken on a sample deposited at 200°C. It was taken over completely grown nickel film area and powerful, large-grained preferential growth can be seen along the upper rim of the canyon just as is seen above smaller graphite features.

Nickel growth on HOPG can also be seen as a field of small island structures in Figure (6.4) which was taken over the island region of a sample grown at 300°C. Similar growth is also visible in Figure (6.5) except that the islands are decorating multiple ledges on the HOPG. This sample was deposited at 205°C. Island structures like these were not observed on any graphite films deposited below 200°C. In fact, on low temperature films it was impossible to detect any film artifacts at all. Even using Nomarski at 1000X failed to reveal any film details. When seen, the nickel islands ranged in size up to approximately one micron, equal to the largest islands observed with STM.

The fused silica films were markedly different. Because of the lack of substrate texture it was possible to identify the film region, but film texture was still difficult to detect. When deposited at low temperature these films were quite hard and resisted damage from handling. The films deposited in

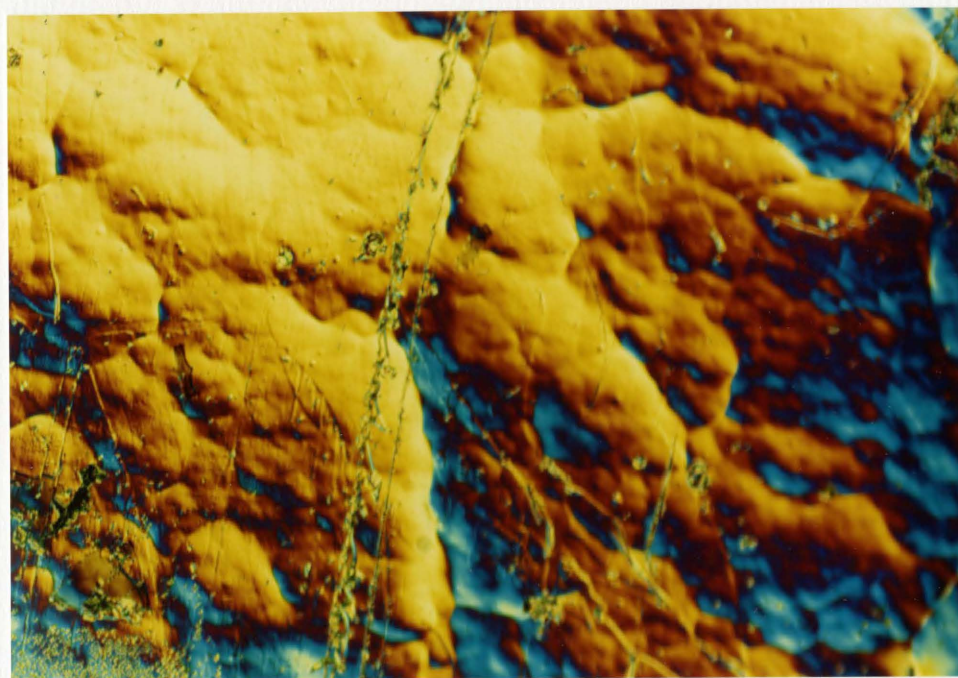


Figure 6.1 A typical surface region on HOPG photographed at 200X.

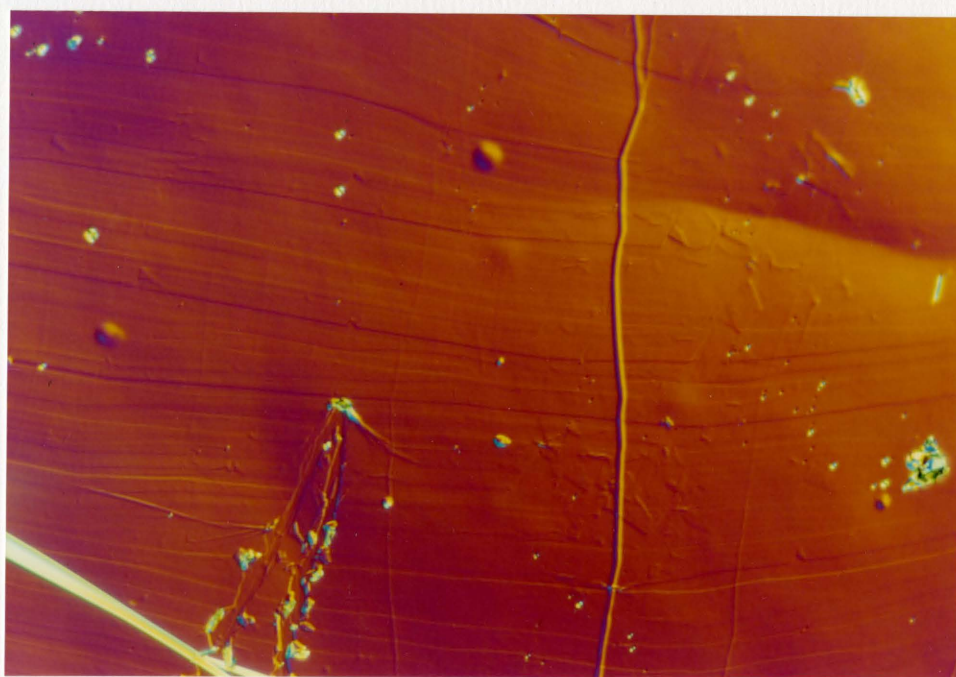


Figure 6.2 A 500X photo of a relatively high quality area of HOPG marred by numerous small grooves and a few larger defects.

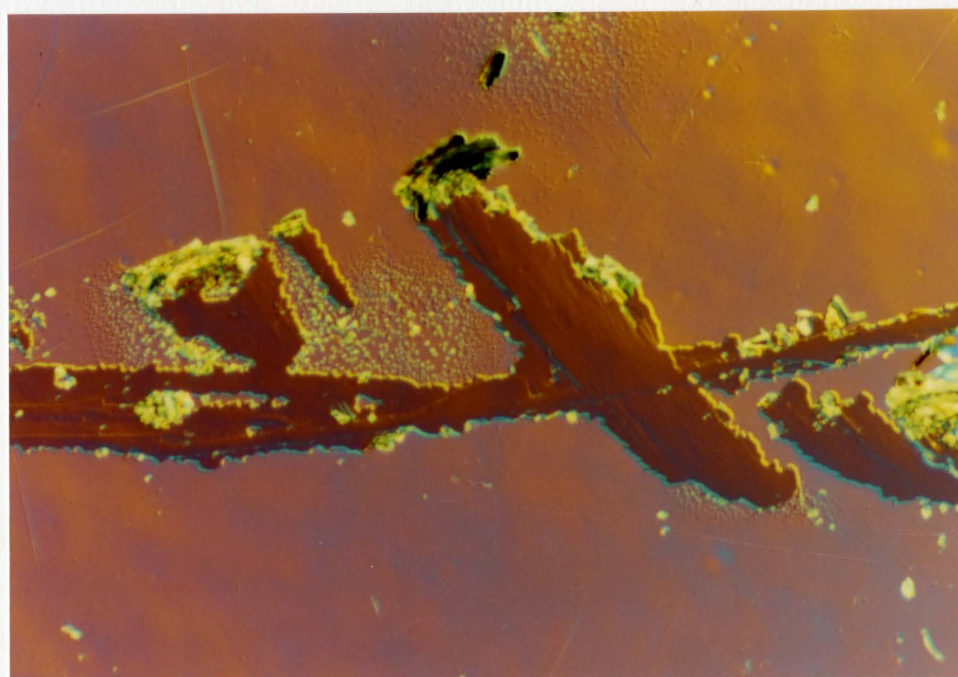


Figure 6.3 A 200X micrograph of a large canyon on HOPG in a nickel film region. Note the preferential film growth around the canyon edges.

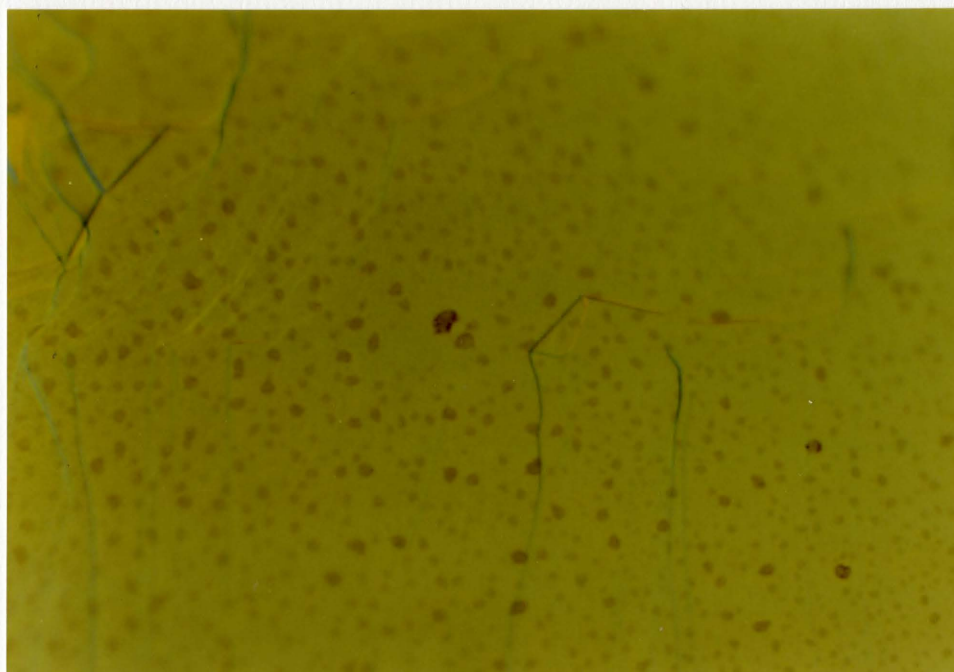


Figure 6.4 A 1000X view of nickel island growth on graphite at 300°C.

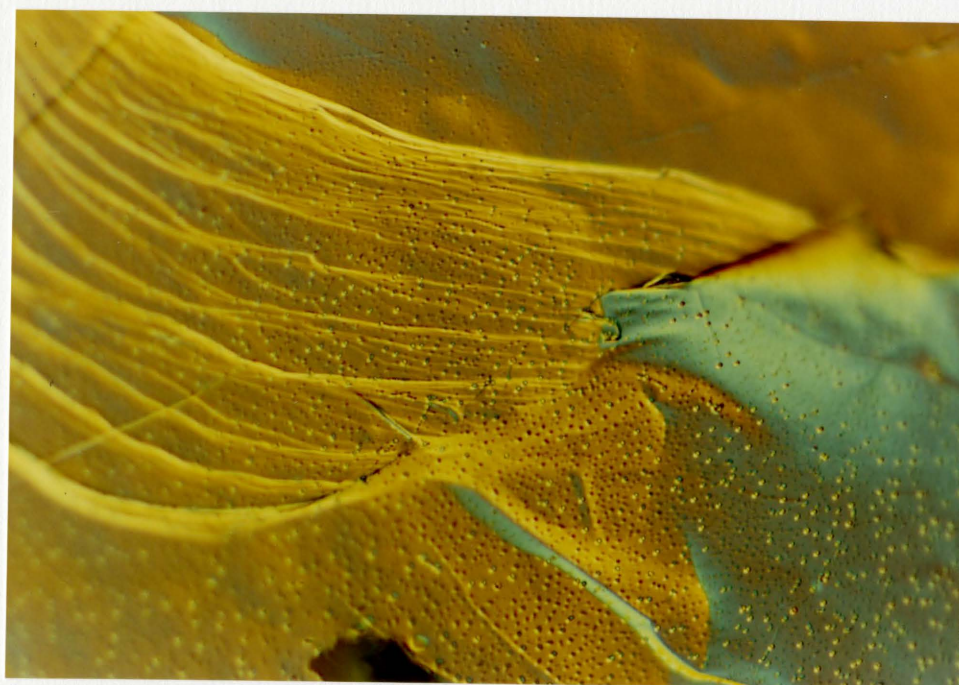


Figure 6.5 A 500X view of nickel island growth on a heavily faulted region of HOPG. This sample was deposited at 205°C.

the Zone 3 structure region however were very soft and could be marred by tissue paper. Apparently annealing of the nickel film was very effective at these high temperatures even if good Zone 3 structure was not observed with STM. Figure (6.6) below shows a 500 power picture of a section of nickel film deposited on fused silica at 500°C. Note the scratches which were produced when cleaving the substrate into sections small enough to fit into the STM. A variety of defects which have propagated through the film from the substrate can be seen in the lower left. Features like this were rare though. Close observation does reveal a slight texture to the film which is reminiscent of the high temperature grain structure of Figure (5.18). Just like films on graphite substrates, films deposited on fused silica below 200°C did not have any visible surface texture. An interesting example is shown in Figure (6.7) of a film deposited on fused silica at 100°C. Taken at 500X, this picture shows one of several holes observed in the nickel films on fused silica. As shown, most of the holes went all the way through to the substrate, but a few were partially filled. Indeed, a few small nickel island growths are visible in the hole shown. Also note the grooves on the film. These are features of the substrate produced by polishing during the production process and they have propagated all the way through the film. Several of them can just be seen traversing the bare substrate in the hole. Except for some contaminants on the surface, this film is basically featureless at this magnification. Even at 1000X no details were resolved on any films deposited below 200°C because of the rapid decrease of film grain size with temperature.

For the sake of comparison, results are also presented for sputtered nickel films deposited on both silicon and float glass at room temperature. These films were very uniform and had no holes or handling marks. An example of the silicon substrate films is shown in Figure (6.8). The film is the lighter region on the left. Note the complete absence of film defects except for surface contamination. This was typical, no substrate features or film texture was observed on these films even at high magnification. The films deposited on float glass were not so perfectly formed. As shown in Figure (6.9), where the film is shown in pink, a great number of bubble-like defects are visible on both film and substrate. These features were common over all of the films deposited on float glass and smaller defect sites were revealed by higher magnification views. Recall however that the Wyko RMS values were lower for the films on float glass than for the films on silicon. The defects seen are easily

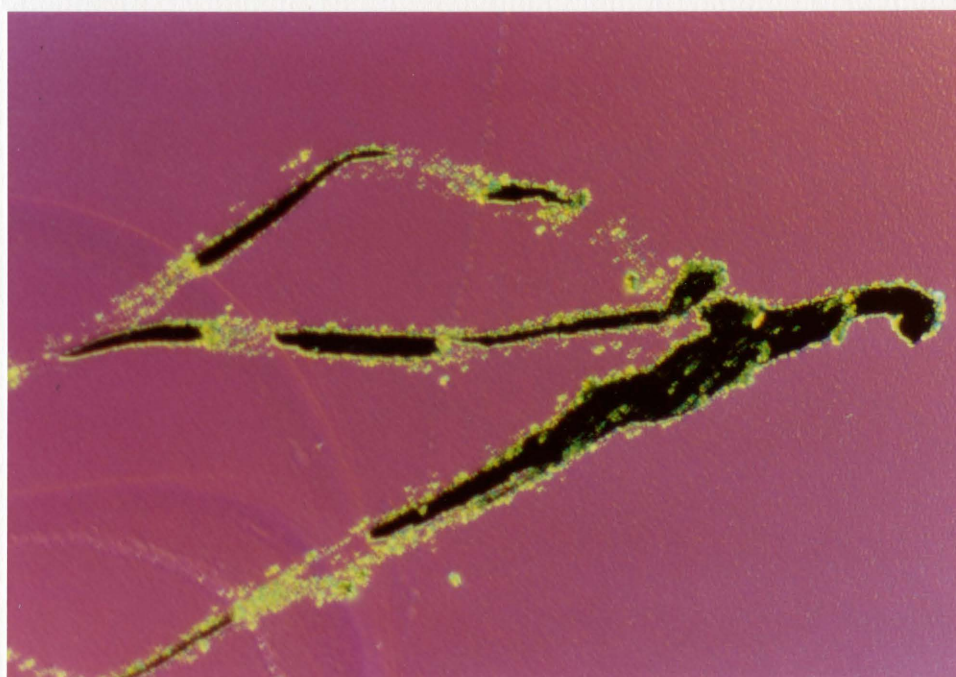


Figure 6.6 Nickel film deposited on fused silica at 500°C shown at 500X. Note the scratches, the substrate defects at the lower left, and the texture of the film which is just visible.

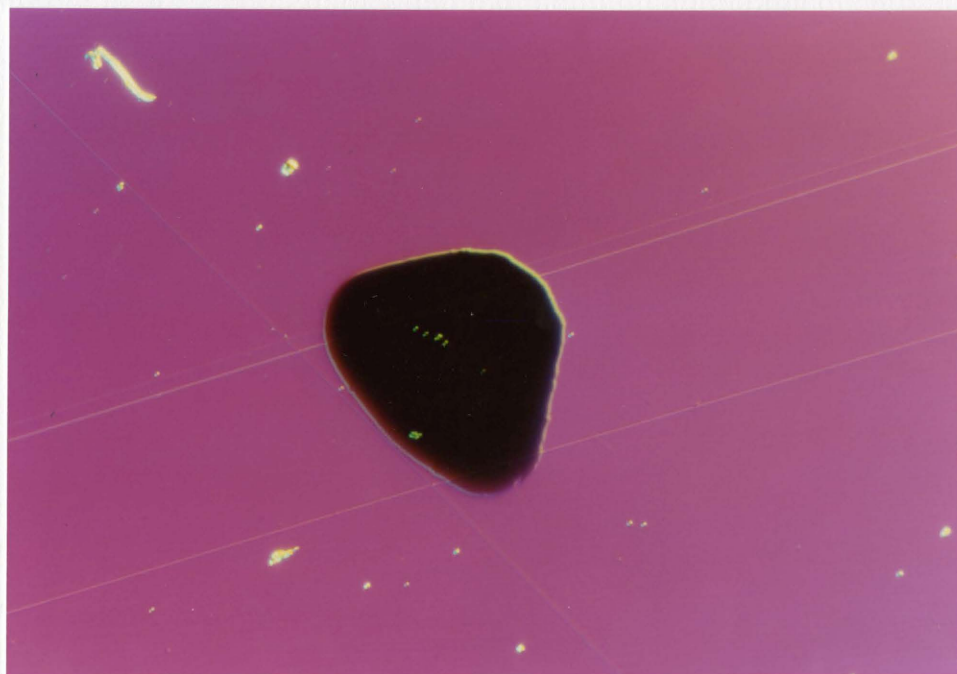


Figure 6.7 A 500X view of a nickel film deposited on fused silica at 100°C. Note the large hole revealing bare substrate and the polishing grooves visible on the film surface which can also be seen on the substrate in the hole.

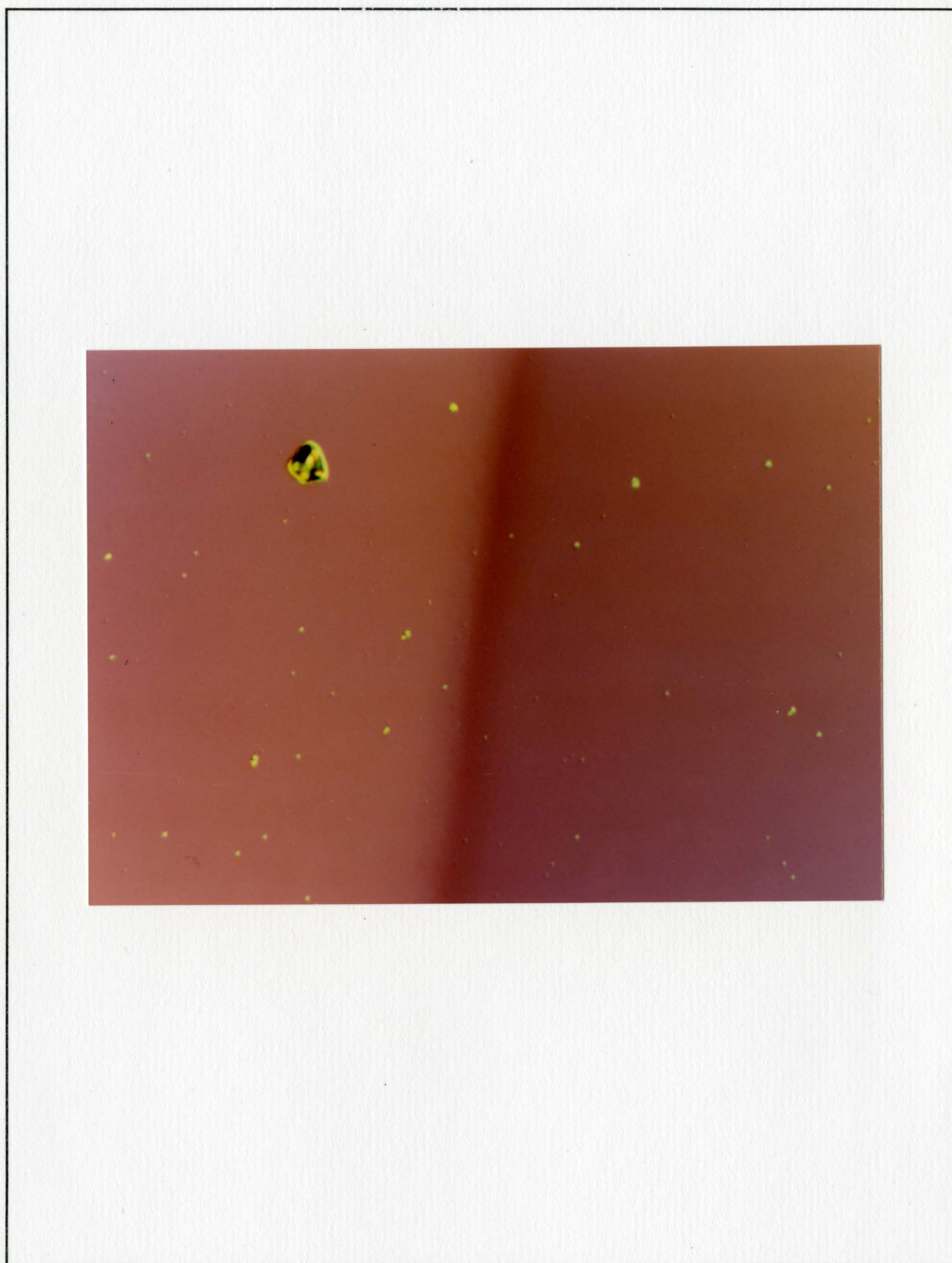


Figure 6.8 A 200X optical micrograph of the edge of a sputtered nickel film on silicon. The film region is the lighter area on the left.

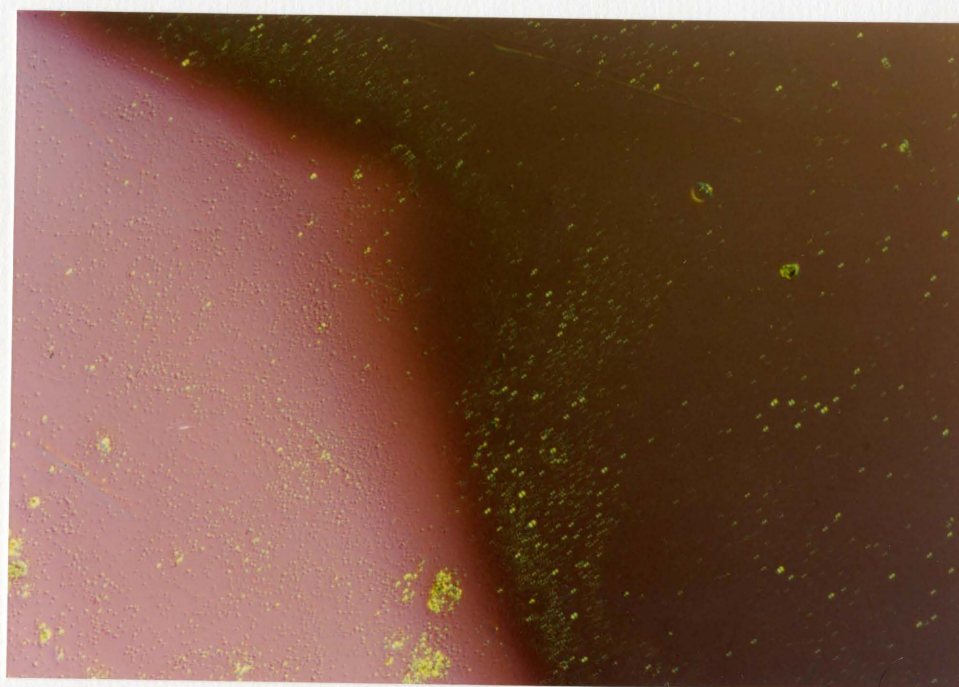


Figure 6.9 A 200X optical micrograph of the edge of a sputtered nickel film on float glass.

large enough to have been detected by the Wyko and should have been reflected by a higher RMS value. The STM did record a larger RMS value for the films on float glass compared to the films on silicon. Furthermore the films on fused silica, which were observed to be marred by holes and polishing grooves, had very low Wyko RMS values and quite high STM microRMS values. It would appear then that the features observed with the optical microscope aided by Nomarski are more clearly represented by STM microRMS than they are by the more conventional Wyko-determined RMS roughness.

Scanning Electron Microscopy

Compared to the relative success of optical microscopy, scanning electron microscopy of the nickel films was a near-complete failure. Despite expending considerable effort and employing every technique available including coating the samples with AuPd to enhance conductivity, no quality images of the films could be produced by SEM. At best it was possible to image a few of the larger features of the graphite substrates underlying the films. One of the very best of these pictures is shown in Figure (6.10). It is just possible to see a few ledge and terrace structures attributable to graphite in this image.

X-ray Diffraction

No attempt was made to use X-ray diffraction as a major study tool during this research. Partially this was because it was feared that even minor X-ray damage to the film would be visible with the STM. In addition, no particularly illuminating results were expected from X-ray data. However, it was necessary to have a few films X-rayed just to confirm that the nickel films were behaving as expected. As is usually the case for FCC metals, the nickel films showed a strong preference for (111) orientation and the nickel peaks were sharper and more intense on the films deposited at high temperatures because of their well-defined grain structure.⁷⁵ Examples of the relevant sections of two X-ray scans, one from a room temperature nickel film on HOPG and a second from one deposited at 300°C, are shown in Figures (6.11) and (6.12).

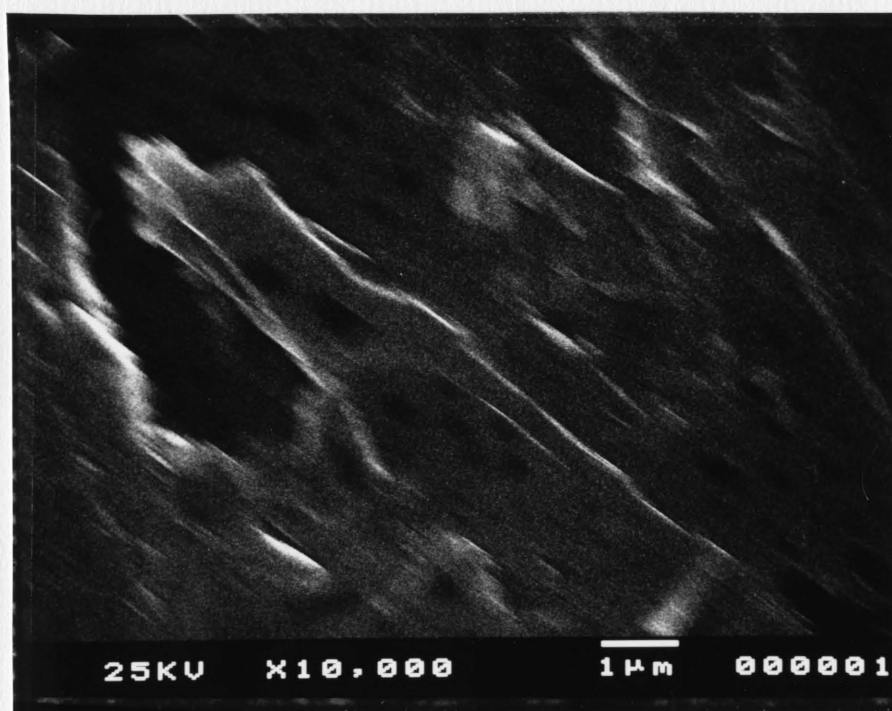


Figure 6.10 A 10,000X SEM image of a nickel film on HOPG which just reveals some of the ledge features characteristic of the graphite.

Grain size determinations from X-ray data on continuous films are not particularly trustworthy, the relevant equations being intended chiefly for determining the size of particles in powders.⁷⁵ Nonetheless grain sizes, d_g , were determined for the nickel peaks shown in Figures (6.11) and (6.12) using the equation,

$$d_g = (0.9\lambda)/(B\cos\theta),$$

where B is angular extent of the film peak at FWHM, θ is the angle where the peak occurred, and λ is the wavelength of the X-rays used.⁷⁵ The low temperature film with its broad diffuse peak had a nominal grain size of 18 nm while the heated film had a grain size of 39 nm. These values are in good agreement with grain sizes observed with STM and with published values for 500 Å thick nickel films, see Figure (5.26).⁸⁴

Comparison With STM Results

Even without useful SEM data, it is possible to draw some strong comparisons between the STM results discussed in Chapter 5 and the data gathered by more conventional means which has been discussed above. The X-ray data gathered is much as expected and the film grain sizes determined from it are in good agreement with STM results. The large number of optical micrographs taken are also in good agreement with STM data where it is possible to bridge the gap in probe area and resolution between the two instruments.

Film Growth

With only optical micrographs to work with, little can be said about the details of nickel film growth. The pictures do show however that the nickel films form sub-micron size islands during growth and that film growth areas are rather evenly populated by these islands. Islands in this size range were observed on large STM scans although at such high resolution their structures were observed to vary

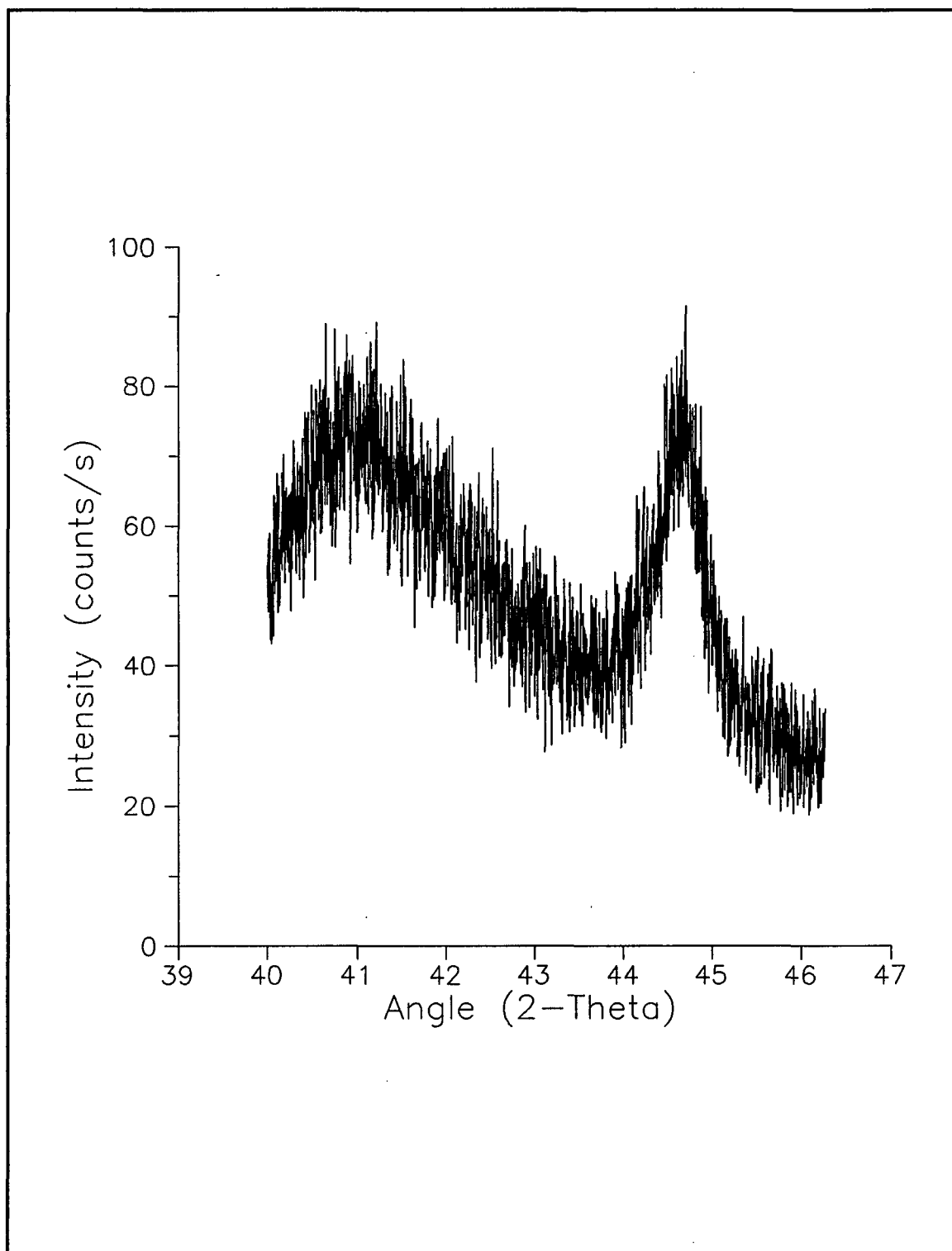


Figure 6.11 X-ray data showing the (111) peak from a nickel film deposited on HOPG at room temperature.

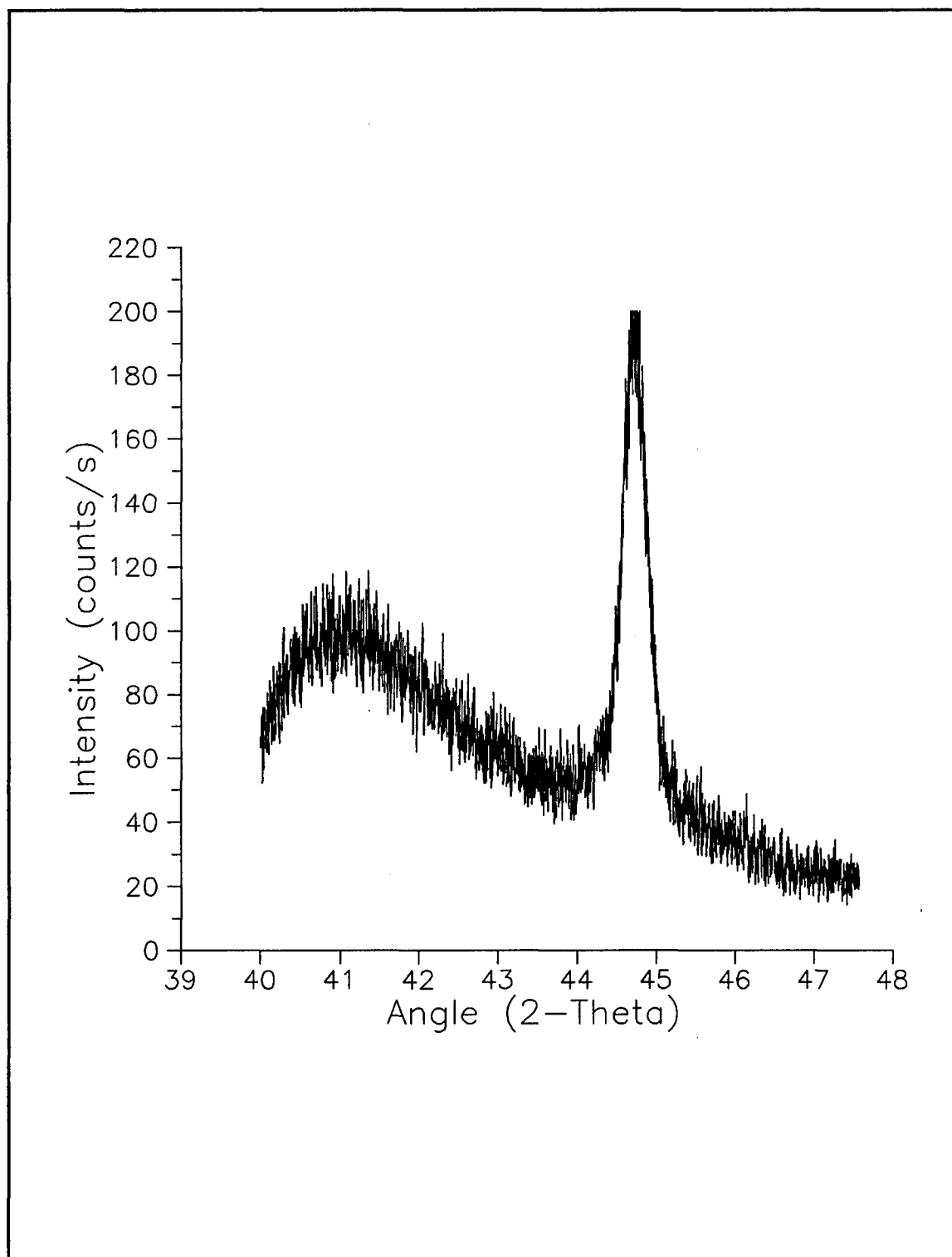


Figure 6.12 A section of an X-ray scan of a nickel film deposited on HOPG at 300°C showing the sharp (111) peak.

considerably. STM also revealed that most of the large islands formed on or near features on HOPG. Optical micrographs were not able to reveal this detail, the islands themselves only being resolved as small dots.

Film Microstructure

The large scale structure of the films studied was revealed by the optical micrographs taken. Large holes, polishing grooves, canyons and groups of ledges on HOPG were all detected only by optical microscopy. STM scans of some of these features are theoretically possible but would not have been of much use given the small scan window available. Actual film grain structure was resolved for some of the high temperature films, but it was far better represented in STM scans. Despite this lack of overlap in the size of features observed, optical microscopy and STM did support each other by revealing the same trends in structure. Films that looked rough on STM scans also looked rough in microscope pictures. The few SEM photographs available also agreed with STM scans, showing the same kinds of graphite features observed by the STM. It is safe to assume then that the STM data is basically free from chemical and electrical anomalies. Certainly it is still possible that local disturbances occurred or that minor tip interactions could have slightly distorted the STM scans, but neither of these effects is strong enough to void the information gleaned from the STM. It was usually operated far above its maximum resolution where all but the worst scan irregularities should have been totally negligible.

CHAPTER VII

SUMMARY

Perhaps the most important result of the work reported in this thesis is not the data itself, but rather the proof it provides of the great number of applications to which STM can be easily adapted in the field of surface science. Certainly the information about the growth of nickel films which was presented is important. Some of it is even completely new work, thanks to the choice of HOPG as a substrate. However, most of the work could have been performed by combining a number of more conventional techniques. With STM however the work could be performed on a single instrument without the need for any significant sample preparation. Moreover, the resulting data is digitized for easy computer manipulation, and the atomic resolution capability of the STM is available should it be needed. These advantages make the STM a powerful new tool for use by the surface scientist, a fact that is manifested by the results presented.

Much of what is already known or expected about nickel films was corroborated by this research. Theoretical considerations indicated that nickel films have a low inherent nucleation barrier and tends to condense completely on a variety of substrates. Both of these facts are supported by this research as is the indicated single atom critical nucleus size for nickel.

The extremely high activation energy for surface diffusion of nickel atoms was something of a surprise though. A fairly large value had been expected because of the high boiling point and tight self-binding of clusters, but the amount of two-dimensional island growth observed lead to expectations of a lower value than that actually measured.^{78,79,80,81} Several possible explanations were provided, including sulfur contamination of the nickel films, underestimation of the mass of nickel deposited due to bulk diffusion into the graphite substrate, and the presence of an anomalous surface energy not accounted for in the nucleation model. In any case it is apparent that some unexpected effect was

driving up the calculated value of E_d , because the passivity of the graphite substrates and the large islands observed decorating features of the graphite surfaces simply do not support such a large energy of activation for surface diffusion.

The roughening of nickel films deposited at high temperatures was also expected. The observed temperature dependence even agrees with nickel grain size studies. However, the consistent disagreement between conventional RMS roughness data and STM-based microRMS values requires that a greater emphasis be placed on selecting the scale of surface defects that one wishes to measure. X-ray data on the other hand agreed nicely with microRMS calculations. The close relationship between the two supports the use of STM as a surface roughness measuring tool for short wavelength work.

Depositing films at non-zero angles of incidence is well known to increase roughness and this was born out in STM studies of films deposited at various angles of incidence. Despite considerable variations in the data it was possible to find a linear relationship between film roughness and angle of deposition, at least for nickel deposited on HOPG. It appears that the formation of large, roughness-inducing hills during growth at high angles of deposition is quite sensitive to something that was not explicitly controlled. Variations in substrate roughness are a distinct possibility because HOPG was used, but it might well be something else such as instabilities in the rate of deposition.

Hopefully this work will provide a useful basis for additional studies of nickel film growth. It should also assist the researcher in need of solid nucleation and growth information about any system to which STM, or its relative, AFM, can be applied, either in air or in vacuum. Some suggestions for related work that arose during the course of this research include such diverse topics as grain boundary characterization, film island to substrate contact angle determinations, cross-sectional STM of films, and direct observation of surface diffusion underneath film masks.

REFERENCES

1. G. Binnig, H. Rohrer, Ch. Gerber and E. Weibel, "Tunneling Through a Controllable Vacuum Gap," *Appl. Phys. Lett.* **40**, 178 (1981).
2. G. Binnig, H. Rohrer, Ch. Gerber and E. Weibel, "Surface Studies by Scanning Tunneling Microscopy," *Phys. Rev. Lett.* **49**, 57 (1982).
3. G. Binnig and H. Rohrer, "Scanning Tunneling Microscopy," *IBM J. Res. Develop.* **30**, 355 (1986).
4. C. F. Quate, "Vacuum Tunneling: A New Technique for Microscopy," *Phys. Today* **39**, 26 (1986).
5. P. K. Hansma and J. Tersoff, "Scanning Tunneling Microscopy," *J. Appl. Phys.* **61**, 163 (1987).
6. Y. Simić-Krstić, M. Kelley, C. Schneiker, M. Krasovich, R. McCluskey, D. Koruga and S. Hameroff, "Direct Observation of Microtubules with the Scanning Tunneling Microscope," *FASEB J.* **3**, 2184 (1989).
7. A. M. Baró, R. Miranda and J. L. Carrascosa, "Application to Biology and Technology of the Scanning Tunneling Microscope Operated in Air at Ambient Pressure," *IBM J. Res. Develop.* **30**, 380 (1986).
8. J. E. Demuth, "Atomic-Scale Surface Characterization With the Scanning Tunneling Microscope," presented at the 8th Annual Symposium of the Arizona Chapter of the American Vacuum Society in Tucson, AZ (April 1989).
9. S. Chiang and R. J. Wilson, "Construction of a UHV Scanning Tunneling Microscope," *IBM J. Res. Develop.* **30**, 515 (1986).
10. J. A. Venables, D. J. Smith and J. M. Cowley, "HREM, STEM, REM, SEM - and STM," *Surf. Sci.* **181**, 235 (1987).
11. J. Schneir, R. Sonnenfeld, O. Marti, P. K. Hansma, J. E. Demuth and R. J. Hamers, "Tunneling Microscopy, Lithography, and Surface Diffusion on an Easily Prepared, Atomically Flat Gold Surface," *J. Appl. Phys.* **63**, 717 (1988).
12. D. W. Abraham, H. Jonathan Mamin, E. Ganz and J. Clarke, "Surface Modification with the Scanning Tunneling Microscope," *IBM J. Res. Develop.* **30**, 492 (1986).
13. G. Binnig, C. F. Quate and Ch. Gerber, "Atomic Force Microscopy," *Phys. Rev. Lett.* **56**, 930 (1986).
14. H. Heinzelmann, E. Meyer, P. Grütter, H.-R. Hidber, L. Rosenthaler and H.-J. Güntherodt, "Atomic Force Microscopy: General Aspects and Application to Insulators," *J. Vac. Sci. Technol. A* **6**, 275 (1988).
15. T. R. Albrecht and C. F. Quate, "Atomic Resolution with the Atomic Force Microscope on Conductors and Nonconductors," *J. Vac. Sci. Technol. A* **6**, 271 (1988).

16. G. Binnig and H. Rohrer, "Scanning Tunneling Microscopy," *Surf. Sci.* **126**, 236 (1983).
17. W. A. Thompson and S. F. Hanrahan, "Thermal Drive Apparatus for Direct Vacuum Tunneling Experiments," *Rev. Sci. Instrum.* **47**, 1303 (1976).
18. W. Betteridge, Nickel and its Alloys, (Ellis Horwood Limited, Chichester, U.K., 1984).
19. S. Park and C. F. Quate, "Tunneling Microscopy of Graphite in Air," *Appl. Phys. Lett.* **48**, 112 (1986).
20. A. Bryant, D. P. E. Smith and C. F. Quate, "Imaging in Real Time with the Tunneling Microscope," *Appl. Phys. Lett.* **48**, 832 (1986).
21. B. Marchon, S. Ferrer, D. S. Kaufman, M. Salmeron and W. Seikhaus, "The Surface Topography of Pyrolytic Carbons and of Gold Thin Films by Scanning Tunneling Microscopy: Grain Boundaries and Surface Defects," *Thin Solid Films* **154**, 65 (1987).
22. V. Elings and F. Wudl, "Tunneling Microscopy on Various Carbon Materials," *J. Vac. Sci. Technol. A* **6**, 412 (1988).
23. G. Binnig, H. Fuchs and E. Stoll, "Surface Diffusion of Oxygen Atoms Individually Observed by STM," *Surf. Sci.* **169**, L295 (1986).
24. G. F. A. van de Walle, H. van Kempfen, P. Wyder and C. J. Flipse, "Scanning Tunneling Microscopy and (Scanning) Tunneling Spectroscopy on Stepped Ni(111)/H," *Surf. Sci.* **181**, 27 (1987).
25. A. M. Baró, G. Binnig, H. Rohrer, Ch. Gerber, E. Stoll, A. Baratoff and F. Salvan, "Real-Space Observation of the 2x1 Structure of Chemisorbed Oxygen on Ni(110) by Scanning Tunneling Microscopy," *Phys. Rev. Lett.* **52**, 1304 (1984).
26. J. A. Venables, "Surface Processes in the Nucleation and Growth of Thin Films," Proceedings IX IVC-V ICSS, (Madrid 1983).
27. C. A. Neugebauer, "Chapter 8: Condensation, Nucleation, and Growth of Thin Films," in Handbook of Thin Film Technology, Eds., L. I. Maissel and R. Glang, (McGraw-Hill, New York, 1970).
28. B. A. Movchan and A. V. Demchishin, "Study of the Structure and Properties of Thick Vacuum Condensates of Nickel, Titanium, Tungsten, Aluminum Oxide and Zirconium Dioxide," *Fiz. Metal. Metalloved.* **28**, 653 (1969).
29. J. Tersoff and D. R. Hamann, "Theory of the Scanning Tunneling Microscope," *Phys. Rev. B* **31**, 805 (1985).
30. J. Bardeen, "Tunnelling From a Many-Particle Point of View," *Phys. Rev. Lett.* **6**, 57 (1961).
31. N. García, C. Ocal and F. Flores, "Model Theory for Scanning Tunneling Microscopy: Application to Au(100)(1x2)," *Phys. Rev. Lett.* **50**, 2002 (1983).
32. N. Garcia, "Theory of Scanning Tunneling Microscopy and Spectroscopy: Resolution, Image and Field States, and Thin Oxide Layers," *IBM J. Res. Develop.* **30**, 533 (1986).
33. T. E. Feuchtwang, P. H. Cutler and N. M. Miskovsky, "A Theory of Vacuum Tunneling Microscopy," *Phys. Lett.* **99A**, 167 (1983).

34. N. D. Lang, "Theory of Single-Atom Imaging in the Scanning Tunneling Microscope," *Phys. Rev. Lett.* **56**, 1164 (1986).
35. J. Tersoff and D. R. Hamann, "Theory and Application for the Scanning Tunneling Microscope," *Phys. Rev. Lett.* **50**, 1998 (1983).
36. M. S. Chung, T. E. Feuchtwang and P. H. Cutler, "Spherical Tip Model in the Theory of the Scanning Tunneling Microscope," *Surf. Sci.* **181**, 412 (1987).
37. N. D. Lang, "Vacuum Tunneling Current from an Adsorbed Atom," *Phys. Rev. Lett.* **55**, 230 (1985).
38. J. H. Coombs and J. B. Pethica, "Properties of Vacuum Tunneling Currents: Anomalous Barrier Heights," *IBM J. Res. Develop.* **30**, 455 (1986).
39. R. García, J. J. Sáenz and N. García, "Conductivity and Structure of Thin Oxide Layers Grown on a Metal Substrate: Scanning-Tunneling Microscopy in NiO on Ni(100)," *Phys. Rev. B* **33**, 4439 (1986).
40. R. S. Becker, J. A. Golovchenko, E. G. McRae and B. S. Schwartzentruber, "Tunneling Images of Atomic Steps on the Si(111)7x7 Surface," *Phys. Rev. Lett.* **55**, 2028 (1985).
41. R. J. Hamers, R. M. Tromp and J. E. Demuth, "Surface Electronic Structure of Si(111)-(7x7) Resolved in Real Space," *Phys. Rev. Lett.* **56**, 1972 (1986).
42. V. M. Hallmark, S. Chiang, J. F. Rabolt, J. D. Swalen and R. J. Wilson, "Observation of Atomic Corrugation on Au(111) by Scanning Tunneling Microscopy," *Phys. Rev. Lett.* **59**, 2879 (1987).
43. C. G. Slough, W. W. McNairy, R. V. Coleman, B. Drake and P. K. Hansma, "Charge-Density Waves Studied With the Use of a Scanning Tunneling Microscope," *Phys. Rev. B* **34**, 994 (1986).
44. J. Tersoff, "Anomalous Corrugations in Scanning Tunneling Microscopy: Imaging of Individual States," *Phys. Rev. Lett.* **57**, 440 (1986).
45. I. P. Batra, N. García, H. Rohrer, H. Salemkink, E. Stoll and S. Ciraci, "A Study of Graphite Surface with STM and Electronic Structure Calculations," *Surf. Sci.* **181**, 126 (1987).
46. R. V. Coleman, B. Drake, P. K. Hansma and G. Slough, "Charge-Density Waves Observed with a Tunneling Microscope," *Phys. Rev. Lett.* **55**, 394 (1985).
47. D. W. Pohl, "Some Design Criteria in Scanning Tunneling Microscopy," *IBM J. Res. Develop.* **30**, 417 (1986).
48. Digital Instruments, Nanoscope II Scanning Tunneling Microscope Instruction Manual, Version 4, 135 Nopal Drive, Santa Barbara, CA 93110.
49. S. Viera, "The Behavior and Calibration of Some Piezoelectric Ceramics Used in the STM," *IBM J. Res. Develop.* **30**, 553 (1986).
50. O. Nishikawa, M. Tomitori and A. Minakuchi, "Piezoelectric and Electrostatic Ceramics for STM," *Surf. Sci.* **181**, 210 (1987).

51. H.-W. Fink, "Mono-atomic Tips for Scanning Tunneling Microscopy," *IBM J. Res. Develop.* **30**, 460 (1986).
52. T. Sakurai, T. Hashizume, I. Kamiya, Y. Hasegawa, T. Ide, M. Miyao, I. Sumita, A. Sakai and S. Hyodo, "Scanning Tunneling Microscope Equipped with a Field Ion Microscope," *J. Vac. Sci. Technol. A*, **7**, 1684 (1989).
53. M. Gehrtz, H. Strecker and H. Grimm, "Scanning Tunneling Microscopy of Machined Surfaces," *J. Vac. Sci. Technol. A* **6**, 432 (1988).
54. R. Nicolaides, Y. Liang, W. E. Packard, Z. Fu, H. A. Blackstead, K. K. Chin, J. D. Dow, J. K. Furdyna, W. M. Hu, R. C. Jaklevic, W. J. Kaiser, A. R. Pelton, M. V. Zeller and J. Bellina, Jr., "Scanning Tunneling Microscope Tip Structures," *J. Vac. Sci. Technol. A* **6**, (1988).
55. M. Aguilar, P. J. Pascual and A. Santisteban, "Scanning Tunneling Microscope Automation," *IBM J. Res. Develop.* **30**, 525 (1986).
56. P. H. Schroer and J. Becker, "Computer Automation for Scanning Tunneling Microscopy," *IBM J. Res. Develop.* **30**, 543 (1986).
57. L. Rosenthaler, H.-R. Hidbar, A. Tonin, L. Eng, U. Staufer, R. Wiesendanger and H.-J. Güntherodt, "Data Processing for Scanning Tunneling Microscopy," *J. Vac. Sci. Technol. A* **6**, 393 (1988).
58. J. A. Thornton, "High Rate Thick Film Growth," in Annual Review of Material Science, 1977, (Annual Reviews, Inc., 1977).
59. K. H. Guenther, B. Loo, D. Burns, J. Edgell, D. Windham and K.-H. Müller, "Microstructure Analysis of Thin Films Deposited by Reactive Evaporation and Reactive Ion Sputtering," *J. Vac. Sci. Technol. A* **7**, (1989).
60. W. A. Tiller, "Fundamental Aspects of Film Nucleation and Growth," *J. Vac. Sci. Technol. A* **7**, 1353 (1989).
61. E. Ritter, R. J. Behm, G. Pötschke and J. Wintterlin, "Direct Observation of a Nucleation and Growth Process on an Atomic Scale," *Surf. Sci.* **181**, 403 (1987).
62. J. A. Ruffner, unpublished research.
63. M. H. Grabow and G. H. Gilmer, "Thin Film Growth Modes, Wetting, and Cluster Nucleation," *Surf. Sci.* **194**, 333 (1988).
64. A. Mazor, B. G. Bukiet and D. J. Srolovitz, "The Effect of Vapor Incidence Angle Upon Thin-Film Columnar Growth," *J. Vac. Sci. Technol. A* **7**, 1386 (1989).
65. R. C. Weast, Ed., CRC Handbook of Chemistry and Physics, 59th ed., (CRC Press Inc., Boca Raton, FL, 1978).
66. G. Apai, J. F. Hamilton, J. Stohr and A. Thompson, "Extended X-ray-Adsorption Fine Structure Of Small Cu and Ni Clusters: Binding-Energy and Bond Length Changes with Cluster Size," *Phys. Rev. Lett.* **43**, 165 (1979).

67. F. Suits, "Deposition and Characterization of Optically Nonlinear Thin-Films with Novel Microstructure," (unpublished Ph.D. dissertation, University of Arizona, 1988).
68. Inficon Leybold-Heraeus Inc., XTC Manual, 6500 Fly Rd., East Syracuse, NY 13057.
69. Union Carbide Corp., Advanced Ceramics, "Technical Specifications Sheet -- Highly-Oriented Pyrolytic Graphite," P. O. Box 94637 Cleveland, OH 44101.
70. R. Brown, "Chapter 6: Thin Film Substrates," in Handbook of Thin Film Technology, Eds., L. I. Maissel and R. Glang, (McGraw-Hill, New York, 1970).
71. G. Binnig and D. P. E. Smith, "Single-Tube Three-Dimensional Scanner for Scanning Tunneling Microscopy," *Rev. Sci. Instrum.* **57**, 1688 (1986).
72. Borland International, 4585 Scotts Valley Dr., Scotts Valley, CA 95066.
73. Tencor Instruments, 2400 Charleston Rd., Mountain View, CA 94043.
74. WYKO Corporation, 1955 E. Sixth St., Tucson, AZ 85719.
75. B. D. Cullity, Elements of X-ray Diffraction, 2nd ed., (Addison Wesley, Reading, Mass, 1978).
76. S. Morita, T. Okada, Y. Ishigame and N. Mikoshiba, "Scanning Tunneling Microscopy of Metal Surfaces in Air," *Surf. Sci.* **181**, 119 (1987).
77. D. W. Pashley, "Chapter 3: The Growth and Structure of Thin Films," in Thin Films, (American Society for Metals, Metals Park, OH, 1964).
78. F. H. Wöhlbier, Ed., Diffusion and Defect Data, Vols. 14 and 16, (Trans Tech S. A., Aedersmannndorf, Switzerland, 1978 and 1980).
79. J. M. Blakely, "Surface Diffusion," in Progress in Materials Science, Vol. 10, (Macmillan Co., New York, 1963).
80. J. J. Burke, N. L. Reed and V. Weiss, Surfaces and Interfaces I: Chemical and Physical Characterization, (Syracuse University Press, Syracuse, NY, 1967).
81. M. D. Coutts and H. L. Pinch, "Surface Decoration and Domains in Very Thin Magnetic Films," *J. Appl. Phys.* **34**, 2113 (1963).
82. R. C. Baetzold, "Study of Evaporated Metal Nuclei by Auger Spectroscopy," *J. Appl. Phys.* **47**, 3799 (1976).
83. J. K. Gimzewski and A. Humbert, "Scanning Tunneling Microscopy of Surface Microstructure on Rough Surfaces," *IBM J. Res. Develop.* **30**, 472 (1986).
84. R. W. Hoffman, "Chapter4: Mechanical Properties of Thin Films," in Thin Films, (American Society for Metals, Metals Park, OH, 1964).